

1 **Asynchronous glacial ~~extent dynamics of LGM mountain glaciers during the Last Glacial Maximum in the~~**
 2 **~~Bogd~~Ikh Bogd massif of Gobi-~~Altay~~Altai range, southwestern Mongolia:**

3 **Aspect control on glacier mass balance**

4 Purevmaa Khandsuren ¹, Yeong Bae Seong ^{1*}, Hyun Hee Rhee ², Cho-Hee Lee ¹, Mehmet Akif Sarikaya³, Jeong-
 5 Sik Oh ⁴, Khadbaatar Sandag ⁵, Byung Yong Yu ⁶

7 ¹Department of Geography, Korea University, Seoul 02841, Korea;

8 ²Division of Glacial Environment Research, Korea Polar Research Institute, Incheon 21990, Korea;

9 ³Istanbul Technical University, Eurasian Institute of Earth Science, Sariyer-Istanbul, 34469, Turkey;

10 ⁴Department of Geography, Dongguk University, Seoul 04620, Korea;

11 ⁵Department of Geography, Mongolian National University of Education, Ulaanbaatar 210648, Mongolia;

12 ⁶AMS laboratory, Korea Institute of Science and Technology, Seoul 02792, Korea;

13 Correspondence to: Yeong Bae Seong (ybseong@korea.ac.kr)

14
 15 **Abstract.** Mountain glacier mass balance is affected by factors other than climate, such as topography, slope, and
 16 aspect. In mid-latitude high mountain regions, the north-south aspect contrast can cause significant changes in
 17 insolation and melt, resulting in local asynchrony in glacial dynamics. ~~Most mid-latitude mountain glaciers reached~~
 18 ~~their maximum extent around the global Last Glacial Maximum (gLGM). However, some also strongly responded to~~
 19 ~~the regional climate change or local non-climatic factors such as topography, leading to asynchronous maximum~~
 20 ~~advances. This study documents the asynchronous response of This study documents the maximum extent and~~
 21 ~~chronology of two paleoglaciers to the local topoclimatic factors using ¹⁰Be exposure age dating and 2D ice surface~~
 22 ~~modelling in the Ikh Bogd massif of Mongolia: one facing north into the Jargalant Valley and the other facing south~~
 23 ~~into the Ikh Artsan valley.~~ ¹⁰Be surface exposure age dating revealed that the ~~Ikh Artsan~~Ikh Artsan short valley glacier
 24 ~~reached its maximum position~~culminated ($M_{th}M_{IA1}$) around 20.1 ± 0.7 ka, coinciding with the gLGM. In contrast,
 25 the Jargalant paleoglacier (M_{J1}) ~~probably~~ reached its maximum extent around 17.2 ± 1.5 ka, around Heinrich 1
 26 stadial and during the post-gLGM northern hemisphere warming. ~~Our 2D ice surface model, which includes the~~
 27 ~~temperature index melt model~~; Our temperature-index melt model predicts that ablation will be substantially lower on
 28 the north-facing slope as it is exposed to less solar radiation and cooler temperatures than on the south-facing slope. ~~an~~
 29 ~~aspect can result in a melt difference between.~~ Two-dimensional ice surface modeling also revealed that the south-
 30 facing Ikh Artsan glacier abruptly retreated from its maximum extent since 20 ka, but the Jargalant glacier on the
 31 shaded slope consistently advanced and thickened due to reduced melt till 17 ka. ~~Modelled timing~~The timings of the
 32 ~~modelled maximum maximum extents~~glacier culmination (20.23 ka in Ikh Artsan, 17.13 ka in Jargalant) are consistent
 33 ~~within $\pm 1\sigma$ with of the~~ ¹⁰Be exposure age results (20.1 ka in Ikh Artsan, 17.2 ka in Jargalant). ~~We also observed several~~
 34 ~~sequences of post-LGM or/and Holocene moraines in both cirques.~~ Extremely old ages ranging from 636.2 ka to 35.9
 35 ka were measured for the inner moraines in the Jargalant cirque (M_{J2} - M_{J4}), suggesting a problem with inheritance from
 36 boulders eroded from the summit plateau.

37

38 **Keywords:** Glacier, late Quaternary, Mongolia, ~~H-Bogd~~[Bogd](#), ¹⁰Be surface exposure dating, paleo-erosion
39 surface, uplifted peneplain, 2D ice surface modelling

40

41 1. INTRODUCTION

42 Massive ice sheets or mountain glaciers respond to various climatic forcing functions that operate on wide
 43 scales from local to global. Winter precipitation and summer air temperature are generally considered the most critical
 44 factors in controlling glacial mass balance and extent. Understanding the impact of climate on past glacial cycles
 45 necessitates a thorough understanding of the timing and amplitude of glacial dynamics. The most recent planet-wide
 46 glacial expansion occurred during the ~~Global-global~~ Last Glacial maximum (gLGM) as a result of changes in major
 47 climate forcings, e.g., reduced summer insolation, tropical sea surface temperatures, and atmospheric CO₂. The
 48 remnants of paleoglacial deposits of gLGM are the best preserved among all the ice ages. The gLGM has been
 49 extensively studied to ascertain the late Pleistocene changes in ice volume, sea-level fluctuations, feedback on climate,
 50 etc. The timing of gLGM has been established using both the marine (e.g., Skinner and Shackleton, 2005; Thompson
 51 et al., 2003; Shackleton, 2000; Shackleton, 1967) and terrestrial (e.g., Fletcher et al., 2010; Clark et al., 2009; Jouzel
 52 et al., 2007; Wang et al., 2001; An et al., 1991) paleoclimatic proxies. Based on proxy records, the timing of gLGM
 53 is constrained between 26.5 to 19 ka, during which the ice sheets and mountain glaciers reached their maximum and
 54 the global sea level was at its minimum (Clark et al., 2009).

55 The timing and extent of the maximum glaciation in many regions worldwide are poorly understood distinct
 56 ice masses respond differently to local and regional climatic conditions. ~~However, a~~ New geochronological techniques
 57 such as in situ cosmogenic surface exposure dating (e.g., Heyman, 2014; Hughes et al., 2013) permit reliable temporal
 58 comparisons between the maximum advances of different mountain glaciers.

59 Evidence from mid-latitude glaciers reveals a more complex behavior than that of synchronized ‘global’
 60 glaciations. In some parts of ~~central~~ Asia, for example, the largest glacial extent occurred before Marine Isotope Stage
 61 (MIS) 2, >100 ka in the northeastern Tibetan plateau (Heyman et al., 2011a) and late MIS 5/MIS 4 in the Kanas
 62 lake, Chinese ~~Altay~~Altai (Gribenski et al. 2018). In the Tian Shan (Blomdin et al., 2016; Li et al., 2014; Koppes et al.,
 63 2008), ~~Altay~~Altai (Blomdin et al., 2018), ~~Khangay~~Khangai (Batbaatar et al., 2018; Pötsch, 2017; Smith et al., 2016;
 64 Rother et al., 2014), and Eastern Sayan, ~~Khovsgol~~ (Batbaatar and Gillespie, 2016; Gillespie et al., 2008) mountains ~~of~~
 65 the central Asia, the largest glaciers dated to MIS 3, while the MIS 2 glaciers appeared to be smaller (Fig. 1). It is
 66 noteworthy that most of the MIS 3 advances are based on a few and/or widely scattered ages of moraine boulders
 67 (Gribenski et al., 2018; Blomdin et al., 2016). On the other hand, in the ~~Giehgene~~Giehgeniyin range (Fig. 9) with arid
 68 climate conditions, the significant cirque glacier advanced during MIS 1 (Batbaatar et al., 2018). These studies suggest
 69 that glaciers in continental ~~central-interior~~ Asia respond to regional-scale climate fluctuation in different ways; hence,
 70 the last glacial maxima differed from place to place. Equilibrium Line Altitude (ELA) depression of MIS 2 maximum
 71 varied ~100 to 1100 m on a scale of a few hundred kilometers from the arid to humid continental environments. ELA
 72 depression estimated 800-1100 m in sub-humid regions (Russian Altai, Khangai, Eastern Sayan, SE Tibetan plateau),
 73 500-600 m in semi-arid Gobi Altai mountains, and 100-600 m in arid northern Tibetan plateau and Tian Shan
 74 (Batbaatar, 2018; see the locations in Fig. 1)

75 In addition to regional climate conditions, non-climatic factors may also control the local extent and dynamics
 76 of glaciation. Topographic factors such as catchment morphology, valley width, length, slope, and aspect, can
 77 influence glacier dynamics and affect the style of glaciation (Barr and Lovell, 2014; Kirkbride and Winkler, 2012).

78 Glacier mass balance varies with slope aspect, snow avalanche, and wind drifting snow. Particularly, the north-south
79 aspect contrast in mid-latitude regions with steeper slopes, higher relief, ~~and higher insolation~~ can generate substantial
80 differences in insolation and melt. This difference may be more significant for cirque, small mountain glaciers, or
81 niche glaciers than for large valley glaciers or ice caps (Evans and Cox, 2005).

82 Although spatio-temporal variations in the glacial extent in response to regional climate change have been
83 mentioned in numerous studies, the influence of ~~topographic changes~~ climatic factor has not been adequately explored.
84 The present study aims to ~~reconstruct~~ evaluate how topographic shading affects ~~the~~ fluctuations in the glacier surface
85 mass balance and consequent changes in glacier thickness and length (advance and retreat) using 2D ice surface
86 model. The spatial and temporal responses of contrastively oriented paleo glaciers to the aspect-driven microclimate
87 are of particular interest to us. We evaluated the response of two mountain glaciers, the south-facing Ikh Artsan glacier
88 and the north facing Jargalant glacier in southwest Mongolia (Fig. 1), to topo-climatic factors. Reliable temporal
89 comparisons between the maximum advances of the two mountain glaciers were made using in situ cosmogenic
90 surface exposure dating (e.g., Heyman, 2014; Hughes et al., 2013). This research will improve our understanding of
91 how mid-latitude glaciers respond to topographic changes.

92 ~~glacier extent and chronology of major glacial events during the last glacial cycle in previously unstudied Ih~~
93 ~~Bogd massif of southwestern Mongolia. Our original hypothesis was the north and south facing valleys would~~
94 ~~experience synchronous paleoglacial advances. Upon falsifying this hypothesis using ¹⁰Be surface exposure dating,~~
95 ~~we then turned to a 2D glacier surface model to determine if the impact of aspect could have influenced the chronology~~
96 ~~for two contrastively oriented (north facing and south facing) valleys.~~

97 2. STUDY AREA

98 2.1 ~~Geology~~General settings of the study area.

99 The Gobi-~~Altay~~Altai range, a ~800 km long NW-SE trending isolated arc of mountains, is bordered in the northwest
100 by the Mongolian ~~Altay~~Altai range and separated from the ~~Khangay~~Khangai range by Gobi Lakes Valley. ~~Ikh Bogd~~Ikh
101 ~~Bogd~~Bogd massif (~~Ikh Bogd~~Ikh Bogd means ‘great saint’ or ‘great sacred mountain’ in Mongolian) is located in the northern
102 Gobi-~~Altay~~Altai range. ~~Its position in the heart of the Gobi makes it an important site to understand the extent and~~
103 ~~timing of glacial changes~~kh Bogd, Gobi-Altai range is one of the key sites for paleoglaciological, paleoenvironmental
104 research in landlocked arid, semi-arid ~~and~~ central Asia.

105 This massif is over 50 km long, 25 km wide, and rises ~2 km above the surrounding arid piedmont. Terguun
106 Bogd (3957 m asl), the massif's highest peak, is also the highest point in the Gobi-Altai range (Fig. 1b). Ikh Bogd's
107 current stress regime is dominated by a network of thrust faults and sinistral strike-slip faults, that combine to form
108 transpressional pop-up structures (Vassallo et al., 2011; Vassallo et al., 2007; Bayasgalan et al., 1999; Cunningham et
109 al., 1996). The highest part (>3000 m) of the flat summit plateau predominantly of Mesozoic granite, whereas the
110 lower parts are mostly Cenozoic gneisses (Vassallo et al., 2011; Jolivet et al., 2007; ~~Tomurtogoo, 1999~~EIC, 1981).

111 The flat summit plateau is thought to be a remnant of a formerly extensive Mesozoic erosion surface (Jolivet
112 et al., 2007; Devyatkin, 1974; Berkey and Morris, 1924), surviving most of the Cenozoic due to its rapid and recent
113 uplift after long-term quiescence (Jolivet et al., 2007). Accordingly, erosion in ~~Ikh Bogd~~Ikh Bogd is limited to several
114 deep gorges. The summit plateau is well-preserved in unincised areas because of the young age of the massif and arid
115 regional climate (Vassallo et al., 2011).

116 Headwater systems of intermittent streams merge and turn into main streams, which later flow out of the
117 mountain front and transport abundant sediments into large alluvial fans. According to the episodic sediment supply,
118 alluvial fans from adjacent valleys coalesced (forming bajadas) and stretch to huge endorheic intermontane basins like
119 the Gobi Lakes Valley (Fig. 2). Numerous prior investigations (e.g. Jolivet et al., 2007; Vasallo et al., 2011) suggest
120 that summit plateau of Ikh Bogd massif lacks Quaternary glacial landforms. However, some well-preserved moraine
121 ridges have been identified and mapped in some cirques of the massif including Ikh Artsan, Jargalant (Batbaatar et al.,
122 2018).

123

124

125

126 2.2 Climate

127 ~~Ikh Bogd~~Ikh Bogd massif is in the cold Gobi Desert, with high amplitude in diurnal and annual temperatures.
128 The climate of the study area is characterized by a dry, cold winter with limited snowfall and hot summer with more
129 than 65% annual precipitation coming in summer (Batbaatar et al., 2018). Bayankhongor (Fig. 2), the nearest aimag
130 center (the largest unit of the Mongolian province) is 140 km away and receives ~~less than ~200~~190 mm of precipitation
131 per year (~~188 mm, an average of 2005–2019~~average, NAMEMNAMHEM, 2020), while ~~precipitation-it~~ drops to ~100
132 mm (Yu et al., 2017, Fig. 2b, 2c and 2d) near Orog lake (1168 m a.s.l, Zhang et al., 2022). The closest weather stations
133 to ~~Ikh Bogd~~Ikh Bogd are Bayangobi (1540 m a.s.l) in the south and Bogd (1240 m a.s.l) in the north. The long-term

134 mean annual temperature measured as 3.4 ± 2 °C in Bayangobi and 4.4 °C in Bogd (Fig. 2c and 2d). The average January
 135 temperature was approximately -18 °C in both stations (NAMEMNAMHEM, 2020).

136 Ikh Bogd experiences long-living winter, a lower mean annual temperature (-10 °C), and higher precipitation
 137 (~200 mm) than its surrounding regions (Fig. 2a, 2b). Even in summer, the temperature is mostly below 0 °C at
 138 altitudes above 3800 m a.s.l in Ikh Bogd (Long-term monthly temperatures are calculated using dry lapse rate of
 139 9.8 °C/km from nearby Bayangobi weather station; Supplementary 1). It begins to snow in nearby Gobi Lakes Valley
 140 around the end of September, although melts quickly. Nonetheless, due to the relatively cold temperature, a thin snow
 141 cover persists on the summit plateau of Ikh Bogd between the end of September and the middle of April. Occasionally,
 142 precipitation falls in the form of snow occurs during summer (Landsat imagery) a thin snow cover persists on the
 143 summit plateau of Ikh Bogd between the end of September and the middle of April. Sometimes, precipitation falls as
 144 snow from June to August (Landsat imagery, Farr et al., 2007). On the other hand Compared to the cool summer of Ikh
 145 Bogd, surrounding areas have summer is warm and wetter summers. The July temperature rises to about 21.8 °C in
 146 Bayangobi and 23.0 °C in Bogd_ (Fig. 2d; NAMEMNAMHEM, 2020).

147 Ikh Bogd has a long living snow cover, lower mean annual temperature (-10 °C), and receives more
 148 precipitation (~200 mm) than its surrounding (Fig. 2a, 2b). Strong Siberian high pressure prohibits the entrance of
 149 westerlies during winter, while westerlies and southwesterlies are still effective during summer in the study area. The
 150 orientation and shape of mobile dunes northwest of Orog lake record the prevailing winds from the northwest (Mischke
 151 et al., 2020; NAMEMNAMHEM, 2020; Yu et al., 2019).

152 Much colder than present-day winters and summers in Mongolia are consistent with the strengthening of the
 153 winter high pressure over northern Eurasia during LGM. LGM summers were 1 to 7°C colder than today in Mongolia.
 154 The southward shift of westerly storm tracks should, therefore, contribute to the lower than present precipitation values
 155 (Tarasov et al., 1999). Multi-proxy records indicate that the local LGM climate if the study area was very dry and
 156 harsh (Yu et al., 2019).

157 **2.3 Glacial landforms and study site setting**

158 The Ikh Bogd massif contains abundance well developed alpine glacial erosional landforms such as cirques,
 159 valleys and depositional landforms such as lateral, terminal and recessional moraine ridges, glacial tills on its northern
 160 and southern slopes. Headwater systems of intermittent streams merge and turn into main streams, which later flow
 161 out of the mountain front as large alluvial fans. The sediment transported by alluvial fan or intermittent streams
 162 accumulates in large endorheic intermontane basins like Gobi Lakes Valley (Fig. 2). Our particular interest in the
 163 present study is to compare the timing of the largest glacier extent in the two small paleo valley glaciers flowed to the
 164 south (Ikh Artsan) and the north (Jargalant; Fig. 1).

165 Glaciers in both valleys were started from cirque shaped headwater above ~3100 m and flowed down to
 166 elevations of ~3000–3200 m. Jargalant valley merge down to the largest valley on the northern flank called Bituut
 167 river valley. This large drainage only experienced glaciations in the form of short cirque valley glaciers on its
 168 headwaters, like in Jargalant valley. A few well preserved moraine ridges have been previously identified near the
 169

170 ~~headwater of Bituut river (Batbaatar et al., 2018). The massif was limited to small cirque valley glaciers is best~~
171 ~~explained by the arid climate of the interior of the Gobi Desert.~~

172 3. METHODOLOGY

173 3.1. Field investigation and geomorphologic mapping

174 We conducted the fieldwork in July of 2018 riding horses. Prior to fieldwork, ~~we had some effort to identify~~ glacial
 175 ~~erosional and depositional extent and moraine ridges~~ landforms from the ALOS PALSAR DEM with 12.5 m resolution
 176 ~~(JAXA/METI, 2007) and oblique imageries of © ArcGIS Earth and © Google Earth~~ Landsat 8 imagery with one arc-
 177 ~~second resolution (Roy et al., 2014; Farr et al., 2007).~~ According to the magnitude of the glaciation, only two categories
 178 ~~of glacial landforms were identified and mapped: glacial cirques and hummocky moraines.~~ Glacial cirques, with
 179 ~~amphitheater-like glacial erosional landforms, were easily recognized around the highest mountain areas.~~
 180 ~~Identification of hummocky moraine has been done from previous study (Batbaatar et al., 2018) and oblique imageries~~
 181 ~~of © ArcGIS Earth and © Google Earth imagery, since the DEM is of insufficient resolution to show the hummocky~~
 182 ~~topography clearly. The mapping was were pre-analyzed performed~~ in a GIS environment and mapped on 30 m Shuttle
 183 Radar Topographic Mission (SRTM), ~~ALOS PALSAR DEM with 12.5 m resolution (JAXA/METI, 2007), satellite~~
 184 ~~imagery of © Bing Maps and © ArcGIS Earth.~~ Local names of some specific landforms (e.g., valleys) were identified
 185 ~~from a 1:100000-scale topographic map of Mongolia (ALMGCM, 1970) and through the interview with the local~~
 186 ~~herders, and Landsat 8 imagery with one arc-second resolution (Roy et al., 2014; Farr et al., 2007).~~ Names of the study
 187 ~~areas and physical characteristics of the specific landforms were identified from a 1:100000-scale topographic map of~~
 188 ~~Mongolia (NAGC, 1969) using their morphology and depositional properties.~~ Pre-identified moraines were confirmed
 189 during fieldwork. They were then categorized based on their stratigraphic position ~~and separation between moraine~~
 190 ~~ridges., morphology, and weathering traits.~~

191

192 3.2. Moraine morphostratigraphy

193 As indicated previously, late Quaternary moraines are only preserved in headwaters. Ih Artsan cirque is smaller and
 194 glacial valley is shorter (~1 km) than Jargalant. The best preserved moraines, with at least seven to eight morainal
 195 crests, occur in the Ih Artsan cirque (Fig. 3; Batbaatar et al., 2018). The farthest moraine sequence ($M_{Ih,1}$) from the
 196 summit plateau was distinguished by abundant matrix-rich glacial sediments, large granitic boulders, and a bulge-like
 197 moraine ridge higher than the inner moraine crests (Fig. 3).

198 The Jargalant paleoglacier has a larger accumulation area and length than Ih Artsan glacier, advancing 1.5
 199 km downvalley. Stratigraphically, we identified four different moraine sequences in the Jargalant complex: $M_{J,4}$, $M_{J,3}$,
 200 $M_{J,2}$, $M_{J,1}$ (from youngest to oldest). $M_{J,4}$ moraine lies between 3365–3410 m a.s.l, containing angular to sub-angular
 201 elast-supported pebble to boulders. Downvalley from $M_{J,4}$ moraine, $M_{J,3}$ and $M_{J,2}$ moraines have smooth matrix-
 202 supported flat tops and steep elast-supported sides. These sequences are longitudinally dissected by intermittent
 203 streams draining toward Bituut valley. The oldest moraine ($M_{J,1}$) was deposited further downvalley, consisting of a
 204 bulging morainal form with large granitic boulders lying on the finer matrix-supported deposit. We speculate that this
 205 oldest preserved material might have extended far enough to reached the Bituut valley (trunk valley). The sequences
 206 were very clearly distinctive in the field as well as in the satellite images (Fig. 4; Fig. 5b).

207

208 3.3. Equilibrium Line Altitude

209 ~~Ih Bogd~~Ikh Bogd massif is unglaciated today. Furthermore, the nearest modern glaciers to the study area are in
 210 Otgontenger (~~Khanga~~Khantai) and Sutai (Mongolian ~~Altay~~Altai), which are approximately 350 to 550 km north and
 211 west of the Ikh Bogd respectively. Thus, we could not calculate present ELAs or ELA depression; hence only ELAs
 212 for former glaciers (Ikh Artsan and Jargalant glaciers) were estimated for comparing glacier behavior of Ikh Artsan
 213 and Jargalant glaciers.-

214 The THAR method may include a large error when glacier geometry is complex (Benn & Lehmkuhl 2000).
 215 Yet, it is more suitable for our study area because it has simple glacier morphology. A relatively lower value of THAR
 216 (Meierding 1982) is commonly used in previous studies of mid-latitude glaciers; however, higher value is applicable
 217 according to glacier type or location. We also used a higher THAR ratio of 0.58 because the Ikh Bogd massif must
 218 have a higher ratio due to its arid environment during the last glaciation (Gillespie et al. 2008; Lehmkuhl et al., 2018;
 219 Felauer et al., 2012).

$$220 \text{ELA} = A_t + 0.58(A_h - A_t) \quad (1)$$

221 where A_h and A_t are the headwall and toe altitudes, respectively.

222 A major problem exists in defining the headwall limit of a former glacier, which is a very subjective and
 223 arbitrary (Porter 1981). The glacial headwall altitude was considered to be 1/3 of the altitude difference between the
 224 cirque floor and the top of the rock cliff, which was a similar ratio for schrund-lines estimation in White Mountains,
 225 New Hampshire, USA (Goldthwait, 1970). In this study, wHeadwall obtained the altitude of the lower and upper
 226 limits extracted of past glaciers using GPS, Google Earth imagery, and anfrom ALOS PALSAR DEM with 12.5 m
 227 resolution (JAXA/METI, 2007). The altimetric error (vertical uncertainty) of the DEM is ~5-7 m (Chai et al., 2022,
 228 Ferreira and Cabral, 2021). Glacial toe altitude was measured in the field using GPS and confirmed with the altitude
 229 extracted from the DEM.

230 The glacial toe was considered to be the minimum altitude of the terminal moraine, while the glacial headwall
 231 altitude was considered to be 1/3 of the altitude difference between the cirque floor and top of the rock cliff (Goldthwait,
 232 1970). Estimates of the headwall altitude for high and steep cirques can range from tens to hundreds of meters, and
 233 determination of the glacial headwall is elusively subjective and arbitrary (Porter 1981). The median altitude method
 234 (MEM; THAR=0.5) is commonly used; however, according to glacier type or location, lower (Meierding 1982) or
 235 higher (Gillespie et al. 2008) ratios may be used. For this reason, we also used a higher THAR ratio of 0.58 (Gillespie
 236 et al. 2008) because Ih Bogd massif must have higher ratio due to its arid environment during the last glaciation
 237 (Lehmkuhl et al., 2018; Felauer et al., 2012).

238

239 **3.43. Cosmogenic ^{10}Be surface exposure dating**

240 We used cosmogenic ^{10}Be surface exposure dating based on the specific sampling procedure below to determine the
 241 timing of the last glacial advances in ~~Ih Bogd~~Ikh Bogd massif (Khandsuren et al., 2019; Gosse and Phillips, 2001).
 242 We sampled quartz-rich granitic boulders on the moraine crests, which were not reworked and represented single,
 243 distinguishable ice-marginal positions. We sampled boulders that are rooted in the upper flat surface of the moraine
 244 crest and away from steep slopes to avoid post-depositional movement such as rolling and sliding downslope. We
 245 avoided boulders smaller than 50 cm above ground level that are likely to have been buried, exhumed, or heavily

246 eroded. Samples were obtained by chisel and hammer from the top surfaces of boulders (less than 5 cm thick) to avoid
 247 the edging effect. We sampled at least five boulders from each single moraine crest to statistically screen any outliers
 248 such as inheritance or post-glaciation reworking.

249 Sample processing for the cosmogenic ^{10}Be surface exposure dating was carried out following Seong et al.
 250 (2016), with the revised procedure of Kohl and Nishiizumi (1992). Rock samples were crushed and sieved to obtain
 251 a monomineralic quartz sample and avoid grain size dependency. Meteoric ^{10}Be and other contaminations were
 252 removed by successive HF/HNO₃ leaching. Purified quartz samples (250~500 μm) were first spiked with ~1047.8
 253 ppm concentrated ^9Be carrier and then dissolved with HF/HNO₃. Fluorides were removed by Perchloric (HClO₄) acid,
 254 while Be was separated from other ions (cations/anions) using ion-exchange chromatography columns. Beryllium
 255 hydroxide was recovered using ammonium hydroxides. Consequently, Be(OH)₂ gels were dried at high-temperature
 256 hotplates. They were calcinated to be oxide forms in a furnace at higher temperatures (800 °C). BeO samples were
 257 mixed with Niobium powder and targeted in aluminum target to be loaded into 6 MV tandem Accelerator Mass
 258 Spectrometry (AMS) for $^{10}\text{Be}/^9\text{Be}$ ratio measurement in the Korea Institute of Science and Technology. $^{10}\text{Be}/^9\text{Be}$ ratios
 259 for each sample were measured relative to the 07KNSTD standard sample 5-1 (Nishiizumi et al., 2007), having a
 260 $^{10}\text{Be}/^9\text{Be}$ ratio of $2.71 \times 10^{-11} \pm 4.71 \times 10^{-13}$ (calibrated error). The measured average ^{10}Be to ^9Be ratio of the processing
 261 blank was $4.53 \times 10^{-15} \pm 1.6 \times 10^{-15}$ (n=2). The exposure ages were calculated using Cronus-Earth online calculator v3
 262 (Balco et al., 2008). ^{10}Be Production rate scaling was based on the time-dependent and nuclide-specific LSDn scaling
 263 (Lifton et al., 2014) ~~as well as the non-time dependent scaling model (Stone, 2000)~~. Several studies about last glacial
 264 history in continental central Asia (e.g Rother et al., 2014, Batbaatar et al., 2018) present ^{10}Be exposure ages referenced
 265 to other scaling methods. For a simple comparison, we recalculated exposure ages with LSDn scaling model (Fig. 9).
 266 Errors of exposure ages were represented by external uncertainty (1 σ confidence level).

267 We tested the boulder populations to find outliers using the Chauvenet and Pierce criterion and normalized
 268 deviation methods (Ross, 2003; Chauvenet, 1960, Batbaatar et al., 2018) before we assigned deglaciation ages of
 269 moraine sequences. The idea behind using Chauvenet's criterion is to find a probability band centered on the mean of
 270 a normal distribution containing all n samples. And any data points that lie outside this probability band can be
 271 considered to be outliers. In contrast, Peirce's criterion is based on Gaussian distribution, and the data point is rejected
 272 if its deviation from the mean exceeds the maximum allowed deviation (calculated from the standard deviation of the
 273 group and Peirce's criterion table). For the normalized deviation, a sample in groups was rejected if its normalized
 274 deviation from the group mean (excluding the tested sample) was greater than two (Batbaatar et al., 2018). The For
 275 the normalized deviation, a sample in populations was rejected if its normalized deviation from the group mean
 276 (excluding the tested sample) was greater than two (Batbaatar et al., 2018). sample was excluded from the group if its
 277 exposure age was recognized as an outlier in any of these three methods. We also calculated the reduced chi-square
 278 value and the relative uncertainty of the group (Blondin et al., 2018; Balco, 2011) after rejecting outliers. The arithmetic
 279 ~~mean~~ mean and group standard deviation were standard deviation (1 σ) of the exposure ages in the group was
 280 considered as a representation of the group age. However, we also calculated the total uncertainty including group
 281 standard deviation and external uncertainty (systematic uncertainty) of each sample within the group (Batbaatar et al.,
 282 2018). We presented minimum exposure ages assuming zero erosion because it has been negligible (at least for the

283 sampled surface) since the boulders were deposited based on field observations and considering almost negligible
 284 erosion in arid regions. We ~~We also performed boulder erosion sensitivity tests on our exposure ages, using erosion~~
 285 rates of 1-4 mm kyr⁻¹ (Blomdin et al., 2018), assumed zero erosion for all samples because it has been negligible (at
 286 least for the sampled surface) since the boulders were deposited, based on field observations. We omitted corrections
 287 for snow cover and vegetation change due to the ephemeral winter snow cover at the elevations of the sampled
 288 boulders (e.g., Gosse and Phillips, 2001) because modern winter snow cover (Oct-Apr) is very thin and no tree cover
 289 exists due to aridity.

290 After rejecting the outliers, Welch's t-test statistic were also used to compare the exposure ages of distal
 291 moraines of two groups (M_{IA1} and M_{I1}). Welch's t-test assumes that the sample means being compared for two groups
 292 are normally distributed, and that the groups have unequal variances. The null hypothesis (H_0) states the means of the
 293 two groups are same, while alternative hypothesis (H_a) states that the means of two groups are unequal. We also
 294 performed the t-test with total uncertainty of the groups instead of group variances in 0.05 significance level.

295 Since our study area is considered to be a well-preserved paleo peneplanation surface, the ¹⁰Be concentration
 296 of the flat summit plateau must be measured very high. If our sampled boulders have an "inherited" component from
 297 the summit plateau, the apparent exposure age should significantly exceed the moraine deposition age. We assumed
 298 that the ¹⁰Be concentration from extremely old boulders could represent the concentration of summit plateau itself.
 299 Hence, we tried to calculate exposure age and ~~minimum~~ the lowest erosion rate of the summit plateau using the highest
 300 measured ¹⁰Be concentration from the oldest moraine boulder. Therefore, we selected ~~the highest~~ point (3625 m,
 301 44.6°N, 100.2°E) between the Jargalant and Ikh Artsan cirques that is representable of the summit plateau. ~~The point~~
 302 ~~was chosen at the highest elevation (3625 m) between Jargalant and Ikh Artsan cirques~~ (Fig. 12). The minimum
 303 erosion rate was calculated with the "Erosion rate calculator" of Cronus Earth V3.0.2 using elevation and geographical
 304 coordinate of the selected point, sampling thickness and and the input parameters were: SP001 (sample name, Summit
 305 Plateau), 44.6 (latitude), 100.2 (longitude), 3625 (elevation/pressure), std (elevation/pressure handling flag), sampled
 306 thickness of oldest boulder, 2.7 (density of granite), 1 (shielding correction), 0 (erosion rate), 2018 (date of sample
 307 collection), Be 10 (nuclide), quartz (mineral), ¹⁰Be concentration of the oldest boulder, uncertainty in the ¹⁰Be
 308 concentration, 07KNSTD (name of standard sample). considering the shielding factor as 1 (unshielded).

309

310

311 **3.4. The 2D ice surface modelling**

312

313 A 2D ice surface model covering 22-16 ka was used to examine the influence of aspect on glacier mass
 314 balance and dynamics and to explain the empirical dating results. The model calculates glacier mass balance variation
 315 and corresponding vertical changes in the glacial ice surface (3.4.1). Furthermore, it defines the glacier toe location
 316 (3.4.2) relative to the changing ELA via ice thickening or thinning. Our simulation cannot model actual glaciers; rather,
 317 it examines the possibility that variable melt rates could cause a significant difference in mass balance. ~~to explain the~~
 318 ~~empirical dating results.~~

319

3.4.1 ~~Glacial thickening and thinning:~~ Glacial surface mass balance model: glacial thinning and thickening.

Glacier mass balance (m) is determined by the summation of net ablation (a, see 3.4.1.1) and accumulation (c, see 3.4.1.2) and ablation (a) over a stated period (t):

$$m = \cancel{c} - \cancel{a} + \cancel{a} - \cancel{b} = \int_{t_1}^{t_2} (ea + ab) dt \quad (2)$$

To infer the net gain and loss of glacier mass along the longitudinal profile (Fig. 8e) for both catchments, we calculated and plotted the variations in June, July, August (JJA; see 3.4.1.1) ~~mean-melt-rate~~ and winter precipitation (i.e., snow ~~in the through the~~ whole year; see 3.4.1.2) during 22-16 ka ago. The elevation of the profile was taken from DEM with 12.5 m spatial resolution in 5 m spatial intervals. Site parameters and input parameters of this model are described in Tables 3 and 4.

3.4.1.1 ~~Glacier ablation: Temperature-index glacier melt model including potential clear-sky direct solar radiation~~

We assumed that the topography (aspect and slope) is the main factor producing difference in daily incoming solar radiation on south- and north-facing slopes. The Earth's surface receives more energy as the solar altitude angles (α) is high (zenith angle and angle of incidence are low). The diurnal changes in solar altitude angle are caused by the earth's rotation around its axis, which varies from morning to evening. At sunrise and sunset, the solar altitude angle is 0 degrees, and it reaches its maximum value at noon. Accordingly, in the mountainous area of the northern hemisphere, the south-facing slope receives the highest energy at noon. The north-facing slope, on the other hand, receives little or no energy due to the topographic shading effect (Fig. 2e). Such a diurnal cycle of insolation would result in a major variation in the yearly or long-term mass balance of mountain glaciers (by surface melt) flowing on south- and north-facing slopes on a long-term scale.

Calculating orbital parameters

Slow changes in axial tilt, shape of the Earth's orbit, and axial precession cause combined to result in long-term cyclical changes in daily incoming solar radiation. First, we computed long-term variations in orbital parameters such as obliquity, eccentricity, and longitude of the perihelion (Berger and Loutre, 1991). ~~Based on These main orbital parameters elements, cause the long-term variation of solar declination (δ) variations that produce seasonal variation in solar altitude at the given latitude. were calculated and~~ Furthermore, the long-term variation of solar declination was ~~consequently~~ used to calculate the hour angle, zenith angle, and angle of incidence variations (Eq. 3-11). ~~The computed Long~~ long-term orbital parameters and solar declination variations make all our calculations time-dependent (Fig. 3).

Calculating hour angle

To define aspect-driven contrast in potential direct solar radiation between south-facing and north-facing valleys, we calculated hourly insolation (Eq. 12) applying the same input parameters, except for the topography (aspect and slope; Fig. 3). To calculate hourly insolation and day length, we calculated sunrise and sunset hour angles for horizontal and inclined surfaces (Eq. 3-9).

356 Sunrise and sunset hour angles on the inclined surface were calculated as a function of latitude, solar declination,
357 slope, and azimuth (Iqbal, 1963). Sunrise hour angle for horizontal surface:

358

$$359 \quad \omega_s = \cos^{-1} (-\tan\phi \tan\delta) \quad (3)$$

360

361 To obtain hour angles on the inclined surface, x and y were extracted from formula 1.6.7 created by Iqbal (1963).

$$362 \quad x = \frac{\cos\phi}{\sin\gamma \tan\beta} + \frac{\sin\beta}{\tan\gamma} \quad (4)$$

363

$$364 \quad y = \tan\delta \left(\frac{\sin\phi}{\sin\gamma \tan\beta} - \frac{\cos\phi}{\tan\gamma} \right) \quad (5)$$

365

366 The following equations give the sunrise and sunset hour angles on the surface oriented toward the east.

$$367 \quad \omega_{sr} = \min \left[\omega_s, \cos^{-1} \left(\frac{-xy - \sqrt{x^2 - y^2 + 1}}{x^2 + 1} \right) \right] \quad (6)$$

368

$$369 \quad \omega_{ss} = -\min \left[\omega_s, \cos^{-1} \left(\frac{-xy + \sqrt{x^2 - y^2 + 1}}{x^2 + 1} \right) \right] \quad (7)$$

370

371 The following equations give the sunrise and sunset hour angles on the surface oriented toward the west.

$$372 \quad \omega_{sr} = \min \left[\omega_s, \cos^{-1} \left(\frac{-xy + \sqrt{x^2 - y^2 + 1}}{x^2 + 1} \right) \right] \quad (8)$$

$$373 \quad \omega_{ss} = -\min \left[\omega_s, \cos^{-1} \left(\frac{-xy - \sqrt{x^2 - y^2 + 1}}{x^2 + 1} \right) \right] \quad (9)$$

374 Equations 3 to 9 are for calculating hour angles in arbitrary surfaces, where ω_s is the sunrise hour angle for
375 horizontal surfaces, ω_{sr} , ω_{ss} is the sunrise and the sunset hour angles on the inclined surface, ϕ is the latitude, δ is the
376 solar declination angle, β is the slope inclination angle, and γ is the surface azimuth angle.

377

378 **Calculating zenith angle and angle of incidence**

379 Furthermore, the local zenith angle (Z) and the angle of incidence (θ) were calculated using ~~a one-hour~~
380 ~~interval-of-hour angles~~ at one-hour intervals (ω). The zenith angle is angle between sun rays and normal plane to the
381 surface ($90^\circ - \alpha$) and approximated as a function of latitude, solar declination angle, and hour angle (Iqbal, 1983):

382

$$383 \quad Z = \sin\delta \sin\phi + \cos\delta \cos\phi \cos\omega \quad (10)$$

384

385 and the angle of incidence on the arbitrary oriented surfaces is expressed as:

386

$$387 \quad \cos\theta = (\sin\phi \cos\beta - \cos\phi \sin\beta \cos\gamma) \sin\delta + (\cos\phi \cos\beta + \sin\phi \sin\beta \cos\gamma) \cos\delta \cos\omega + \cos\delta \sin\beta \sin\gamma \sin\omega \quad (11)$$

388

389 where β is the slope inclination angle and γ is the surface azimuth angle.

390

391 **Calculating daily insolation and daily melt**

392 Hourly potential clear-sky direct solar radiation (I) was calculated as (Hock, 1999):

$$393 \quad I = I_0 \left(\frac{R_m}{R} \right)^2 \Psi_a \left(\frac{P}{P_0 \cos Z} \right) \cos \theta \quad (12)$$

394 where I_0 is solar constant (1368 W m^{-2}), $(R_m/R)^2$ is the eccentricity correction factor of the Earth's orbit for the time
 395 considered with R the instantaneous Sun-Earth distance, and R_m is the mean Sun-Earth distance, Ψ_a is the mean
 396 atmospheric clear-sky transmissivity ($\Psi_a=0.75$: (Hock, 1998)), P_h is the atmospheric pressure (OAF, 1976), P_0 is the
 397 mean atmospheric pressure at sea level, Z is the local zenith angle, and θ is the angle of incidence between the normal
 398 to the grid slope and the solar beam. Therefore, hourly insolation was summed into daily insolation for corresponding
 399 day length (not for 24 h; Fig. 3).

400

401 We calculated daily melt with following equation using daily insolation value (Eq. 12).

402

$$403 \quad a = \begin{cases} \left(\frac{1}{n} MF + a_{ice} I \right) T & : T > 0 \\ 0 & : T \leq 0 \end{cases} \quad (13)$$

404 MF is a melt factor ($\text{mm d}^{-1} \text{ } ^\circ\text{C}^{-1}$), a_{ice} is a radiation coefficient for ice surfaces, I is potential clear-sky direct solar
 405 radiation at the ice surface (W m^{-2}), and T is the time-dependent monthly mean temperature ($^\circ\text{C}$). Furthermore, we
 406 integrated (summed) the daily melt into monthly and summer melt (Fig. 3).

407

408 **Calculating time-dependent temperature.**

409 We calculated the time-dependent temperature of the study area in the following order:

410 1) Present-day monthly air temperatures (T) for both cirque headwall altitudes (3533.3 m in Jargalant, 3508.3 m in
 411 Ikh Artsan) were calculated from the two nearest national weather stations using a summer adiabatic lapse rate of $8 \text{ } ^\circ\text{C}$
 412 km^{-1} (Batbaatar et al., 2018). Bayangobi weather station (1540 m a.s.l.) is 27 km SE of the study region, and Bogd
 413 (Horiult) weather station (1240 m a.s.l.) is 45 km NW (Fig. 2c).

414 2) We use only summer temperature because even today, monthly mean temperatures between August to May are less
 415 than $0 \text{ } ^\circ\text{C}$, in which no melt occurs (NAMHEM, 2020). The long-term average of the extreme minimum temperature
 416 at the mean glacial toe altitude (Ikh Artsan and Jargalant) is $-5.2 \text{ } ^\circ\text{C}$ (calculated from Bayankhongor 1874 m) a.s.l.
 417 using lapse rate of $8 \text{ } ^\circ\text{C}/\text{km}$). The JJA mean temperature at the cirque headwall altitude was measured as $3.5 \text{ } ^\circ\text{C}$ in
 418 Jargalant valley and $5.4 \text{ } ^\circ\text{C}$ in the Ikh Artsan valley and $3.5 \text{ } ^\circ\text{C}$ in Jargalant valley. We chose the value of $5.4 \text{ } ^\circ\text{C}$ for
 419 the summer temperature of the study area and used further calculations (see supplementary 1 file).

420 3) We obtained a time-dependent summer temperature since 22 ka. LGM summer temperature was easily calculated
 421 by subtracting known LGM summer temperature anomaly ($1\text{--}7 \text{ } ^\circ\text{C}$ by Tarasov et al., 1999) from the present-day
 422 temperature of the study area. The study area's present-day modern and LGM summer temperature of the study area
 423 ($5.4 \text{ } ^\circ\text{C}$) was calibrated to Greenland temperature data (from NGRIP ice core (Buizert et al., 2018) since 22 ka (~~Buizert~~
 424 ~~et al., 2018~~) to obtain time-dependent temperature variation (see supplementary 2 file).

425 4) LGM summer temperature anomalies ranging from -5.0 °C to -6 °C were applied to calculate glacial melt since 22
426 ka (see supplementary 2 file).

427

428 3.4.1.2 Glacier accumulation and snow data

429 Climatologies at high resolution for the ~~earth's~~-Earth's land surface areas (CHELSA) provides a high resolution,
430 downscaled centennial climate model data since 20 ka. We used CHELSA-TraCE21k 1 km monthly precipitation time
431 series (Karger et al., 2021). Precipitation data between 22–20 ka was considered the same as 20 ka data. Only snowfall
432 at the mean altitude of each valley was considered glacial accumulation, which occurs when the monthly average
433 temperature is below 0 °C.

434

435 3.4.2 Glacial advance and retreat model based on glacier thickness change

436 Finally, a simple 2D ice surface model reconstructed paleo glacier behavior from 22–16 ka in the study area. First, we
437 created small initial glacial surface profiles on both valleys using the 2D ice surface model developed by Benn and
438 Hulton (2010). The model calculates the ice surface elevation (ice thickness) along the profiles (Fig. 8e) in both valleys.
439 The model only requires an input of the yield stress that is assumed to describe a glacier's basal shear stress regime
440 and a shape factor accounting for the valley-drag effects. We plot the ice profile with 5 m spacing, assuming constant
441 basal shear stress of 50, 100, 150, 200, and 300 kPa. ~~Jargalant glacier is 2.7 times larger in area than Ikh Artsan and
442 twice as long in glacier length, forming a large, deep, and well-developed cirque. The cirque and valley dimensions
443 are a reflection of the intensity of former glacial erosion and size. The normal stress acting on the glacier bed is mainly
444 a result of the weight (thickness) of a glacier. According to the glacial valley size and paleoglacier extent, we chose
445 the higher basal shear stress of initial glacier for Jargalant valley (200 kPa) and the smaller value for Ikh Artsan valley
446 (100 kPa).~~Shape factors were calculated perpendicular to the profile at intervals of 5 m. Subsequently, we calculated
447 the glacier mass balance for 22–16 ka using our temperature-index melt model results and paleo snow accumulation
448 data. Therefore, we applied corresponding paleo mass balance values on the initial ice thickness profiles. Artsan and
449 Jargalant glaciers are mostly developed within a cirque. The maximum erosion related to the rotational movement
450 beneath a cirque is closely linked to the ELA for cirque glaciers (Dahl et al., 2003). Hence, in our modelling, the
451 thickest ice surface related to the maximum erosion was recognized as ELA. Accordingly, paleo ELAs were calculated
452 regarding the ice thickness change. Eventually, we used the simple quadratic function formula ($f(x)=ax^2 + bx + c$) to
453 determine the location of the glacial toe based on ELA and headwall altitude values (Benn and Hulton 2010). With
454 the glacial toe location, we could evaluate the paleoglacier advance and retreat at any time of interest.

455

456 4. RESULTS

457

458 **4.1 Field observation and moraine stratigraphy**

459 In Ikh Bogd, late Quaternary glaciation is almost confined within the cirque, extensive valley glacier
 460 networks are absent. Glaciers in Ikh Artsan and Jargalant catchments are also restricted in the cirques and flowed
 461 shortly down to elevations of ~3000 m a.s.l. Jargalant valley merge down to the largest valley on the northern flank
 462 called Bituut river valley (Fig. 1b; Fig. 5a; Fig. 12c). This large drainage only experienced glaciations in the form of
 463 short cirque-valley glaciers, like in Jargalant valley. The massif was limited to small single (no networking) cirque-
 464 valley glaciers is best explained by the arid climate of the interior of the Gobi Desert.

465 Ikh Artsan cirque is smaller and glacial valley is shorter (~ 1 km) than Jargalant. The best-preserved moraines,
 466 with at least seven to eight morainal crests, occur in the Ikh Artsan cirque (Fig. 4; Fig. 6a; Batbaatar et al., 2018). The
 467 farthest moraine sequence (M_{IA1}) was distinguished by down-valley stratigraphic position and long flat ridge along
 468 the valley side (Fig. 4a). M_{IA1} moraine is composed of thick, unsorted glacial debris of different particle sizes (from
 469 silt to boulder) with huge granitic boulders at the top. Towards the left, the moraine is cut by an intermittent stream,
 470 forming a deep valley (Fig. 4). ~~M_{IA1} moraine is composed of thick, unsorted glacial debris of different particle sizes~~
 471 ~~(from silt to boulder) with huge granitic boulders at the top. Towards the left, the moraine is cut by an intermittent~~
 472 ~~stream, forming a deep valley~~

473 The Jargalant paleoglacier has a larger accumulation area and length than Ikh Artsan glacier, advancing 1.5
 474 km downvalley. The moraine stratigraphy of Jargalant hummocky moraine was quite complicated. The original
 475 moraine surface of the inner moraines has been dissected by longitudinal stream forming the parallel moraine mounds
 476 or elongated moraine ridges along the valley. In the field, we matched such uneroded surfaces (or ridges) with the
 477 similar elevation and assumed them as an individual sequence. Stratigraphically, we identified four different moraine
 478 sequences in the Jargalant complex: M_{J4} , M_{J3} , M_{J2} , and M_{J1} , from youngest to oldest; Fig. 6). M_{J4} , M_{J3} , and M_{J2}
 479 moraines are distinctively separated on the left side of the valley. Elongated moraine feature (M_{J3} , M_{J2}) at the right
 480 side of the valley looks like a single flow feature. However, we assumed that the original form of the moraine
 481 (separation) had been removed or reworked by the stream erosion (Fig. 6c). According to these matters, some moraine
 482 boundaries are still uncertain, hence we marked the boundary with dashed line (Fig.s 5 and 6b, c). M_{J4} moraine lies
 483 between 3365–3410 m a.s.l, containing angular to sub-angular clast-supported pebble to boulders. Downvalley from
 484 the M_{J4} moraine, M_{J3} and M_{J2} moraines have been longitudinally dissected by stream channels, and uneroded moraine
 485 surface forms elongated parallel moraine ridges with smooth matrix-supported flat tops and steep clast-supported sides.
 486 These streams are filled with the till and angular water-lain sediments. The oldest moraine (M_{J1}) was deposited further
 487 downvalley, consisting of a single moraine ridge with large granitic boulders lying on the finer matrix-supported
 488 deposit. We mapped the extent of the most distal moraine ridge from the lower end of M_{J2} moraine to the point where
 489 the slope changes abruptly. We speculate that this oldest moraine may have extended far enough to reach the Bituut
 490 valley; however, beyond this point, moraine would have been reworked by post glacial processes and lateral erosion
 491 of Bituut river (Fig. 5; Fig. 6b, c).

492

4.12. Late Pleistocene ELA reconstruction

LGM ELA was calculated for $M_{th}M_{JA1}$ and M_{J1} moraines (Table 1). We estimated the former ELA using a headwall altitude of 3508–3532 m. The terminal moraine was also identified at an elevation of 3222 m a.s.l in the Ikh ArtsanIkh Artsan valley. Accordingly, the ELA for the $M_{th}M_{JA1}$ moraine was 3388 m a.s.l. In contrast, a large terminal moraine was deposited at 2998 m a.s.l in Jargalant valley. The ELA associated with M_{J1} moraine was 3308 m a.s.l., about 80 m lower than $M_{th}M_{JA1}$ moraine.

4.23. ^{10}Be surface exposure age dating

We present ~~the new~~ new ^{10}Be exposure ages obtained from the boulders associated with five different moraine sequences, $M_{th}M_{JA1}$ in Ikh ArtsanIkh Artsan valley and M_{J1} , M_{J2} , M_{J3} , and M_{J4} ~~sequences~~ in Jargalant (Table 2; Fig. 56).

Ikh ArtsanIkh Artsan valley: seven granitic boulders (IAM001–007) collected from the most distal moraine ridge ranged in age between 21.2 ± 1.5 to 19.1 ± 1.3 ka. ^{10}Be exposure ages from this moraine sequence were well-well- clustered, and none of the three methods (Chauvenet, Pierce, and standardized deviation) detected outliers was detected, yielding a moraine formation group age mean of was found to be $20.1 \pm 0.70.7$ ka (20.1 ± 1.6 ka with total uncertainty), $R\chi^2$ was 0.29, and group relative uncertainty was calculated as 4% (Fig. 67).

Jargalant valley: twenty-one granitic moraine boulders on the four moraine sequences were collected. Five to seven boulders from each moraine crest were sampled. Outliers were detected and rejected by Pierce and normalized deviation criteria. Because, the results from Pierce and normalized deviation methods were consistent, however, Chauvenet method could not recognize some outliers which were recognized by Pierce and normalized deviation criteria. Exposure ages from the innermost M_{J4} moraine ranged from 636.2 ± 45.1 to 177.3 ± 11.3 ka. The oldest age (JAM003, 636.2 ± 45.1 ka) was excluded, and the four remaining ^{10}Be exposure ages provided a mean age of 212.9 ± 4545.9 ka (212.9 ± 47.9 ka with total uncertainty) ~~ka~~. Five boulders from the M_{J3} moraine ranged in age between 209.0 ± 26.1 to 35.9 ± 8.0 ka. The Group-group mean age was calculated as $69.9 \pm 3939.4-4$ ka (69.9 ± 41.5 ka with total uncertainty) ~~ka~~ after rejecting an outlier of 209.0 ± 26.1 ka (JAM008). Boulders from the M_{J2} moraine yielded ages from 284.9 ± 18.4 to 162.1 ± 10.2 ka with a mean exposure age of $193.7 \pm 3636.7-7$ ka (193.7 ± 41.1 ka with total uncertainty) ~~ka~~ after rejecting the oldest age of 284.9 ± 18.4 ka (JAM012). Samples from the distal moraine of Jargalant valley (M_{J1}) ranged in age from 18.9 ± 1.7 to 10.6 ± 0.8 ka. The arithmetic mean age for this moraine sequence was $17.2 \pm 4-51.5$ ka (17.2 ± 2.1 ka with total uncertainty) without the youngest age of 10.8 ± 0.5 ka (JAM016). The Group-group was relatively well clustered, and its relative uncertainty was 9% and $R\chi^2 = 1.18$ (Fig. 67). For erosion rates of 1-4 mm kyr⁻¹, an exposure age of 10 ka calculated assuming zero erosion would underestimate the true age by 1-4% and an age of 20 ka by 2-7%. Samples with longer exposures (boulders with inheritance) older than 100 ka, were increasingly sensitive to erosion; i.e., JAM10 (123.8 ka) had an impact, increasing ages with 12-125% for 1-4 mm kyr⁻¹ and JAM03 (636.2 ka) was saturated even for 1 mm kyr⁻¹ boulder erosion rate.

Our age dating results from most distal moraines of Ikh Artsan (20.1 ± 1.6 ka) and Jargalant (17.2 ± 2.1) coincide within the narrow range (19.2-18.5 ka) as we apply total uncertainties to the group mean. However, T-test reveals (T=3.928, P=0.001) that the exposure ages from the distal moraine of Ikh Artsan presented a statistically

530 significant difference from that of the Jargalant based on standard deviations (variance) of the two groups. Likewise,
 531 the exposure ages of the two groups were different in 0.05 significance level (T=2.665, P=0.044) using total
 532 uncertainties instead of the variance.

533 Boulders from inner moraines (M_{J4}, M_{J3}, and M_{J2}) presented older (~636.2–35.9 ka) exposure than the timing
 534 of the maximum extent unlike morphostratigraphy-the inner moraines should be younger than the distal moraine (M_{J1}).
 535 The unexpected, significant inheritance has been widely recognized around the globe in the previous studies on
 536 cosmogenic nuclides dating (Ciner et al., 2017; more references therein), possibly overestimating the real deposition
 537 age of moraine. We interpret that the unexpected older exposure ages (~636.2–35.9 ka) from M_{J4}, M_{J3}, and M_{J2}
 538 moraines of Jargalant valley strongly imply the inheritance from the summit plateau. These unusually old boulders
 539 are pieces of the summit plateau that were transported onto the glacier surface by rockfall, which seems to happen in
 540 recent times as well. For temperate glaciers, rock fracturing occurs not only on the headwall above the glacier, but
 541 also within the bergschrund (bottom of the headwall) by ice segregation. This kind of undermining (sapping) process
 542 or/and glacial debuitressing would drive consequent upper headwall collapse and give a large amount of rock supply
 543 to the glacier (Sanders et al., 2012; These unusually old boulders are pieces of the summit plateau that were transported
 544 onto the glacier surface by rockfall as the cirque walls were undermined by growing ice, which seems to happen in
 545 the recent times as well (Table 2; Fig. 5b6b, Fig. 11). ¹⁰Be concentration of the oldest sample (JAM003 with ¹⁰Be
 546 concentration of ~262.9×10⁵) likely represents nuclide concentration at the surface of the summit plateau. The
 547 production rate for the summit plateau (60.49 atoms g⁻¹ yr⁻¹) must be higher than the moraine samples (38.45 atoms
 548 g⁻¹ yr⁻¹) due to its higher elevation (3625 m) than sampling sites and 100% exposure (topographic shielding is 1) to
 549 cosmic-ray bombardment. The older version of Cronus Earth (V2.3) provides the production rate (referenced to Lal
 550 (1991)/Stone (2000) scaling scheme for spallation) of 60.49 atoms g⁻¹ yr⁻¹ for summit plateau and 38.45 atoms g⁻¹ yr⁻¹
 551 for sampling site (average production rate of all sampling points including Ikh Artsan and Jargalant). With a high
 552 ¹⁰Be concentration of JAM003 and production rate of summit plateau (3625 m a.s.l), the assuming exposure age of
 553 the flat summit plateau was calculated as 442.3 ± 29.8 ka, and the corresponding erosion rate was calculated as 1.23
 554 ± 0.10 mm kyr⁻¹. ~~The unexpected, significant inheritance has been widely recognized around the globe in the literature~~
 555 ~~of cosmogenic nuclides dating (Ciner et al., 2017; more references therein), possibly overestimating the real age of~~
 556 ~~moraine.~~

557

5. THE 2D ICE SURFACE MODELLING: METHODS AND RESULTS

Our original hypothesis was that the north and south facing cirques of the Ih Bogd massif would be concordant. The results were that the glaciers on the opposite aspects were asynchronously behaved, by about 3 millennia. These findings led to a second hypothesis, that aspect might provide enough of a difference to explain the asynchrony. Thus, to stay true to the research events, we combine methods and results of simulating a simple 2D ice surface model including mass balance calculation covering the time period of 22–16 ka. Our exercise cannot simulate actual glaciers, however, rather simply assess the idea that aspect might produce enough of a difference in mass balance and ice surface via different melt rates to explain the empirical dating results.

5.1. Glacial surface mass balance model

Glacier mass balance (m) is determined by the summation of net accumulation (c) and ablation (a) over a stated period (t):

$$m = c - a = \int_{t_1}^{t_2} (c - a) dt \quad (1)$$

To infer the net gain and loss of glacier mass along the longitudinal profile (Fig. 7a, b, c) for both catchments, we calculated and plotted the variations in summer (JJA) mean melt rate and winter precipitation (i.e., snow in the whole year) during 22–16 ka ago. Site parameters and input parameters of this model are described in Tables 3 and 4.

5.1.1 Temperature-index glacier melt model including potential clear-sky direct solar radiation

We calculated time dependent incoming solar radiation of the study area by applying the potential clear-sky direct solar radiation method to a 12.5 m resolution DEM to realize the aspect effect on insolation distribution in mountainous areas. For simplicity, we rerun this insolation model along a longitudinal profile line drawn for Ih Artsan and Jargalant glacial valleys (Fig. 7). Subsequently, we combined the insolation values with the temperature-index melt model. To calculate melt, we used a series of equations in the following steps, calculating: 1) orbital parameters; 2) topography; 3) hour angle on an arbitrary inclined surface and day length; 4) local zenith angle and angle of incidence with hour interval; 5) hourly insolation; 6) integrate hourly insolation into daily insolation; 7) daily melt; and 8) summer (JJA) melt integration for given time of interval (22–16 ka).

The earth's rotation around its axis causes the diurnal changes in incoming solar radiation; the position of this axis relative to the sun causes seasonal changes; the variations in eccentricity, axial tilt, and precession cause combined to result in long-term cyclical changes in climate. Correspondingly, two main orbital parameters, solar declination (δ) and eccentricity correction factor $(R_m/R^{-1})^2$ were used for the calculation of the further paleo-solar radiation for 22–16 ka (Berger and Loutre, 1991).

According to the aspect effect, north-facing slopes must receive less direct solar radiation than south-facing slopes in the mid-latitude northern hemisphere. To define aspect-driven contrast in potential direct solar radiation between south-facing and north-facing valleys, we applied the same input parameters, except for the topography (aspect and slope). Sunrise and sunset hour angles on the inclined surface were calculated as a function of latitude, solar declination, slope, and azimuth (Iqbal, 1963).

595 Sunrise hour angle for horizontal surface:

$$596 \omega_s = \cos^{-1}(-\tan\phi \tan\delta) \quad (2)$$

597

598 To obtain hour angles on the inclined surface, x and y were extracted from formula 1.6.7 created by Iqbal (1963):

$$599 x = \frac{\cos\phi}{\sin\gamma \tan\beta} + \frac{\sin\beta}{\tan\gamma} \quad (3)$$

600

$$601 y = \tan\delta \left(\frac{\sin\phi}{\sin\gamma \tan\beta} - \frac{\cos\phi}{\tan\gamma} \right) \quad (4)$$

602

603 The following equations give the sunrise and sunset hour angles on the surface oriented toward the east.

$$604 \omega_{sf} = \min \left[\omega_s, \cos^{-1} \left(\frac{-xy + \sqrt{x^2 y^2 + 1}}{x^2 + 1} \right) \right] \quad (5)$$

605

$$606 \omega_{ss} = \min \left[\omega_s, \cos^{-1} \left(\frac{-xy + \sqrt{x^2 y^2 + 1}}{x^2 + 1} \right) \right] \quad (6)$$

607

608 The following equations give the sunrise and sunset hour angles on the surface oriented toward the west.

$$609 \omega_{sf} = \min \left[\omega_s, \cos^{-1} \left(\frac{-xy + \sqrt{x^2 y^2 + 1}}{x^2 + 1} \right) \right] \quad (7)$$

610

$$610 \omega_{ss} = \min \left[\omega_s, \cos^{-1} \left(\frac{-xy + \sqrt{x^2 y^2 + 1}}{x^2 + 1} \right) \right] \quad (8)$$

611 Equations 2 to 8 are for calculating hour angles in arbitrary surfaces, where ω_s is the sunrise hour angle for
612 horizontal surfaces, ω_{sf} , ω_{ss} is the sunrise and the sunset hour angles on the inclined surface, ϕ is the latitude, δ is the
613 solar declination angle, β is the slope inclination angle, and γ is the surface azimuth angle.

614 Furthermore, the local zenith angle (Z) and the angle of incidence (θ) were calculated using a one hour
615 interval of hour angle (ω). The zenith angle is approximated as a function of latitude, solar declination angle, and hour
616 angle (Iqbal, 1983):

617

$$618 Z = \sin\delta \sin\phi + \cos\delta \cos\phi \cos\omega \quad (9)$$

619

620 and the angle of incidence on the arbitrary oriented surfaces is expressed as:

621

$$622 \cos\theta = (\sin\phi \cos\beta - \cos\phi \sin\beta \cos\gamma) \sin\delta + (\cos\phi \cos\beta + \sin\phi \sin\beta \cos\gamma) \cos\delta \cos\omega + \cos\delta \sin\beta \sin\gamma \sin\omega \quad (10)$$

623

624 where β is the slope inclination angle and γ is the surface azimuth angle.

625 Hourly potential clear sky direct solar radiation (I) during daytime is calculated as (Hock, 1999):

$$627 I = I_0 \left(\frac{R_{in}}{R} \right)^2 \Psi_a \left(\frac{P}{P_0 \cos Z} \right) \cos\theta \quad (11)$$

where I_0 is solar constant (1368 W m^{-2}), $(R_m/R)^2$ is the eccentricity correction factor of the Earth's orbit for the time considered with R the instantaneous Sun Earth distance, and R_m is the mean Sun Earth distance, Ψ_a is the mean atmospheric clear sky transmissivity ($\Psi_a=0.75$: (Hock, 1998)), P_h is the atmospheric pressure (OAF, 1976), P_0 is the mean atmospheric pressure at sea level, Z is the local zenith angle, and θ is the angle of incidence between the normal to the grid slope and the solar beam. Daily solar radiation resulted from integration of hourly solar radiation for each day

We calculated daily melts with equation (12) and integrated them into annual summer melt.

$$a = \begin{cases} \left(\frac{1}{m} MF + a_{ice} I \right) T & : T > 0 \\ 0 & : T \leq 0 \end{cases} \quad (12)$$

MF is a melt factor ($\text{mm d}^{-1} \text{ } ^\circ\text{C}^{-1}$), a_{ice} is a radiation coefficient for ice surfaces, I is potential clear sky direct solar radiation at the ice surface (W m^{-2}), and T is the monthly mean temperature ($^\circ\text{C}$).

We calculated the paleotemperature of the study area in the following order.

1st) Present day monthly air temperatures (T) for both cirque headwall altitudes (3533.3 m in Jargalant, 3508.3 m in Ih Artsan) were calculated from the two nearest national weather stations using a summer adiabatic lapse rate of $8 \text{ } ^\circ\text{C km}^{-1}$ (Batbaatar et al., 2018). Bayangobi weather station locates (1540 m a.s.l) ~27 km SE and Bogd (Horiult) weather station (1240 m a.s.l) is ~45 km NE from the study area (Fig. 2c).

2nd) We use only summer temperature because even today, monthly mean temperatures between August to May are less than $0 \text{ } ^\circ\text{C}$, in which no melt occurs (NAMEM, 2020). Present day precipitation falls as snow between the end of September to the middle of April. Sometimes it snows even in summer (Landsat imagery, Farr et al., 2007). The summer mean temperature (JJA) at the cirque headwall altitude was measured as $3.5 \text{ } ^\circ\text{C}$ in Jargalant valley and $5.4 \text{ } ^\circ\text{C}$ in the Ih Artsan valley. We chose the value of $5.4 \text{ } ^\circ\text{C}$ for the summer temperature of the study area and used further calculations (see supplementary 1 file).

3rd) We obtained a time dependent summer temperature since 22 ka. LGM summer temperature was easily calculated by subtracting known LGM summer temperature anomaly ($1-7 \text{ } ^\circ\text{C}$ by Tarasov et al., 1999) from the present day temperature of the study area. The study area's present day and LGM summer temperature was calibrated to Greenland temperature data (from NGRIP ice core) since 22 ka (Buizert et al., 2018) to obtain time dependent temperature variation (see supplementary 2 file).

4th) LGM summer temperature anomalies ranging from $-5.0 \text{ } ^\circ\text{C}$ to $-6 \text{ } ^\circ\text{C}$ were applied to calculate glacial melt since 22 ka (see supplementary 2 file).

5.1.2. Glacier accumulation and snow data

Climatologies at high resolution for the earth's land surface areas (CHELSA) provides a high resolution, downscaled centennial climate model data since 20 ka. We used CHELSA TraCE21k 1 km monthly precipitation time series (Karger et al., 2021). Precipitation data between 22-20 ka was considered the same as 20 ka data. Only snowfall at

the mean altitude of each valley was considered glacial accumulation, which occurs when the monthly average temperature is below 0°C.

5.2. 2D ice surface model based on glacier thickness change

Finally, a simple 2D ice surface model reconstructed paleo glacier behavior from 22–16 ka in the study area. First, we created small initial glacial surface profiles on both valleys using the 2D ice surface model developed by Benn and Hulton (2010). The model calculates the ice surface elevation (ice thickness) along the profiles (Fig. 7a, b, c) in both valleys. The model only requires an input of the yield stress that is assumed to describe a glacier's basal shear stress regime and a shape factor accounting for the valley drag effects. We plot the ice profile with 5 m spacing, assuming constant basal shear stress of 50, 100, 150, 200, and 300 kPa. According to the glacial valley scale and paleoglacier extent, we chose the higher basal shear stress of initial glacier for Jargalant valley (200 kPa) and the smaller value for Ikh Artsan valley (100 kPa). Shape factors were calculated perpendicular to the profile at intervals of 5 m. Subsequently, we calculated the glacier mass balance for 22–16 ka using our temperature index melt model results and paleo snow accumulation data. Therefore, we applied corresponding paleo mass balance values on the initial ice thickness profiles. A cross section of the thickest ice was recognized as ELA. Accordingly, paleo ELAs were calculated regarding the ice thickness change. Eventually, we used the simple quadratic function formula ($f(x) = ax^2 + bx + c$) to determine the location of the glacial toe based on ELA and headwall altitude values (Benn and Hulton 2010). With the glacial toe location, we could evaluate the paleoglacier advance and retreat at any time of interest.

5.4.34. Results from 2D ice surface modelling result

We ran the potential direct solar radiation model applying to a 12.5 m resolution DEM for a more realistic comparison. The model suggests that the aspect largely affects the incoming potential clear-sky solar radiation. The result approved that the south-facing slopes in mountainous regions receive more significant solar radiation than the north-facing slope in the northern hemisphere our study area. At solar noon, the sun is always directly south in the northern hemisphere, hence southern slopes of the mountainous area receive their maximum insolation. However, the orientations of the two valleys are not true north or south. The azimuth of the Ikh Artsan is 247° (SSW) and for the Jargalant it is 40° (NNE). According to the exact orientation (aspect) of the valleys (northeast to southwest), the peak of the hourly daily maximum insolation contrast between two valleys is calculated between Ikh Artsan and minimum insolation in Jargalant were observed between 15:30 to 16:40 o'clock pm, not at noon. The present day current June solstice incoming daily solar radiation in Ikh Artsan was 8527.34 WH m⁻² and in Ikh Artsan valley and 7714.35 WH m⁻² in Jargalant valley, but whereas the solar radiation was smaller lower in 22 ka, 8460.07 WH m⁻² in Ikh Artsan, and 7604.54 WH m⁻² in Jargalant. Although both valleys received maximum insolation in the first to middle half of June, the maximum difference in incoming daily solar radiation occurred at the end of August. The main difference in the daily incoming solar radiation ranges from 10–24% in on summer days over the period 22–16 ka. The spatial distribution of potential direct solar radiation of the study area is given in Fig. 78. Typically, the total daily insolation anomaly of summer solstice in 20 ka for from present-day and integrated total daily insolation

699 ~~for 22-16 ka~~20 ka (Fig. 7a), ~~summer insolation for thousand years (21–20 ka), and total summer insolation over 22–~~
 700 ~~16 ka was were~~ described on the 12.5 m grid cells (Fig. 8d, e). In the same way, 14% excess of total summer insolation
 701 was observed on the southern slope during ~~the over~~-modelling time interval of 22–16 ka (Fig. 78b, ef, ; see
 702 supplementary 2 file).

703 For simplicity, the melt was calculated (Eq. 12) along ~~specific valley profiles~~ of ~~Ih Artsan~~Ikh Artsan and
 704 Jargalant valleys (Fig. 78e, f). In accordance with the incoming solar radiation contrast, melt rates on south-facing
 705 slopes exceed those on north-facing slopes, as would be expected. If modern glaciers existed in ~~Ih Bogd~~Ikh Bogd, the
 706 present-day summer melt would be calculated as 4.02 m in ~~Jargalant-Ikh Artsan~~ valley and 3.7 m in ~~Ih Artsan~~
 707 ~~valley~~Jargalant, respectively. This was a substantially higher melt rate in the arid, cool climate of the study area. The
 708 temperature-index melt model discovered that 5% of melt excess in June solstice of any year between 22–16 ka was
 709 observed on the south-facing slope. Approximately 8% of the difference in summer melt in any year was observed
 710 during 22–16 ka (Fig. 78f, see supplementary 2 file)

711 ~~We run our 2D ice surface model for many times using different values of basal shear stress, LGM summer~~
 712 ~~temperature anomalies, and site temperature (Supplementary material 2). The cirque and valley dimensions reflect the~~
 713 ~~glacier size (including thickness) and the intensity of former glacial erosion (Barr and Spagnolo, 2015). The normal~~
 714 ~~stress acting on the glacier bed is mainly a result of the weight (thickness) of a glacier. Jargalant glacier is 2.7 times~~
 715 ~~larger in area than Ikh Artsan and twice as long in glacier length, forming a large, deep, and well-developed cirque.~~
 716 ~~According to the glacial valley size, we chose the higher basal shear stress for Jargalant valley (200 kPa) and the~~
 717 ~~smaller value for Ikh Artsan valley (100 kPa). Except for the present day temperature and topographic data, the same~~
 718 ~~input parameters were applied to both valleys. LGM summer temperature anomalies ranging from -6 °C to -5 °C with~~
 719 ~~0.1 °C intervals were applied the same for both glaciers. We used input parameter of 100 kPa of basal shear stress~~
 720 ~~for Ih Artsan initial glacier (22 ka), while a twofold value (200 kPa) for Jargalant in proportion to the size of the~~
 721 ~~glaciers. Some previous studies suggest that temperature is lower on the north-facing slopes at the same altitude. On~~
 722 ~~the north-facing slope of Taibai, Qinling mountains, JJA monthly mean temperature is measured 0.5–1 °C lower than~~
 723 ~~on the south-facing slope in the altitude range of 1250–3750 m (Tang & Fang, 2006). Therefore, we applied two~~
 724 ~~different present day temperature values for the north-facing Jargalant glacier, but LGM summer temperature~~
 725 ~~anomalies were the same for both cases. We ran the 2D ice surface model from 22 ka to 16 ka with two cases~~
 726 ~~according to the different temperature inputs: 1) using the same present-day temperature with Ikh Artsan valley; and~~
 727 ~~2) using the different lower present-day temperature for both Jargalant valleys valley than Ikh Artsan.~~

728 **Case 1.** Applying the same present-day temperature: ~~The timing of maximum extent was similar for both~~
 729 ~~valleys when using the same site temperature. When we give use the same present-day temperature and the same LGM~~
 730 ~~anomaly of -5.5 °C, the modelled timing chronology of the maximum extents (20.23 ka) for both valleys of two glaciers~~
 731 ~~were similar and consistent with the Ih Artsan Ikh Artsan terminal moraine age dating result (20.1 ka).~~

732 **Case 2.** Applying the different present-day temperatures: For the Jargalant glacier, we applied lower present-
 733 day temperature by -1 °C to -0 °C (at 0.1 °C interval) than ~~Ih Artsan~~Ikh Artsan. The run yielded different chronologies
 734 of maximum ice expansions. ~~Only a small temperature change between the south- and north-facing slope forced two~~
 735 ~~glaciers behave asynchronously, the north-facing glacier got have The gaps between maximum ice advance timings~~

736 ~~range from~~ 2.70–3.46 kyr of lag in the timing of the maximum extent. When we applied -5.5 °C of LGM summer
737 temperature anomaly and present-day summer temperature in Jargalant 0.5 °C lower than in ~~Ih-Artsan~~Ikh Artsan, ~~Ih~~
738 ~~Artsan~~Ikh Artsan glacier reached its maximum extent near 20.2~~3~~ ka. In contrast, the Jargalant glacier maximally
739 advanced approximately at 17.1~~3~~ ka. This result perfectly fits our ¹⁰Be moraine age dating results (20.1 ka and 17.2
740 ka).

65. DISCUSSION

6.1. Asynchrony in LGM ice expansion across the western Mongolia

Our study shows the glaciers of Ih Artsan valley reached its maximum extent during gLGM at 20.1 ± 0.7 ka. Several inner moraine ridges (Fig. 5a) were recognized and some of them dated to 15–13 ka (Batbaatar et al., 2018).

In the other hand, our study also documents the farthest found moraine (M_{J1}) in Jargalant valley formed around 17 ka (17.2 ± 1.5 ka), three millennia later than the south facing Ih Artsan valley. We could not find any other evidence that the Jargalant glacier reached the trunk valley of Bituut river. Probably geological markers could have been erased by the main river of Bituut or earlier advances were less extensive. However, we suggest the exposure age (17.2 ± 1.5 ka) of the distal moraine (M_{J1}) is the age for maximum extent for the Jargalant valley (Fig. 5b and 6), because this moraine was not like the small ridge left as a glacier stagnates during its retreat. The M_{J1} moraine was larger than the other moraine sequences, large enough to mark the maximum advance of the glacier.

Some ^{10}Be exposure ages of the glacial erratic from the mountain ranges nearby Ih Bogd show the significant glacial advances between LGM to the Holocene (Fig. 8). The largest ice extent was dated as ~ 22.0 ka on the western flank of the Sutai (Batbaatar et al., 2018). On the other hand, the farthest ice expansion corresponds to MIS 3 in the Khangay mountain range (Batbaatar et al., 2018; Pötsch, 2017; Smith et al., 2016; Rother et al., 2014). In the Gichene mountains, Holocene (8–7 ka) glaciers advanced with a similar magnitude to their local LGM position. Generally, two main glacial stages, LGM and post-LGM (~ 17 –16 ka), were observed within MIS 2 in Mongolia (Batbaatar et al., 2018; Pötsch, 2017; Batbaatar and Gillespie, 2016; Smith et al., 2016; Rother et al., 2014).

A suite of granulometric, palynological, ostracod, and geochemical proxies from the Gobi Lakes Valley reveal several harsh and dry climates, including the local LGM (19–18 ka) and Younger Dryas (Mischke et al., 2020; Yu et al., 2019; Lehmkuhl et al., 2018; Yu et al., 2017; Lee et al., 2013; Felauer et al., 2012, Fig. 8). Abrupt deglaciation occurred near 20 ka in Ih Artsan valley, whereas the lower boundary of deglaciation likely began at 17.2 ka on Ih Bogd's northern slope (Jargalant). The warming trend was also present in the Gobi Lakes Valley, where lakes once were desiccated during local LGM, and experienced water level increase after local LGM (e.g., Mischke et al., 2020; Yu et al., 2017).

65.21. Asynchronous LGM glaciation in other mid-latitude ranges

Recent glacial chronologies from mid-latitude mountain ranges in North Atlantic region document that Laurentide, Scandinavian ice sheets and number of valley glaciers behaved synchronously, advancing to their maximum extent at roughly the same time as the gLGM (26.5–19 ka). However, some experienced pre-LGM glacial maxima, while others stagnated, re-advanced, continuously advanced even farther during the subsequent Heinrich Stadial 1 (HS-1, 17.5–14.5 ka), displaying both inter-range and intra-range asynchrony (Palacio et al., 2020; Licciardi and Pierce 2018; Young et al., 2011, Laabs et al., 2009).

In Europe, Large-large-scale inter-range asynchrony (several tens of kyr) of last glacial termination was common in Europe. Cosmogenic surface dating from Alps and Turkey provides nearly synchronous last glacial maxima with the gLGM (26.5–19 ka, MIS 2), whereas Whereas other numerical dating techniques including

778 radiocarbon, U-series, and OSL indicate earlier local glacial maxima (80–30 ka, MIS 4 to MIS 3) in the Cantabrian
 779 Mountains, Pyrenees, Italian Apennines and Pindus Mountains (e.g., Oliva et al., 2019; Jimenez-Sanchez et al., 2013).
 780 Another inter-range asynchrony was observed in mountain glaciers of North America. They reached their maximum
 781 extent from as old as 25–24 ka for some moraines and outwash in the Sierra Nevada to as young as 17–15 ka for some
 782 terminal moraines in the Rocky Mountains but a clear central tendency exists with a mean of ~19.5 ka (Laabs et al.,
 783 2020; Palacios et al., 2020; Young et al., 2011). Relatively younger ages (HS-1) across the mountains located in the
 784 higher latitude were interpreted as a sign of **glacial post-LGM culmination** in response to increased delivery of westerly
 785 derived moisture which reached the northern continental interior of the western U.S after the large ice sheets started
 786 to retreat (Thackray, 2008, Licciardi et al., 2004, Licciardi et al., 2001). For instance, younger exposure ages of the
 787 last glacial maxima in the western Uinta mountains, compared to mountain ranges farther east and north, reflected the
 788 influence of pluvial Lake Bonneville after the recession of Laurentide ice sheet to the north (Laabs et al., 2009).

789 Medium scale inter-range asynchrony (several thousand years) was observed in the Yellowstone plateau.
 790 Terminal moraines dated to ~17 ka are common in valleys along the north eastern mountains (e.g., Eightmile, Chico,
 791 Pine Creek, S.Fork Deep Creek, Cascade Canyon and Gallatin) of the Great Yellowstone plateau. Glaciers in the
 792 Teton Range (south western part of the plateau) have terminal moraine with the age of ~15 ka. Local LGM maxima
 793 dated to ~19.8 to 18.2 ka in the western part of the plateau (Beartooth Uplift). Licciardi and Pierce (2018) suggested
 794 that shifting orographic precipitation pattern due to the formation of ice dome and change in ice flow direction caused
 795 asynchrony in the Great Yellowstone region.

796 ~~No or v~~Very ~~few small number of~~ glacial chronologies, ~~if any at all, document record~~ intra-range asynchrony
 797 ~~for during~~ the ~~latest-most recent~~ glacial termination. Age dating results from some relatively well-studied mountain
 798 ranges (Wasatch, Uinta, Bighorn ranges in North America) present ~~that~~ intra-range asynchrony in glacial maxima in
 799 their various aspect (Laabs et al., 2020). Some of them had LGM age ranging from hundreds to thousands of years
 800 from valley to valley. In the Wasatch range, terminal moraines dated to ~21.9 ka (Laabs and Munroe, 2016), ~20.8
 801 ka, 17.3 ka (Laabs et al., 2011) in three western valleys, 19.6 ka in the southwestern valley and 17.6 ka ~~and~~ 17.3 ka
 802 in the southeastern valleys (Quirk et al., 2020). Similarly, last glacial terminal moraine age difference of ~1 kyr was
 803 observed between north-facing and south-facing slope, Eastern Pyrenees (Delmas et al., 2011; Delmas et al., 2008).
 804 Even glaciers on the same oriented slope contain some chronology difference. LGM moraine chronology from the
 805 three valleys on the east side of the central Sawatch range varies from 22.3 ka to 19.9 ka (Young et al., 2011).

806 Nevertheless, we suggest that some internal, external, analytical uncertainties associated with sampling,
 807 measurements, or/and statistical approach can cause the low magnitude of asynchrony in such small intra-range or
 808 massif. Some studies have attributed intra-range asynchrony in terminal moraine ages to contrasting valley glacier
 809 response times related to topography, ice dynamics and/or differences in glacier shape and hypsometry (Young et al.,
 810 2011, Licciardi and Pierce, 2018). As mentioned above, large and ~~medium-medium~~-scale asynchrony in the mountain
 811 glaciers across the North Atlantic region mostly explained by precipitation distribution due to the relative location of
 812 the moisture source area and atmospheric circulation contributed by topography. However intra-range or intra-massif
 813 scale of asynchrony in last glacial period needs further research to ~~be fully~~ understood fully.

814

815
816
817
818
819
820
821
822
823
824
825
826
827
828
829
830
831
832
833
834
835
836
837
838
839
840
841
842
843
844
845
846
847
848
849
850

5.2. Inter-range asynchrony in ice expansion of last glacial cycle across the western Mongolia

Some ^{10}Be exposure ages of the glacial erratic from the mountain ranges nearby Ikh Bogd show the significant glacial advances between LGM to the Holocene (Fig. 9). The largest ice extent was dated as ~22.0 ka on the western flank of the Sutai (Batbaatar et al., 2018). On the other hand, the farthest ice expansion corresponds to MIS 3 in the Khangai mountain range (Batbaatar et al., 2018; Pötsch, 2017; Smith et al., 2016; Rother et al., 2014). In the Gichgeniyn mountains, Holocene (8–7 ka) glaciers advanced with a similar magnitude to their local LGM position. Generally, two main glacial stages, LGM and post LGM (~17–16 ka), were observed within MIS 2 in Mongolia (Batbaatar et al., 2018; Pötsch, 2017; Batbaatar and Gillespie, 2016; Smith et al., 2016; Rother et al., 2014).

Previous studies using granulometric, palynological, ostracod, and geochemical proxies from the Gobi Lakes Valley reveal occurrence of harsh and dry climates, during the local LGM (19–18 ka) and Younger Dryas (Mischke et al., 2020; Yu et al., 2019; Lehmkuhl et al., 2018; Yu et al., 2017; Lee et al., 2013; Felauer et al., 2012; Fig. 9). The results are consistent with our exposure ages from two valleys within total uncertainty range. The warming trend was also present in the Gobi Lakes Valley, where lakes once were desiccated during local LGM, and experienced water level increase after local LGM (e.g., Mischke et al., 2020; Yu et al., 2017).

6.3. Aspect effect on the asynchronous maximum glacier extent glacial dynamic in Ikh Bogd

Our age dating result reveals that abrupt deglaciation occurred since ~20 ka in the Ikh Artsan glacier. Exposure ages from M_{II} moraine (~17 ka) should represent one of the following: glacier culmination, survival or temporary glacial stagnation of the LGM glacier or glacier re-advance. In either case, culmination of the Jargalant glacier near 17 ka implies a major difference in glacier mass balance between south- and north-facing glaciers. Changes in glacier mass balance in small massif or mountain (intra-range) could show large spatial variation due to local topography (aspect) induced factors: i) snow avalanching, ii) preferential deposition of wind-drifted snow (Florentine et al., 2020), iii) solar radiation, and iv) temperature.

i. Periodically occurring snow avalanches support glacial accumulation. Most avalanches have steep slopes between 25° and 50° to slide down (Luckman, 1977). Ikh Artsan and Jargalant valleys are connected to the flat summit plateau and are less steep than the threshold slope of 25°. The average slope was measured as 23° for Jargalant and 18.2° for Ikh Artsan. Very wet snow lubricated with water can cause an avalanche on a slope of only 10 to 25° (Luckman, 1977). However, it is not significantly relevant to our study area because Ikh Bogd and its neighboring area experienced very cold and dry conditions during MIS 2 (e.g., Yu et al., 2019).

ii. Wind-drifted snow accumulation occurs either with or without snowfall. Wind deflates the snow from the windward slope and redistributes it into the leeward slope. However, the prevailing wind direction of the study area is northwest to southeast, which is almost perpendicular to the orientations of the two valleys. We assume the wind direction during MIS 2 was similar to the present with much strength. Therefore, wind-drifted snow may not significantly affect glacier accumulation. For that reason, we used the same precipitation value in both valleys.

851 iii. North-facing slopes in the northern hemisphere receive less solar radiation because of the aspect effect. Ikh Bogd
 852 locates in a mid-latitude great sunlight climate; furthermore, it has steeper relief which can enhance the aspect
 853 effect. (Evans and Cox, 2005). Topographic shading can also influence glacier response and mass balance in
 854 mountainous areas (Olson and Rupper, 2019). As expected, our modelling results demonstrate that the north-
 855 facing slope receives less summer insolation than the south-facing slope, resulting in reduced glacial melt (5-10%)
 856 under the same temperature conditions.

857 iv. The vegetation, discontinuous permafrost, and modern and paleo glacier distribution and their magnitude in semi-
 858 arid mid-latitude regions have contrasting temperatures and soil moisture on sunny and shady slopes (Barr and
 859 Spagnolo, 2015; Evans 2006; Klinge et al., 2021). As a result of topographically induced differences of solar
 860 radiation and evapotranspiration, forests (consisting of Siberian larch) and discontinuous permafrost are limited
 861 to north-facing slopes, whereas mountain steppe covers south-facing slopes in Mongolian forest-step zone (Klinge
 862 et al., 2021; Fig. 8b, c). Klinge et al. (2021) determined that the annual incoming solar radiation, permafrost table
 863 depth, and soil moisture (topographic wetness index) are significantly correlated. Aspect-driven solar radiation
 864 and temperature contrast also give more glacier, lower (altitude) glacier, and larger glacier on the poleward slope
 865 (e.g., Barr and Spagnolo, 2015; Evans 2006). For instance, Sutai mountain (closest modern glacier to Ikh Bogd)
 866 has large, well-developed valley glaciers flow northward into low altitude from the ice dome, but the glaciers at
 867 the south-facing slope end near the summit margin without developing into valley glaciers (Fig. 8c). According
 868 to these facts, a small temperature difference is likely to be real and needs to be considered. Our temperature
 869 index melt model revealed that applying lower temperature to the north-facing glacier than to the south-facing
 870 glacier results in a large melt difference between the two valleys.

871
 872 Among the four topography-aspect induced factors, two are applicable on our study area; incoming solar radiation
 873 and temperature difference in south- and north-facing slopes. Our temperature index melt model suggests that an
 874 aspect-driven insolation change affects the amount of melt, however in a very small amount. This small reduction in
 875 the melt due to the shading effect could not cause a significant difference in glacial mass balance or long-term glacier
 876 stagnation or advance. Under the same temperature and different insolation, glaciers on the south- and north-facing
 877 slopes across small regions behave almost synchronously. Both Ikh Artsan and Jargalant glaciers ~~reached their~~
 878 ~~maximum extent~~culminated near 20.2 ka and abruptly retreated to the cirque headwall. Also, their changes in glacial
 879 dynamic were almost the same (See supplementary 2 file). However, no glacier stagnation observed in the Jargalant
 880 valley around 17 ka (i.e., this result does not match our exposure age dating). We sampled from possible most distal
 881 moraine from Jargalant valley to avoid sampling from of reworked boulders in the steep slope. Likewise, we could
 882 not find any other evidence that the Jargalant glacier reached the trunk valley of the Bituut river. If we consider both
 883 glaciers moved synchronously, the most distal moraine must locate more downvalley from the ~17 ka culmination. In
 884 this case, the geological evidence (terminal moraine) near 20 ka must have been degraded by Bituut mainstream or/and
 885 reworked with the mass movement.

886 When we set the site temperature of Jargalant slightly colder (-0.1 to -1 °C) than in the Ikh Artsan, glaciers started
 887 to behave differently, i.e., retreat from their distal location asynchronously. When we apply 0.5 °C colder temperature

888 to Jargalant than Ikh Artsan, 2D ice surface modelling results are consistent with age dating results. The Ikh Artsan
 889 glacier abruptly retreated from its maximum extent near 20.2 ka (age dating result was 20.1 ka). In contrast, the
 890 Jargalant glacier advanced almost continuously until 17.8 ka and then began to retreat from its maximum extent by
 891 17.1 ka (age dating result was 17.2 ka) with brief stagnation around its maximum extent. This result suggests that the
 892 exposure age of ~17 ka corresponds to the most extensive glaciation in Jargalant valley. We also assume that the
 893 exposure age (17.2 ± 1.5 ka) of the distal moraine (M_{J1}) is the age for maximum extent for the Jargalant valley (Figs.
 894 6b and 6c), because this moraine was not like the small ridge left as a glacier stagnates during its retreat. The M_{J1}
 895 moraine was larger than the other moraine sequences, large enough to mark the maximum advance of the
 896 glacier. Previous research indicates that the retreat or advance pattern of glaciers in some regions is not necessarily
 897 expected to be uniform, coincidental, or synchronous with the primary factors (Fig. 8). Based on proxies from
 898 lacustrine (Orog) sediment cores, the local LGM ranges between 19 and 18 ka near the Ih Bogd massif (Yu et al.,
 899 2017; Yu et al., 2019). However, deglaciation started in Ih Artsan valley (south-facing) nearly a thousand years earlier
 900 (20.1 ± 0.7) than local LGM. For the Jargalant valley (north-facing), we could not find the actual evidence of the latest
 901 deglaciation. If we consider both glaciers moved synchronously, the geological evidence (terminal moraine) near 20
 902 ka must have been degraded by Bituut mainstream or/and reworked with the mass movement. Contrary, if the Jargalant
 903 glacier advanced maximally near 17.2 ka based on exposure age dating, deglaciation must have begun 3000 years
 904 later in Jargalant valley than in Ih Artsan valley. In this case, the most extensive glacial extent in Jargalant valley
 905 should represent LGM glacial survival or significant glacial re-advance near 17 ka as the same as glacier advance in
 906 Mongolia and North Atlantic region during HS 1.

907 Based on the age dating and 2D ice surface modelling, we propose that the glaciers on the north- and south-
 908 facing slopes of Ikh Bogd may have behaved asynchronously. In either case, changes in glacier mass balance in small
 909 massif or mountain (intra-range) could show large spatial variation due to local topography driven climatic factors: 1)
 910 snow avalanching, 2) preferential deposition of wind drifted snow (Florentine et al., 2020), 3) solar radiation, 4)
 911 temperature.

912 i.—Periodically occurring snow avalanches support glacial accumulation. Most avalanches have steep slopes between
 913 25° and 50° to slide down (Luckman, 1977). Both valleys are connected to the flat top and are less steep than the
 914 threshold slope of 25° ; Jargalant valley is 23° for Jargalant and 18.2° for Ih Artsan. Very wet snow lubricated
 915 with water can cause an avalanche on a slope of only 10 to 25° (Luckman, 1977). However, it is not significantly
 916 relevant to our study area because Ih Bogd and its neighboring area experienced very cold and dry conditions
 917 during MIS 2 (e.g., Yu et al., 2019).

918 ii.—Wind drifted snow accumulation occurs either with or without snowfall. Wind deflates the snow from the
 919 windward slope and redistributes it into the leeward slope. However, the prevailing wind direction of the study
 920 area is northwest to southeast, which is the almost perpendicular direction to the orientations of the two valleys.
 921 We assume the wind direction during MIS 2 was similar to the present with much strength. Therefore, wind
 922 drifted snow may not significantly affect glacier accumulation. For that reason, we used the same precipitation
 923 value in both valleys.

924 ~~iii. North facing slopes in the northern hemisphere receive less solar radiation because of the aspect effect. Ih Bogd~~
 925 ~~locates in a mid-latitude great sunlight climate; furthermore, it has steeper relief which can enhance the aspect~~
 926 ~~effect. (Evans and Cox, 2005). Topographic shading can also influence glacier response and mass balance in~~
 927 ~~mountainous areas (Olson and Rupper, 2019). As expected, our modelling results demonstrate that the north-~~
 928 ~~facing slope receives less summer insolation than the south-facing slope, resulting in reduced glacial melt (5–10%)~~
 929 ~~under the same temperature conditions. Our 2D ice surface model suggests that an aspect affects the amount of~~
 930 ~~melt, however in a very small amount. This small reduction in the melt due to the shading effect could not stagnate~~
 931 ~~glaciers or cause significant glacier to advance for 3000 years. Under the same temperature, glaciers on the north~~
 932 ~~and south-facing slopes across small regions behave almost synchronously.~~

933 ~~iv. Some previous studies suggest that temperature is lower on the north-facing slopes at the same altitude. On the~~
 934 ~~north-facing slope of Taibai, Qinling mountains, JJA monthly mean temperature is measured 0.5–1 °C lower than~~
 935 ~~on the south-facing slope in the altitude range of 1250–3750 m (Tang & Fang, 2006). The vegetation distribution~~
 936 ~~on Mongolia's north-facing and south-facing slopes can prove the contrast in temperature and moisture on sunny~~
 937 ~~and shady slopes. In the field, we can easily see that trees grow only on the northern slope within the forest step~~
 938 ~~zone in Mongolia (Fig. 7d, 7e). According to these facts, a small temperature difference is real and needs to be~~
 939 ~~considered. When we set the present day temperature of Jargalant to 0.5 °C colder than in the Ih Artsan, 2D ice~~
 940 ~~surface modelling results perfectly match with the ¹⁰Be age dating results (Fig. 9). In this case, glaciers retreated~~
 941 ~~from their distal location asynchronously. The retreat of Ih Artsan glacier started near 20.23 ka (age dating result~~
 942 ~~was 20.1 ka), while Jargalant glacier started to retreat near 17.13 ka (age dating result was 17.2 ka). There were~~
 943 ~~small fluctuations in the ice advance and retreat with temperature changes in both cases, synchronous and~~
 944 ~~asynchronous.~~

945 ~~In conclusion, g~~Glacier volume and area changes are likely to be sensitive to ~~temperature~~ temperature change
 946 ~~during cold periods (22–16 ka) in semi-arid and arid regions, such as Ih Bogd~~ Ikh Bogd (Batbaatar et al., 2018).
 947 Glaciers of Ikh Artsan and Jargalant behaved asynchronously due to aspect-induced temperature differences, rather
 948 than solar insolation. In subfreezing temperature, even summer precipitation falls as snow, increasing glacier
 949 accumulation and reducing ablation. Based on the age dating and 2D ice surface modelling, we propose that the
 950 glaciers on the north and south-facing slopes of Ih Bogd were able to reach their maximum extent at different times
 951 with a 3 kyr temporal gap, caused by a combination of aspect-driven melt rate and temperature difference.

954 **6.5.4. Morphostratigraphic mismatch in exposure age dating from erratic boulders, Jargalant valley**

955 **6.5.4.1. Inheritance from the summit plateau**

956 The massif has a steep slope; in particular, the slope reaches 32–70° along cirque walls and incised valleys.
 957 Colluvial materials covering hillslopes and long boulder corridors were mainly the results of the active mass wasting
 958 process. Particularly, rockfall deposits forming scree and talus apron must be the product of steep slope failure of the
 959 summit plateau (Fig. [1011](#)). We expected that inner moraine crests would present Holocene or HS-1 exposure in light
 960 of morphostratigraphy. M_{J2}, M_{J3}, and M_{J4} moraine crests have exposure ages ranging from 636.2 to 35.9 ka (Table 2,

961 Fig. 56). According to moraine stratigraphy, exposure ages of inner moraines cannot be older than the age of the distal
 962 moraine. The apparent ages show antiquity and scatter in its distribution, which cannot be a single geologic event;
 963 associating the mean age with the specific timing of glacial termination is not appropriate (Heyman et al., 2011b). It
 964 was more likely that the exposure ages from M_{J2}, M_{J3}, and M_{J4} moraines were due to the inherited ¹⁰Be concentration
 965 produced during prior exposure in the boulders recycled from the cirque wall or paleo summit plateau by rockfall or
 966 toppling during glaciation and/or paraglacial period. During termination of the farthest moraine, glacier was long
 967 enough to pluck the fresh rocks out along its bed. Also, thick glacier would not allow inherited rocks fall onto the
 968 glacier ice (Fig. 12d). After glacier retreat to the cirque, glacier thinning allowed rockfalls with inheritance to the ice
 969 surface. Increase of inherited boulders would be contributed by enhanced rock-slope failure (de-buttressing) right after
 970 rapid deglaciation (Hashemi et al., 2022; Ballantyne and Stone, 2012; Cossart et al., 2008) and ice segregation along
 971 the bergschrund. Boulders with inheritance transported to the glacier toe as supraglacier debris. Plucking out by the
 972 shorter shortened glacier distance from the cirque wall was not enough efficient for to supply a glacier to erode
 973 the rock surface fresh rocks, relative to the rock supply with summit plateau including inheritance (Fig. 12e), during
 974 transportation to the final position (Fig. 11d-f). On the other hand, this pattern would be contributed by enhanced rock-
 975 slope failure (de-buttressing) right after rapid deglaciation (Hashemi et al., 2022; Ballantyne and Stone, 2012; Cossart
 976 et al., 2008).

977

978

979 **6.5.4.2. Cenozoic evolution of the low-lying, high-elevated summit plateau**

980 ~~We recalculated the exposure age and erosion rate for the paleo summit plateau using ¹⁰Be concentrations~~
 981 ~~from those reworked boulders and production rate at the elevation of 3625 m which is the highest point between~~
 982 ~~Jargalant and Ih Artsan cirques (Fig. 11). Maximum exposure age of the flat summit plateau was calculated as 442.3~~
 983 ~~± 29.8 ka, and the corresponding erosion rate of the summit plateau was 1.23 ± 0.10 m Myr⁻¹, which falls well into~~
 984 ~~the common denudation rate of arid region. (Table 2).~~

985 The flat summit plateau of the Ih-BogdIkh Bogd massif is considered an uplifted paleo-peneplanation surface.
 986 The basement structure of Ih-BogdIkh Bogd was formed by the collision of the WNW-ESE to ENE-WSW oriented
 987 amalgamated terranes throughout the Precambrian and Paleozoic (Şengör et al., 1993). ⁴⁰Ar/³⁹Ar ages from extrusive
 988 volcanic on the Ih-BogdIkh Bogd summit and apatite fission-track data show two significant uplifts that occurred in
 989 the Gobi-AltayAltai range and Ih-BogdIkh Bogd history (Jolivet et al., 2007; Vassallo et al., 2007). The first uplift
 990 related to early to mid-Jurassic, the region experienced crustal shortening events greater than 2 km. Gobi-AltayAltai
 991 has been observed elsewhere in central Asia through this event that is possibly due to a collision between Mongol-
 992 Okhotsk and Siberia or the Lhasa and Qiangtang block to the far south in Tibet (Cunningham, 2010; Dewey et al.,
 993 1988; Traynor and Sladen, 1995). The present erosional surface of the summit plateau formed just after this Jurassic
 994 exhumation and was preserved under a negligible erosion rate. Preservation of this flat summit plateau and its fission-
 995 track age indicate quiescence without significant vertical crustal motions continued until the last uplift began
 996 (Cunningham, 2010; Jolivet et al., 2007; Vassallo et al., 2007).

997 The Gobi-~~Altay~~Altai range is one of the northernmost far-fields affected by the Cenozoic tectonic collision
998 of India into Asia, which initiated the late Cenozoic reactivation and present-day stress regime (Cunningham et al.,
999 1996; Vassallo et al., 2007). According to the apatite fission track data of Vassallo et al. (2007), the onset of the last
1000 and ongoing uplift corresponds to the late Cenozoic, 5 ± 3 Ma. This tectonic reactivation is responsible for creating
1001 the high topography (~4000 m a.s.l) seen today, in the response to which faster exhumation is initiated as well
1002 (Vassallo et al., 2007).

1003 The paleo-erosion surfaces at high altitudes experienced rapid uplift after a long time of quiescence with low
1004 erosion. Cosmogenic nuclides-based denudation rates from global paleo-erosion surfaces in diverse climatic, tectonic,
1005 and lithologic environments do not exceed ~ 20 m Myr⁻¹ (Byun et al., 2015). We obtained erosion rate for flat summit
1006 plateau using production rate at summit plateau and ¹⁰Be concentrations of reworked boulders from M_{J4}, M_{J3}, and M_{J2}
1007 moraines. Calculated bedrock erosion rate for last ~600 ka for summit plateau ranged from 1.23 ± 0.10 m Myr⁻¹
1008 to 25.8 ± 5.75 m Myr⁻¹. The erosion rate of 25.8 ± 5.75 m Myr⁻¹ was thought to be a maximum value because erosion
1009 probably increases with the increasing elevation of the uplifting massif. This result was harmonious with the long-
1010 term (since the last uplift) exhumation rate of 23.6 ± 3 m Ma⁻¹ (Vassallo et al., 2011) and Holocene erosion rate of 28
1011 m Myr⁻¹ (Jolivet et al., 2007) for the massif. Whereas flatness and the lowest erosion rate of 1.23 ± 0.10 m Myr⁻¹
1012 reveal negligible erosion and notable preservation of paleo-surface for several hundred thousand years. If this erosion
1013 rate reflects an average rate that can be applied to the entire flat surface and has been maintained for the total uplift
1014 period of the massif (Vassallo et al., 2007), it would account for only the 2 to 7.6 m of erosion.

1015 **76. CONCLUSIONS**

1016 Central Asian valley glaciers, including Ih-BogdIkh Bogd massif, expanded and shrank, presenting more complex
 1017 behavior relative to large ice sheets in the northern hemisphere. Regional climate and local non-climatic factors have
 1018 been playing an essential role in this complexity. Our ^{10}Be dating documents that the maximum advance in Ih
 1019 ArtsanIkh Artsan valley on the southern slope occurred at 20.1 ka ($M_{\text{th}}M_{\text{LA}1}$), generally falling within the gLGM,
 1020 whereas large terminal moraine formed around 17.2 ka (M_{J1}) in the Jargalant valley on the northern slope.

1021 Asynchrony in glacier expansion has been reported from some of areas in the globe but has not been clearly
 1022 studied with a combination of geochronologic and numerical modeling approaches. ~~The glacier chronology itself~~
 1023 ~~provides the possibility of both explanations, synchronous and asynchronous expansion of glacier. Glaciers of Ih~~
 1024 ~~Artsan and Jargalant valleys advanced and retreated synchronously in the same LGM summer temperature.~~ Due to
 1025 aspect-driven solar insolation change, paleoglacier in the north-facing Jargalant valley melted slower (5-10%) than
 1026 the glacier in Ih-ArtsanIkh Artsan valley. However, this amount of melt difference could not produce glacier advance
 1027 or stagnation for a long period. Asynchronous glaciation was observed across the study area if the LGM summer
 1028 temperature in Jargalant valley ~~was considered colder than Ikh Artsan and age dating result and modelling result were~~
 1029 ~~consisting when we -was-apply 0.5 °C lower temperature to Jargalant to~~ than in Ih-ArtsanIkh Artsan. ~~due to aspect-~~
 1030 ~~driven temperature change.~~ According to the lower temperature case, Jargalant glacier retreated from the most
 1031 extensive position 3000 years later than Ih-ArtsanIkh Artsan glacier. In the other words, our modelling reveals that
 1032 ~~The-the~~ temperature difference driven by aspect on both slopes significantly affects the glaciers to survive longer than
 1033 when the aspect-driven insolation only affects the glacier melt.

1034 The glacial retreat began soon after the peak of local glacial maximum on both valleys and left several
 1035 sequences of inner moraines in their heads (cirques). Inner moraine at the south-facing cirque dated to ~ 13.5 ka
 1036 (Batbaatar et al., 2018), however on the north-facing cirque, transported boulders show a significantly old exposure
 1037 age (636.2 to 35.9 ka) for inner moraines (M_{J2} - M_{J4}). The summit plateau of the Ih-BogdIkh Bogd massif is one of the
 1038 oldest known tectonically uplifted surfaces on Earth. It is more likely that extremely old exposure ages are the result
 1039 of inheritance recycled from rock falls from the paleo-erosional surface of the summit plateau.

1040 *Data availability.* The data that supports the findings of this study are available within the article [and its
1041 supplementary material]
1042

1043 *Author contributions.* YBS planned the study and proceeded a field investigation with JSO, PK, KS, and CHL. YBS
1044 designed a funding acquisition. JSO designed ^{10}Be lab experiments with RHH and BYY. CHL and MKS developed
1045 a matlab code of the 2D ice surface modelling and performed the simulation. PK and YBS prepared the manuscript
1046 with contributions from all co-authors.

1047

1048 *Competing interests.* The contact author has declared that neither they nor their co-authors have any competing
1049 interests.

1050

1051 *Disclaimer.* Publisher's note: Copernicus Publications remains neutral with regard to jurisdictional claims in
1052 published maps and institutional affiliations.

1053

1054 *Acknowledgments.* This work was supported by the Ministry of Education of the Republic of Korea and the National
1055 Research Foundation of Korea (NRF-2018S1A5A2A01031348 for Y.B.S).

1056

1057 **REFERENCES**

- 1058 ©JAXA/METI., 2007. ALOS PALSAR L1.0 High-resolution terrain corrected dataset. Accessed through ASF DAAC,
 1059 <https://asf.alaska.edu>, 25 June 2009. <https://doi.org/10.5067/J4JVCFDDPEW1>
- 1060 An, Z., Kukla, G., Porter, S.C., Xiao, J.: Late Quaternary dust flow on the Chinese loess plateau, *Catena*, 18(2), 125-
 1061 132, [https://doi.org/10.1016/0341-8162\(91\)90012-M](https://doi.org/10.1016/0341-8162(91)90012-M), 1991.
- 1062 [Balco, G: Contributions and unrealized potential contributions of cosmogenic nuclide exposure dating to glacier](#)
 1063 [chronology, 1990–2010. *Quat. Sci. Rev.* 30, 3–27. <https://doi.org/10.1016/j.quascirev.2010.11.003>, 2011](#)
- 1064 Balco, G., Stone, J.O., Lifton, N.A., Dunai, T.J.: A complete and easily accessible means of calculating surface
 1065 exposure ages or erosion rates from ^{10}Be and ^{26}Al measurements, *Quat. Geochronol.*, 3(3), 174-195,
 1066 <https://doi.org/10.1016/j.quageo.2007.12.001>, 2008.
- 1067 Ballantyne, C.K., Stone, J.O.: Timing and periodicity of paraglacial rock-slope failures in the Scottish Highlands,
 1068 *Geomorphology*, 186, 150-161, <https://doi.org/10.1016/j.geomorph.2012.12.030>, 2013.
- 1069 Barr, I.D., Lovell, H.: A review of topographic controls on moraine distribution, *Geomorphology*, 226, 44-64,
 1070 <https://doi.org/10.1016/j.geomorph.2014.07.030>, 2014.
- 1071 [Batbaatar, J.: Quaternary Glaciation in Central Asia \(Doctoral dissertation\), 2018.](#)
- 1072 Batbaatar, J., Gillespie, A.R.: Outburst floods of the Maly Yenisei. Part II—new age constraints from Darhad basin,
 1073 *Int. Geol. Rev.*, 58(14), 1753-1779, <https://doi.org/10.1080/00206814.2016.1193452>, 2016.
- 1074 Batbaatar, J., Gillespie, A.R., Fink, D., Matmon, A., Fujioka, T.: Asynchronous glaciations in arid continental climate,
 1075 *Quat. Sci. Rev.*, 182, 1-19, <https://doi.org/10.1016/j.quascirev.2017.12.001>, 2018.
- 1076 [Barr, I. D., & Spagnolo, M.: Glacial cirques as palaeoenvironmental indicators: Their potential and limitations. *Earth-*](#)
 1077 [*Sci. Rev.* 151, 48-78. <https://doi.org/10.1016/j.earscirev.2015.10.004>, 2015](#)
- 1078 Bayasgalan, A., Jackson, J., Ritz, J.F., Carretier, S.J.T.: Field examples of strike-slip fault terminations in Mongolia
 1079 and their tectonic significance. *Tectonics*, 18(3), 394-411, <https://doi.org/10.1029/1999TC900007>, 1999.
- 1080 Benn, D. I., and Hulton, N. R.: An Excel™ spreadsheet program for reconstructing the surface profile of former
 1081 mountain glaciers and ice caps, *Comput. Geosci*, v. 36, no. 5, p. 605-610,
 1082 <https://doi.org/10.1016/j.cageo.2009.09.016>, 2010,
- 1083 Benn, D.I., Lehmkuhl, F.: Mass balance and equilibrium-line altitudes of glaciers in high-mountain environments,
 1084 *Quat. Int.*, 65(Supplement C), 15-29, [https://doi.org/10.1016/S1040-6182\(99\)00034-8](https://doi.org/10.1016/S1040-6182(99)00034-8), 2000.
- 1085 Berger, A., and Loutre, M.-F.: Insolation values for the climate of the last 10 million years, *Quat. Sci. Rev.*, v. 10, no.
 1086 4, p. 297-317, [https://doi.org/10.1016/0277-3791\(91\)90033-Q](https://doi.org/10.1016/0277-3791(91)90033-Q), 1991,
- 1087 Berkey, C.P., Morris, F.K.: The peneplanes of Mongolia, *Am. Mus. Novit.*, 136, 1-11, 1924.
- 1088 Blomdin, R., Stroeven, A.P., Harbor, J.M., Gribenski, N., Caffee, M.W., Heyman, J., Rogozhina, I., Ivanov, M.N.,
 1089 Petrakov, D.A., Walther, M.: Timing and dynamics of glaciation in the Ikh Turgen Mountains, Altai region,
 1090 High Asia, *Quat. Geochronol.*, 47, 54-71, <https://doi.org/10.1016/j.quageo.2018.05.008>, 2018.
- 1091 Blomdin, R., Stroeven, A.P., Harbor, J.M., Lifton, N.A., Heyman, J., Gribenski, N., Petrakov, D.A., Caffee, M.W.,
 1092 Ivanov, M.N., Hättestrand, C., Rogozhina, I., Usabaliyev, R.: Evaluating the timing of former glacier

- 1093 expansions in the Tian Shan: A key step towards robust spatial correlations, *Quat. Sci. Rev.*, 153, 78-96,
 1094 <https://doi.org/10.1016/j.quascirev.2016.07.029>, 2016.
- 1095 Buizert, C., Keisling, B., Box, J., He, F., Carlson, A., Sinclair, G., and DeConto, R.: Greenland-wide seasonal
 1096 temperatures during the last deglaciation, *Geophys. Res. Lett.*, v. 45, no. 4, p. 1905-1914,
 1097 <https://doi.org/10.1002/2017GL075601>, 2018.
- 1098 Byun, J., Heimsath, A.M., Seong, Y.B., Lee, S.Y.: Erosion of a high-altitude, low-relief area on the Korean Peninsula:
 1099 implications for its development processes and evolution, *Earth Surf. Process. Landf.*, 40(13), 1730-1745,
 1100 <https://doi.org/10.1002/esp.3749>, 2015.
- 1101 [Chai, L. T., Wong, C. J., James, D., Loh, H. Y., Liew, J. J. F., Wong, W. V. C., & Phua, M. H.: Vertical accuracy](#)
 1102 [comparison of multi-source Digital Elevation Model \(DEM\) with Airborne Light Detection and Ranging](#)
 1103 [\(LiDAR\). In IOP Conference Series: Earth. Environ. Sci., 1053, No. 1, p. 012025, IOP Publishing,](#)
 1104 [10.1088/1755-1315/1053/1/012025, 2022.](#)
- 1105 Chauvenet, W.: A Manual of spherical and practical astronomy-Vol. 1: Spherical astronomy; Vol. 2: Theory and use
 1106 of astronomical instruments. Method of least squares, 5th ed., revised and corr, Dover Publication, New York,
 1107 1960
- 1108 Chen, Y., Li, Y., Wang, Y., Zhang, M., Cui, Z., Yi, C., Liu, G.: Late Quaternary glacial history of the Karlik Range,
 1109 easternmost Tian Shan, derived from ¹⁰Be surface exposure and optically stimulated luminescence datings,
 1110 *Quat. Sci. Rev.*, 115, 17-27, <https://doi.org/10.1016/j.quascirev.2015.02.010>, 2015.
- 1111 Ciner, A., Sarikaya, M. A., Yildirim, C.: Misleading old age on a young landform? The dilemma of cosmogenic
 1112 inheritance in surface exposure dating: Moraines vs. rock glaciers, *Quat. Geochronol.*, 42, 76-88,
 1113 <https://doi.org/10.1016/j.quageo.2017.07.003>, 2017.
- 1114 Clark, P.U., Dyke, A.S., Shakun, J.D., Carlson, A.E., Clark, J., Wohlfarth, B., Mitrovica, J.X., Hostetler, S.W.,
 1115 McCabe, A.M.: The last glacial maximum, *Science*, 325(5941), 710-714,
 1116 <https://doi.org/10.1126/science.1172873>, 2009.
- 1117 Cossart, E., Braucher, R., Fort, M., Bourlès, D., Carcaillet, J.: Slope instability in relation to glacial debuitressing in
 1118 alpine areas (Upper Durance catchment, southeastern France): evidence from field data and ¹⁰Be cosmic ray
 1119 exposure ages, *Geomorphology*, 95(1-2), 3-26, <https://doi.org/10.1016/j.geomorph.2006.12.022>, 2008.
- 1120 Cunningham, D.: Tectonic setting and structural evolution of the Late Cenozoic ~~Gobi-Altai~~~~Gobi-Altai~~ orogen, *J. Geol.*
 1121 *Soc. London.*, 338(1), 361-387, <https://doi.org/10.1144/SP338.17>, 2010.
- 1122 Cunningham, W.D., Windley, B.F., Dorjnamjaa, D., Badamgarov, J., Saandar, M.: Late Cenozoic transpression in
 1123 southwestern Mongolia and the ~~Gobi-Altai~~~~Gobi-Altai~~-Tien Shan connection, *Earth Planet. Sci. Lett.*, 140(1-
 1124 4), 67-81, [https://doi.org/10.1016/0012-821X\(96\)00048-9](https://doi.org/10.1016/0012-821X(96)00048-9), 1996.
- 1125 [Dahl, S. O., Bakke, J., Lie, Ø., & Nesje, A.: Reconstruction of former glacier equilibrium-line altitudes based on](#)
 1126 [proglacial sites: an evaluation of approaches and selection of sites. *Quat. Sci. Rev.*, 22\(2-4\), 275-287,](#)
 1127 [\[https://doi.org/10.1016/S0277-3791\\(02\\)00135-X\]\(https://doi.org/10.1016/S0277-3791\(02\)00135-X\), 2003](#)
- 1128 Delmas, M., Calvet, M., Gunnell, Y., Braucher, R., & Bourlès, D.: Palaeogeography and ¹⁰Be exposure-age
 1129 chronology of Middle and Late Pleistocene glacier systems in the northern Pyrenees: implications for

- 1130 reconstructing regional palaeoclimates, *Palaeogeo. Palaeoclimatol. Palaeoecol.*, 305(1-4), 109-122,
 1131 <https://doi.org/10.1016/j.palaeo.2011.02.025>, 2011.
- 1132 Delmas, M., Gunnell, Y., Braucher, R., Calvet, M., & Bourlès, D.: Exposure age chronology of the last glaciation in
 1133 the eastern Pyrenees, *Quat. Res.*, 69(2), 231-241, <https://doi.org/10.1016/j.yqres.2007.11.004>, 2008.
- 1134 Devyatkin, E.: Structures and formational complexes of the Cenozoic activated stage. *Tectonics of the Mongolian*
 1135 *People's Republic*, Nauka, 41, 182-195, 1974.
- 1136 Dewey, J.F., Shackleton, R.M., Chengfa, C., Yiyin, S.: The tectonic evolution of the Tibetan Plateau, *Philos. Trans.*
 1137 *Royal Soc. A.*, 327(1594), 379-413, <https://doi.org/10.1098/rsta.1988.0135>, 1988.
- 1138 [Evans, I. S.: Local aspect asymmetry of mountain glaciation: a global survey of consistency of favoured directions for](#)
 1139 [glacier numbers and altitudes. *Geomorphology*, 73\(1-2\), <https://doi.org/10.1016/j.geomorph.2005.07.009>](#)
 1140 [166-184, 2006](#)
- 1141 [EIC.: Geologic map of Mongolia 1:1000000. Environment Information Center of National Agency for Meteorology,](#)
 1142 [Hydrology and Environmental Monitoring, Ulaanbaatar, Mongolia, 1981.](#)
- 1143 Evans, I.S., Cox, N.J.: Global variations of local asymmetry in glacier altitude: separation of north-south and east-
 1144 west components, *J. Glaciol.*, 51(174), 469-482, <https://doi.org/10.3189/172756505781829205>, 2005.
- 1145 ~~Farr, T.G., Rosen, P.A., Caro, E., Crippen, R., Duren, R., Hensley, S., Kobrick, M., Paller, M., Rodriguez, E., Roth,~~
 1146 ~~L.: The shuttle radar topography mission, *Rew. Geophys.*, 45(2) DOI:~~
 1147 ~~<https://doi.org/10.1029/2005RG000183>, 2007.~~
- 1148 Felauer, T., Schlütz, F., Murad, W., Mischke, S., Lehmkuhl, F.: Late Quaternary climate and landscape evolution in
 1149 arid Central Asia: A multiproxy study of lake archive Bayan Tohomin Nuurç, Gobi desert, southern Mongolia,
 1150 *J. Asian. Earth. Sci.*, 48, 125-135, <https://doi.org/10.1016/j.jseaes.2011.12.002>, 2012.
- 1151 [Ferreira, Z. A., & Cabral, P.: A Comparative study about vertical accuracy of four freely available digital elevation](#)
 1152 [models: a case study in the Balsas river watershed, Brazil. *ISPRS Int. J. Geo-Inf.*, 11\(2\), 106,](#)
 1153 <https://doi.org/10.3390/ijgi11020106>, 2022
- 1154 Fletcher, W.J., Goni, M.F.S., Allen, J.R., Cheddadi, R., Combourieu-Nebout, N., Huntley, B., Lawson, I., Londeix,
 1155 L., Magri, D., Margari, V.: Millennial-scale variability during the last glacial in vegetation records from
 1156 Europe, *Quat. Sci. Rev.*, 29(21-22), 2839-2864, <https://doi.org/10.1016/j.quascirev.2009.11.015>, 2010.
- 1157 Florentine, C., Harper, J., Fagre, D.: Parsing complex terrain controls on mountain glacier response to climate forcing,
 1158 *Glob. Planet. Change.*, 191, 103209, <https://doi.org/10.1016/j.gloplacha.2020.103209>, 2020.
- 1159 Garnier, B., and Ohmura, A.: A method of calculating the direct shortwave radiation income of slopes, *J. Appl.*
 1160 *Meteorol. Climatol.*, v. 7, no. 5, p. 796-800, [https://doi.org/10.1175/1520-](https://doi.org/10.1175/1520-0450(1968)007<0796:AMOCTD>2.0.CO;2)
 1161 [0450\(1968\)007<0796:AMOCTD>2.0.CO;2](https://doi.org/10.1175/1520-0450(1968)007<0796:AMOCTD>2.0.CO;2), 1968.
- 1162 Gillespie, A., Molnar, P.: Asynchronous maximum advances of mountain and continental glaciers, *Rew. Geophys.*,
 1163 33(3), 311-364, <https://doi.org/10.1029/95RG00995>, 1995.
- 1164 Gillespie, A.R., Burke, R.M., Komatsu, G., Bayasgalan, A.: Late Pleistocene glaciers in Darhad basin, northern
 1165 Mongolia, *Quat. Res.*, 69(2), 169-187, <https://doi.org/10.1016/j.yqres.2008.01.001>, 2008.

- 1166 Goldthwait, R.P.: Mountain glaciers of the Presidential Range in New Hampshire, *Arc. Alp. Res.*, 2(2), 85-102,
1167 <https://doi.org/10.1080/00040851.1970.12003566>, 1970.
- 1168 Gosse, J.C., Phillips, F.M.: Terrestrial in situ cosmogenic nuclides: theory and application, *Quat. Sci. Rev.*, 20(14),
1169 1475-1560, [https://doi.org/10.1016/S0277-3791\(00\)00171-2](https://doi.org/10.1016/S0277-3791(00)00171-2), 2001.
- 1170 [Gribenski, N., Jansson, K. N., Preusser, F., Harbor, J. M., Stroeven, A. P., Trauerstein, M., ... & Zhang, W.: Re-](#)
1171 [evaluation of MIS 3 glaciation using cosmogenic radionuclide and single grain luminescence ages, Kanas](#)
1172 [Valley, Chinese Altai. *J. Quat. Sci.*, 33\(1\), 55-67, <https://doi.org/10.1002/jqs.2998>, 2018](#)
- 1173 Hashemi, K., Sarıkaya, M.A., Görüm, T., Wilcken, K.M., Çiner, A., Žebre, M., Stepišnik, U., Yıldırım, C.: The
1174 Namaras rock avalanche: Evidence of mid-to-late Holocene paraglacial activity in the Central Taurus
1175 Mountains, SW Turkey, *Geomorphology*, 408, 108261, <https://doi.org/10.1016/j.geomorph.2022.108261>,
1176 2022.
- 1177 Heyman, J.: Paleoglaciation of the Tibetan Plateau and surrounding mountains based on exposure ages and ELA
1178 depression estimates, *Quat. Sci. Rev.*, 91, 30-41, <https://doi.org/10.1016/j.quascirev.2014.03.018>, 2014.
- 1179 Heyman, J., Stroeven, A.P., Caffee, M.W., Hättestrand, C., Harbor, J.M., Li, Y., Alexanderson, H., Zhou, L., Hubbard,
1180 A.: Palaeoglaciology of Bayan Har Shan, NE Tibetan Plateau: exposure ages reveal a missing LGM
1181 expansion, *Quat. Sci. Rev.*, 30(15-16), 1988-2001, <https://doi.org/10.1016/j.quascirev.2011.05.002>, 2011a.
- 1182 Heyman, J., Stroeven, A.P., Harbor, J.M., Caffee, M.W.: Too young or too old: evaluating cosmogenic exposure
1183 dating based on an analysis of compiled boulder exposure ages, *Earth Planet. Sci. Lett.*, 302(1-2), 71-80,
1184 <https://doi.org/10.1016/j.epsl.2010.11.040>, 2011b.
- 1185 Hock, R.: Modelling of glacier melt and discharge: ETH Zurich-, 1999, A distributed temperature-index ice-and
1186 snowmelt model including potential direct solar radiation, *J. Glaciol.*, v. 45, no. 149, p. 101-111,
1187 <https://doi.org/10.3189/S0022143000003087>, 1998,
- 1188 Hock, R.: A distributed temperature-index ice-and snowmelt model including potential direct solar radiation, *J.*
1189 *Glaciol.*, 45(149), 101-111, <https://doi.org/10.3189/S0022143000003087>, 1999.
- 1190 Hughes, P.D., Gibbard, P.L., Ehlers, J.: Timing of glaciation during the last glacial cycle: evaluating the concept of a
1191 global 'Last Glacial Maximum'(LGM). *Earth-Sci. Rev.*, 125, 171-198,
1192 <https://doi.org/10.1016/j.earscirev.2013.07.003>, 2013.
- 1193 Iqbal, M.: *An Introduction to Solar Radiation*, New York, Academic Press, 1983
- 1194 Jiménez-Sánchez, Montserrat, et al.: "A review of glacial geomorphology and chronology in northern Spain: timing
1195 and regional variability during the last glacial cycle.", *Geomorphology*, 196, 50-64,
1196 <https://doi.org/10.1016/j.geomorph.2012.06.009>, 2013.
- 1197 Jolivet, M., Ritz, J.-F., Vassallo, R., Larroque, C., Braucher, R., Todbileg, M., Chauvet, A., Sue, C., Arnaud, N., De
1198 Vicente, R.: Mongolian summits: an uplifted, flat, old but still preserved erosion surface, *Geology*, 35(10),
1199 871-874, <https://doi.org/10.1130/G23758A.1>, 2007.
- 1200 Jones, R., Small, D., Cahill, N., Bentley, M., Whitehouse, P.: iceTEA: tools for plotting and analysing cosmogenic-
1201 nuclide surface-exposure data from former ice margins, *Quat. Geochronol.*, 51, 72-86,
1202 <https://doi.org/10.1016/j.quageo.2019.01.001>, 2019.

- 1203 Jouzel, J., Stievenard, M., Johnsen, S.J., Landais, A., Masson-Delmotte, V., Sveinbjornsdottir, A., Vimeux, F., Von
 1204 Grafenstein, U., White, J.W.: The GRIP deuterium-excess record, *Quat. Sci. Rev.*, 26(1-2), 1-17,
 1205 <https://doi.org/10.1016/j.quascirev.2006.07.015>, 2007.
- 1206 Karger, D.N., Conrad, O., Böhner, J., Kawohl, T., Kreft, H., Soria-Auza, R.W., Zimmermann, N.E., Linder, H.P.,
 1207 Kessler, M.: Climatologies at high resolution for the earth's land surface areas. *Sci. Data.*, 4, 170122,
 1208 <https://doi.org/10.1038/sdata.2017.122>, 2017.
- 1209 Khandsuren, P., Seong, Y.B., Oh, J.S., Rhee, H.H., Sandag, K., Yu, B.Y.: Late Quaternary glacial history of Khentey
 1210 Mountains, Central Mongolia, *Boreas*, 48(3), 779-799, doi.org/10.1111/bor.12386, 2019.
- 1211 Kirkbride, M., Winkler, S.: Correlation of Late Quaternary moraines: impact of climate variability, glacier response,
 1212 and chronological resolution, *Quat. Sci. Rev.*, 46, 1-29, <https://doi.org/10.1016/j.quascirev.2012.04.002>,
 1213 2012.
- 1214 Klinge, M., Böhner, J., Lehmkuhl, F.: Climate Pattern, Snow-and Timberlines in the Altai Mountains, Central Asia
 1215 (Klimaverhältnisse, Schnee-und Waldgrenzen im Altai Gebirge, Zentralasien), *Erdkunde*, 296-308, 2003.
- 1216 [Klinge, M., Schneider, F., Dulamsuren, C., Arndt, K., Bayarsaikhan, U., & Sauer, D.: Interrelations between relief,](#)
 1217 [vegetation, disturbances, and permafrost in the forest-steppe of central Mongolia. *Earth Surf. Process.*](#)
 1218 [*Landf.*, 46\(9\), 1766-1782, <https://doi.org/10.1002/esp.5116>, 2021](#)
- 1219 Kohl, C.P., Nishiizumi, K.: Chemical isolation of quartz for measurement of in situ -produced cosmogenic nuclides,
 1220 *Geochim. Cosmochim. Acta*, 56(9), 3583-3587, [https://doi.org/10.1016/0016-7037\(92\)90401-4](https://doi.org/10.1016/0016-7037(92)90401-4), 1992.
- 1221 Koppes, M., Gillespie, A.R., Burke, R.M., Thompson, S.C., Stone, J.: Late quaternary glaciation in the Kyrgyz Tien
 1222 Shan. *Quat. Sci. Rev.*, 27(7-8), 846-866, <https://doi.org/10.1016/j.quascirev.2008.01.009>, 2008.
- 1223 Laabs, B. J., Licciardi, J. M., Leonard, E. M., Munroe, J. S., & Marchetti, D. W.: Updated cosmogenic chronologies
 1224 of Pleistocene mountain glaciation in the western United States and associated paleoclimate inferences, *Quat.*
 1225 *Sci. Rev.*, 242, 106427, <https://doi.org/10.1016/j.quascirev.2020.106427>, 2020.
- 1226 Laabs, B. J. C., & Munroe, J. S.: Late Pleistocene mountain glaciation in the Lake Bonneville basin, In *Developments*
 1227 *in Earth. Surf. Process.*, Vol. 20, pp. 462-503, <https://doi.org/10.1016/B978-0-444-63590-7.00017-2>, 2016
- 1228 Laabs, B. J., Refsnider, K. A., Munroe, J. S., Mickelson, D. M., Applegate, P. J., Singer, B. S., & Caffee, M. W.:
 1229 Latest Pleistocene glacial chronology of the Uinta Mountains: support for moisture-driven asynchrony of the
 1230 last deglaciation, *Quat. Sci. Rev.*, 28(13-14), 1171-1187, <https://doi.org/10.1016/j.quascirev.2008.12.012>, 2009
- 1231 Lal, D.: Cosmic ray labeling of erosion surfaces: in situ nuclide production rates and erosion models, *Earth Planet.*
 1232 *Sci. Lett.*, 104(2), 424-439, [https://doi.org/10.1016/0012-821X\(91\)90220-C](https://doi.org/10.1016/0012-821X(91)90220-C), 1991.
- 1233 Lee, M.K., Lee, Y.I., Lim, H.S., Lee, J.I., Yoon, H.I.: Late Pleistocene–Holocene records from Lake Ulaan, southern
 1234 Mongolia: implications for east Asian palaeomonsoonal climate changes, *J. Quat. Sci.*, 28(4), 370-378,
 1235 <https://doi.org/10.1002/jqs.2626>, 2013.
- 1236 Lehmkuhl, F., Grunert, J., Hülle, D., Bathkishig, O., Stauch, G.: Paleolakes in the Gobi region of southern Mongolia,
 1237 *Quat. Sci. Rev.*, 179, 1-23, <https://doi.org/10.1016/j.quascirev.2017.10.035>, 2018.

- 1238 Li, Y., Liu, G., Chen, Y., Li, Y., Harbor, J., Stroeven, A.P., Caffee, M., Zhang, M., Li, C., Cui, Z.: Timing and extent
 1239 of Quaternary glaciations in the Tianger Range, eastern Tian Shan, China, investigated using ^{10}Be surface
 1240 exposure dating, *Quat. Sci. Rev.*, 98, 7-23, <https://doi.org/10.1016/j.quascirev.2014.05.009>, 2014.
- 1241 Licciardi, J. M., Clark, P. U., Brook, E. J., Elmore, D., & Sharma, P.: Variable responses of western US glaciers during
 1242 the last deglaciation, *Geology*, 32(1), 81-84, <https://doi.org/10.1130/G19868.1>, 2004
- 1243 Licciardi, J. M., Clark, P. U., Brook, E. J., Pierce, K. L., Kurz, M. D., Elmore, D., & Sharma, P.: Cosmogenic ^3He
 1244 and ^{10}Be chronologies of the late Pinedale northern Yellowstone ice cap, Montana, USA, *Geology*, 29(12),
 1245 1095-1098, [https://doi.org/10.1130/0091-7613\(2001\)029<1095:CHABCO>2.0.CO;2](https://doi.org/10.1130/0091-7613(2001)029<1095:CHABCO>2.0.CO;2), 2001.
- 1246 Licciardi, J. M., & Pierce, K. L.: History and dynamics of the Greater Yellowstone Glacial System during the last two
 1247 glaciations, *Quat. Sci. Rev.*, 200, 1-33, <https://doi.org/10.1016/j.quascirev.2018.08.027>, 2018
- 1248 Lifton, N., Sato, T., Dunai, T.J.: Scaling in situ cosmogenic nuclide production rates using analytical approximations
 1249 to atmospheric cosmic-ray fluxes, *Earth Planet. Sci. Lett.*, 386, 149-160,
 1250 <https://doi.org/10.1016/j.epsl.2013.10.052>, 2014.
- 1251 Luckman, B. H.: The Geomorphic Activity of Snow Avalanches. *Geografiska Annaler: Series A, Phys. Geogr.*,
 1252 59(1-2), 31-48, <https://doi.org/10.1080/04353676.1977.11879945>, 1977.
- 1253 Mischke, S., Lee, M.K., Lee, Y.I.: Climate history of southern Mongolia since 17 ka: The ostracod, gastropod and
 1254 charophyte record from Lake Ulaan, *Front. Earth Sci.*, 8, 221, <https://doi.org/10.3389/feart.2020.00221>,
 1255 2020.
- 1256 ~~NAGC, N.A.f.G.a.CALAMGCM., 1969.:~~ Topographic map of Mongolia, [Geodesy and Cartography division of](#)
 1257 [Administration Agency for Land Affairs of Administration and Management, Geodesy and Cartography of](#)
 1258 [Mongolia, Ulaanbaatar, Mongolia., 1970.](#)
- 1259 ~~NAMEMNAMHEM., N.A.f.M.a.E.m., 2020.:~~ Climate data. [Mongolian Statistical Information Service Institute for](#)
 1260 [Hydrology and Aviation Meteorological Center, of National Agency for Meteorology, Hydrology and](#)
 1261 [Environmental Monitoring, -Ulaanbaatar, Mongolia., 2020.](#)
- 1262 Nishiizumi, K., Imamura, M., Caffee, M., Southon, J., Finkel, R., McAninch, J.: Absolute calibration of ^{10}Be AMS
 1263 Standards, *Nucl. Instrum. Methods Phys. Res. B.*, 258(2), 403-413,
 1264 <https://doi.org/10.1016/j.nimb.2007.01.297>, 2007.
- 1265 National Oceanic and Atmospheric Administration.: US standard atmosphere (Vol. 76)., 1976
- 1266 Oliva, M., Palacios, D., Fernández-Fernández, J. M., Rodríguez-Rodríguez, L., García-Ruiz, J. M., Andrés, N., ... &
 1267 Hughes, P. D.: Late Quaternary glacial phases in the Iberian Peninsula, *Earth-Sci. Rev.*, 192, 564-600,
 1268 <https://doi.org/10.1016/j.earscirev.2019.03.015>, 2019.
- 1269 Olson, M., & Rupper, S.: Impacts of topographic shading on direct solar radiation for valley glaciers in complex
 1270 topography, *The Cryosphere*, 13(1), 29-40, 2019.
- 1271 Palacios, D., Stokes, C. R., Phillips, F. M., Clague, J. J., Alcalá-Reygosa, J., Andrés, N., ... & Ward, D. J.: The
 1272 deglaciation of the Americas during the Last Glacial Termination, *Earth-Sci. Rev.*, 203, 103113,
 1273 <https://doi.org/10.1016/j.earscirev.2020.103113>, 2020.

- 1274 Pötsch, S.: Dynamics and paleo-climatic forcing of late Pleistocene glaciers in the Turgen and Khangai mountains
 1275 (Mongolia) reconstructed from geomorphology, ¹⁰Be surface exposure dating, and ice flow modelling. Ph.D.
 1276 thesis, Greifswald, Finsterwalde, 2017.
- 1277 Quirk, B. J., Moore, J. R., Laabs, B. J., Plummer, M. A., & Caffee, M. W.: Latest Pleistocene glacial and climate
 1278 history of the Wasatch Range, Utah, *Quat. Sci. Rev.*, 238, 106313,
 1279 <https://doi.org/10.1016/j.quascirev.2020.106313>, 2020.
- 1280 Ross, S.M.: Peirce's criterion for the elimination of suspect experimental data, *J. Eng. Technol.*, 20(2), 38-41, 2003.
- 1281 Rother, H., Lehmkuhl, F., Fink, D., Nottebaum, V.: Surface exposure dating reveals MIS-3 glacial maximum in the
 1282 Khangai Mountains of Mongolia, *Quat. Res.*, 82(2), 297-308, <https://doi.org/10.1016/j.yqres.2014.04.006>,
 1283 2014.
- 1284 ~~Roy, D.P., Wulder, M.A., Loveland, T.R., Woodecock, C., Allen, R.G., Anderson, M.C., Helder, D., Irons, J.R.,~~
 1285 ~~Johnson, D.M., Kennedy, R.: Landsat 8: Science and product vision for terrestrial global change~~
 1286 ~~research, *Remote Sens. Environ.*, 145, 154-172, 2014.~~
- 1287 Sahsamanoglou, H., Makrogiannis, T., Kallimopoulos, P.: Some aspects of the basic characteristics of the Siberian
 1288 anticyclone, *Int. J. Climatol.*, 11(8), 827-839, <https://doi.org/10.1002/joc.3370110803>, 1991.
- 1289 [Sanders, J. W., Cuffey, K. M., Moore, J. R., MacGregor, K. R., & Kavanaugh, J. L.: Periglacial weathering and](#)
 1290 [headwall erosion in cirque glacier bergschrunds. *Geology*, 40\(9\), 779-782, <https://doi:10.1130/G33330.1>,](#)
 1291 [2012](#)
- 1292 Şengör, A., Natal'in, B., Burtman, V.: Evolution of the Altaid tectonic collage and Palaeozoic crustal growth in Eurasia,
 1293 *Nature*, 364(6435), 299-307, <https://doi.org/10.1038/364299a0>, 1993.
- 1294 Seong, Y.B., Dorn, R.I., Yu, B.Y.: Evaluating the life expectancy of a desert pavement, *Earth-Sci.Rev.*, 162, 129-154,
 1295 <https://doi.org/10.1016/j.earscirev.2016.08.005>, 2016.
- 1296 Shackleton, N.: Oxygen isotope analyses and Pleistocene temperatures re-assessed, *Nature*, 215(5096), 15-17,
 1297 <https://doi.org/10.1038/215015a0>, 1967.
- 1298 Shackleton, N.J.: The 100,000-year ice-age cycle identified and found to lag temperature, carbon dioxide, and orbital
 1299 eccentricity, *Science*, 289(5486), 1897-1902, <https://doi.org/10.1126/science.289.5486.1897>, 2000.
- 1300 Skinner, L., Shackleton, N.: An Atlantic lead over Pacific deep-water change across Termination I: implications for
 1301 the application of the marine isotope stage stratigraphy, *Quat. Sci. Rev.*, 24(5-6), 571-580,
 1302 <https://doi.org/10.1016/j.quascirev.2004.11.008>, 2005.
- 1303 Smith, S.G., Wegmann, K.W., Ancuta, L.D., Gosse, J.C., Hopkins, C.E.: Paleotopography and erosion rates in the
 1304 central Hangay Dome, Mongolia: Landscape evolution since the mid-Miocene, *J. Asian. Earth. Sci.*, 125, 37-
 1305 57 DOI: <https://doi.org/10.1016/j.jseaes.2016.05.013>, 2016.
- 1306 Stone, J.O.: Air pressure and cosmogenic isotope production, *J. Geophys. Res. Solit Earth.*, 105(B10), 23753-23759,
 1307 <https://doi.org/10.1029/2000JB900181>, 2000.
- 1308 Tang, Z., & Fang, J.: Temperature variation along the northern and southern slopes of Mt. Taibai, China, *Agric. For.*
 1309 *Meteorol.*, 139(3-4), 200-207, <https://doi.org/10.1016/j.agrformet.2006.07.001>, 2006.

- 1310 Tarasov, P., Peyron, O., Guiot, J., Brewer, S., Volkova, V., Bezusko, L., Dorofeyuk, N., Kvavadze, E., Osipova, I.,
 1311 and Panova, N.: Last Glacial Maximum climate of the former Soviet Union and Mongolia reconstructed from
 1312 pollen and plant macrofossil data, *Clim. Dyn.*, v. 15, no. 3, p. 227-240,
 1313 <https://doi.org/10.1007/s003820050278>, 1999,
- 1314 Thackray, G. D.: Varied climatic and topographic influences on Late Pleistocene mountain glaciation in the western
 1315 United States, *J. Quat. Sci.*: Published for the Quaternary Research Association, 23(6-7), 671-681,
 1316 <https://doi.org/10.1002/jqs.1210>, 2008.
- 1317 Thompson, W.G., Spiegelman, M.W., Goldstein, S.L., Speed, R.C.: An open-system model for U-series age
 1318 determinations of fossil corals, *Earth Planet. Sci. Lett.*, 210(1-2), 365-381, [https://doi.org/10.1016/S0012-](https://doi.org/10.1016/S0012-821X(03)00121-3)
 1319 [821X\(03\)00121-3](https://doi.org/10.1016/S0012-821X(03)00121-3), 2003.
- 1320 ~~Tomurtogoo, O.: Geological map of Mongolia, 2014.~~
- 1321 Traynor, J., Sladen, C.: Tectonic and stratigraphic evolution of the Mongolian People's Republic and its influence on
 1322 hydrocarbon geology and potential, *Mar. Pet. Geol.*, 12(1), 35-52, [https://doi.org/10.1016/0264-](https://doi.org/10.1016/0264-8172(95)90386-X)
 1323 [8172\(95\)90386-X](https://doi.org/10.1016/0264-8172(95)90386-X), 1995.
- 1324 Vassallo, R., Jolivet, M., Ritz, J.-F., Braucher, R., Larroque, C., Sue, C., Todbileg, M., Javkhanbold, D.: Uplift age
 1325 and rates of the Gurvan Bogd system (Gobi-~~Altay~~~~Altay~~) by apatite fission track analysis, *Earth Planet. Sci.*
 1326 *Lett.*, 259(3-4), 333-346, <https://doi.org/10.1016/j.epsl.2007.04.047>, 2007.
- 1327 Vassallo, R., Ritz, J.-F., Carretier, S.: Control of geomorphic processes on ¹⁰Be concentrations in individual clasts:
 1328 Complexity of the exposure history in Gobi-~~Altay~~~~Altay~~ range (Mongolia), *Geomorphology*, 135(1-2), 35-47,
 1329 <https://doi.org/10.1016/j.geomorph.2011.07.023>, 2011.
- 1330 Wang, Y.-J., Cheng, H., Edwards, R.L., An, Z., Wu, J., Shen, C.-C., Dorale, J.A.: A high-resolution absolute-dated
 1331 late Pleistocene monsoon record from Hulu Cave, China, *Science*, 294(5550), 2345-2348,
 1332 <https://doi.org/10.1126/science.1064618>, 2001.
- 1333 Young, N. E., Briner, J. P., Leonard, E. M., Licciardi, J. M., & Lee, K.: Assessing climatic and nonclimatic forcing
 1334 of Pinedale glaciation and deglaciation in the western United States, *Geology*, 39(2), 171-174,
 1335 <https://doi.org/10.1130/G31527.1>, 2011.
- 1336 Yu, K., Lehmkuhl, F., Diekmann, B., Zeeden, C., Nottebaum, V., Stauch, G.: Geochemical imprints of coupled
 1337 paleoenvironmental and provenance change in the lacustrine sequence of Orog Nuur, Gobi Desert of
 1338 Mongolia, *J. Paleolimnol.*, 58(4), 511-532, <https://doi.org/10.1007/s10933-017-0007-7>, 2017.
- 1339 Yu, K., Lehmkuhl, F., Schlütz, F., Diekmann, B., Mischke, S., Grunert, J., Murad, W., Nottebaum, V., Stauch, G.,
 1340 Zeeden, C.: Late Quaternary environments in the Gobi Desert of Mongolia: Vegetation, hydrological, and
 1341 palaeoclimate evolution, *Palaeogeogr. Palaeoclimatol. Palaeoecol.*, 514, 77-91,
 1342 <https://doi.org/10.1016/j.palaeo.2018.10.004>, 2019.
- 1343 Zhang, S., Zhao, H., Sheng, Y., Chen, S., Li, G., & Chen, F.: Late Quaternary lake level record of Orog Nuur, southern
 1344 Mongolia, revealed by optical dating of paleo-shorelines, *Quat. Geochronol.*, 72, 101370,
 1345 <https://doi.org/10.1016/j.quageo.2022.101370>, 2022.
- 1346

1347 **LIST OF TABLES**

1348 Table 1. LGM ELA reconstruction

1349 Table 2. Result of ^{10}Be exposure age dating1350 Table 3. ~~Run-Site parameters~~ and ~~site-glacier~~ parameters used for the 2D ice surface model1351 Table 4. ~~Input-Key~~ parameters of glacial mass balance model

1352

1353 **LIST OF FIGURES**

1354 Figure 1. Study area

1355 Figure 2. The present-day climate of Mongolia

1356 Figure 3. Source code structure diagram of 2D ice surface modelling1357 Figure 4. Photo composites of the ~~Иh-ArtsanIkh Artsan~~ valley and paleoglacial evidence1358 Figure 5. ~~Figure 4.~~ Geomorphologic setting and moraine stratigraphy in Jargalant valley1359 Figure 6. ~~Figure 5.~~ ^{10}Be Exposure ages (ka) for moraine sequences1360 Figure 7. ~~Figure 6.~~ Kernel Density Plot (KDP) of estimated ^{10}Be exposure ages from distal moraine crests in Jargalant
1361 and ~~Иh-ArtsanIkh Artsan~~ valleys1362 Figure 8. ~~Figure 7.~~ Asymmetric distribution of potential clear-sky direct solar radiation, glacial melt, and vegetation
1363 on the south- and north-facing slopes. Asynchronous distribution in potential clear sky direct solar radiation, glacial
1364 melt, and vegetation

1365

1366 Figure 9. ~~Figure 8.~~ Temporal and spatial distributions of glacial and paleo-lacustrine records in the neighboring
1367 regions of ~~Иh-BogdIkh Bogd~~ massif1368 Figure 10. ~~Figure 9.~~ Asynchronous advance and retreat pattern of ~~Иh-BogdIkh Bogd~~ paleo glacier during 22-16 ka1369 Figure 11. ~~Figure 10.~~ Rockfall deposits in Jargalant valley1370 Figure 12. ~~Figure 11.~~ Inheritance from the uplifted paleo-surface of ~~Иh-BogdIkh Bogd~~

1371 **Table 1.** LGM ELA reconstruction

Sites	Top of the rock cliff (m a.s.l)	Altitude of cirque floor (m a.s.l)	Headwall altitude ^a (m a.s.l)	Toe altitude, LGM ^b (m a.s.l)	THAR ELA ^{eb} (m a.s.l)
Jargalant valley	3620	3360	3533	2997	3308
Ih ArtsanIkh Artsan valley	3560	3385	3508	3222	3388
Average					3348

1372 ^a Headwall altitude for LGM glaciers was selected at one-third of the altitude difference between the top of the rock
1373 cliff and the cirque floor (Goldthwait, 1970).

1374 ^b ~~Toe altitude was selected as the minimum altitude of the terminal moraine~~

1375 ^e-THAR of 0.58 was used for calculating LGM ELA (Batbaatar et al., 2018)

1376 ALOS PALSAR DEM with spatial resolution of 12.5 m is used to extract corresponding elevations. Altimetric error
1377 (vertical uncertainty) is ~5-7 m (Chai et al., 2022, Ferreira and Cabral, 2021).

Table 2. Result of ^{10}Be exposure age dating

Moraine group	Name	Latitude (°N, DD)	Longitude (°E, DD)	Elevation (m a.s.l)	Thickness (cm)	Shielding factor ^a	Quartz ^c (g)	Be carrier ^d (g)	$^{10}\text{Be}/^{9}\text{Be}$ c.f. (10^{-13})	^{10}Be conc. d.f. (10^5 atoms g^{-1})	Exposure age ^{f, g, h} (ka)	LSDn
M₁₀	IAM001	44.95421	100.2602	3289	2	0.7746	20.3	0.3729	6.0 ± 0.2	7.7 ± 0.3	22.1 ± 1.9	19.9 ± 1.4
	IAM002	44.95429	100.26022	3290	2.5	0.7746	17.52	0.3796	5.3 ± 0.2	8.0 ± 0.3	23.1 ± 2.0	20.7 ± 1.4
	IAM003	44.95427	100.2603	3289	3.5	0.7746	20	0.3849	6.1 ± 0.2	8.1 ± 0.3	23.7 ± 2.1	21.2 ± 1.5
	IAM004	44.95438	100.26035	3289	3.5	0.7746	14.69	0.3958	4.1 ± 0.1	7.6 ± 0.3	22.1 ± 1.9	19.9 ± 1.4
	IAM005	44.95435	100.26015	3290	3	0.7746	19.75	0.3704	5.7 ± 0.2	7.4 ± 0.2	21.4 ± 1.8	19.3 ± 1.3
	IAM006	44.95437	100.26006	3288	3.5	0.7746	19.54	0.3812	5.7 ± 0.2	7.7 ± 0.2	22.6 ± 1.9	20.3 ± 1.4
	IAM007	44.95438	100.26004	3288	4	0.7746	18.96	0.3738	5.3 ± 0.2	7.2 ± 0.2	21.2 ± 1.8	19.1 ± 1.3
M ₁₄	JAM001	44.97614	100.29007	3412	3	0.8218	16.91	0.3842	78.6 ± 0.6	124.9 ± 1.6	344.6 ± 30.1	278.9 ± 18.1
	JAM002	44.97627	100.29012	3411	4	0.8218	20	0.3993	57.0 ± 0.6	79.7 ± 1.1	214.7 ± 18.2	177.3 ± 11.3
	JAM003	44.97651	100.29021	3411	2.5	0.8218	20.03	0.3871	194.3 ± 1.2	262.9 ± 3.1	806.4 ± 79.3	636.2 ± 45.1
	JAM004	44.97654	100.28988	3409	3	0.8218	20	0.382	70.9 ± 0.6	94.8 ± 1.3	256.3 ± 21.9	208.9 ± 13.3
	JAM005	44.97665	100.29008	3409	2.5	0.8218	20.03	0.375	64.8 ± 0.5	84.9 ± 1.1	227.0 ± 19.2	186.6 ± 11.8
M ₁₃	JAM006	44.97891	100.29092	3350	3	0.8363	20.02	0.3708	12.3 ± 2.6	15.9 ± 3.4	41.5 ± 9.5	35.9 ± 8.0
	JAM007	44.97886	100.29079	3351	3	0.8363	20.03	0.3707	25.3 ± 5.0	32.8 ± 6.5	86.3 ± 18.9	74.1 ± 15.7
	JAM008	44.97894	100.29084	3350	3	0.8363	20.42	0.3932	68.9 ± 7.0	92.9 ± 9.5	255.2 ± 35.3	209.0 ± 26.1
	JAM009	44.97891	100.29095	3348	3.5	0.8363	19.97	0.3832	15.3 ± 2.7	20.5 ± 3.7	53.8 ± 10.7	45.8 ± 8.7
	JAM010	44.97897	100.29089	3348	3.5	0.8363	19.97	0.3856	40.9 ± 5.7	55.2 ± 7.7	148.7 ± 24.8	123.8 ± 19.4
M ₁₂	JAM011	44.98058	100.29328	3293	2.5	0.8598	19.91	0.3903	52.3 ± 0.5	71.7 ± 1.0	194.5 ± 16.4	162.1 ± 10.2
	JAM012	44.98083	100.29321	3289	2	0.8598	19.97	0.3785	93.6 ± 0.6	124.2 ± 1.5	349.1 ± 30.5	284.9 ± 18.4
	JAM013	44.98095	100.29263	3289	4	0.8598	20.22	0.3794	81.0 ± 4.1	106.4 ± 5.5	300.5 ± 30.6	246.6 ± 20.6
	JAM014	44.98096	100.29259	3292	3	0.8598	20.38	0.3812	61.0 ± 6.4	79.9 ± 8.4	218.9 ± 30.5	181.9 ± 23.0
	JAM015	44.98096	100.2926	3292	3	0.8598	20.04	0.3894	59.4 ± 5.2	80.8 ± 7.1	221.7 ± 27.6	184.0 ± 20.3
M ₁₁	JAM016	44.98224	100.29684	3193	3.5	0.8852	19.91	0.3872	3.0 ± 0.1	4.0 ± 0.2	10.8 ± 1.0	10.6 ± 0.8
	JAM017	44.98232	100.29693	3191	3	0.8852	20.05	0.3935	4.8 ± 0.3	6.6 ± 0.4	17.7 ± 1.7	16.3 ± 1.4
	JAM018	44.98232	100.29693	3191	2.5	0.8852	20.06	0.3864	5.8 ± 0.4	7.8 ± 0.5	20.8 ± 2.1	18.9 ± 1.7
	JAM019	44.98326	100.29745	3170	3	0.8935	20.17	0.3962	4.4 ± 0.2	6.0 ± 0.3	16.2 ± 1.6	15.1 ± 1.3
	JAM020	44.98379	100.29716	3172	3.5	0.9311	20.14	0.3865	5.8 ± 0.2	7.7 ± 0.2	19.9 ± 1.7	18.2 ± 1.2
	JAM021	44.98385	100.29712	3171	3	0.9311	20.04	0.3879	5.4 ± 0.2	7.3 ± 0.2	18.9 ± 1.6	17.4 ± 1.2

- ^a Sampling thickness of the boulders' outermost exposed surfaces.
- ^b Topographic shielding factors for each sampling site were measured at intervals of 30°.
- ^c Weight of the pure quartz. The density of granite (2.7 g cm^{-3}) was used to calculate exposure age.
- ^d A mean value of process blank samples ($4.53 \times 10^{-15} \pm 1.62 \times 10^{-15}$) was used for correction.
- ^e Ratios of $^{10}\text{Be}/^9\text{Be}$ were normalized with 07KNSTD reference sample 5-1 prepared by Nishiizumi et al. (2007) with a $^{10}\text{Be}/^9\text{Be}$ ratio of $2.71 \times 10^{-11} \pm 4.71 \times 10^{-13}$ (calibrated error) and using a ^{10}Be half-life of 1.36×10^6 years (Chmeleff et al., 2010; Korschinek et al., 2010)
- ^f Uncertainties were calculated at the 1σ confidence level.
- ^g Exposure ages, assuming zero erosion were calculated using CRONUS-Earth online calculator version 3.0.2 (Balco et al., 2008).
- ^h Constant production rate of the ^{10}Be model of Stone (2000) was used for calculating exposure age.
- ⁱ Constant production rate of the ^{10}Be model of Lifton et al. (2014) was used.
- ^j SP001 and SP002 (SP is abbreviation of summit plateau) are not real samples. Exposure ages for summit plateau were calculated using the highest and lowest ^{10}Be concentration of boulders from inner moraines from Jargalant and production rate of summit plateau (3625 m a.s.l)

2 **Table 3.** ~~Run and s~~Site parameters and glacier parameters used for the 2D ice surface model

Variable	Value	Unit
Time interval	22-16	ka
Day type	1 (calendar day)	
Day interval	152-243 (summer)	
Average elevation of site	3265.3	m
Modern summer temperature of Ih Artsan <u>Ikh Artsan</u>	5.4	°C
Modern summer temperature of Jargalant	4.9	°C
LGM anomaly	-5.5	°C
Snow ratio (when temperature is below 0°C)	0.35	
Elevation of initial glacier's toe (Ih Artsan <u>Ikh Artsan</u>)	3385.1	m
Elevation of initial glacier's toe (Jargalant)	3360.9	m
Elevation of the distal moraine (Ih Artsan <u>Ikh Artsan</u>)	3222.2	m
Elevation of the distal moraine (Jargalant)	2997.2	m
Headwall altitude (Ih Artsan <u>Ikh Artsan</u>)	3508.3	m
Headwall altitude (Jargalant)	3533.3	m
Glacial bed shear stress (Ih Artsan <u>Ikh Artsan</u>)	100	kPa
Glacial bed shear stress (Jargalant)	200	kPa

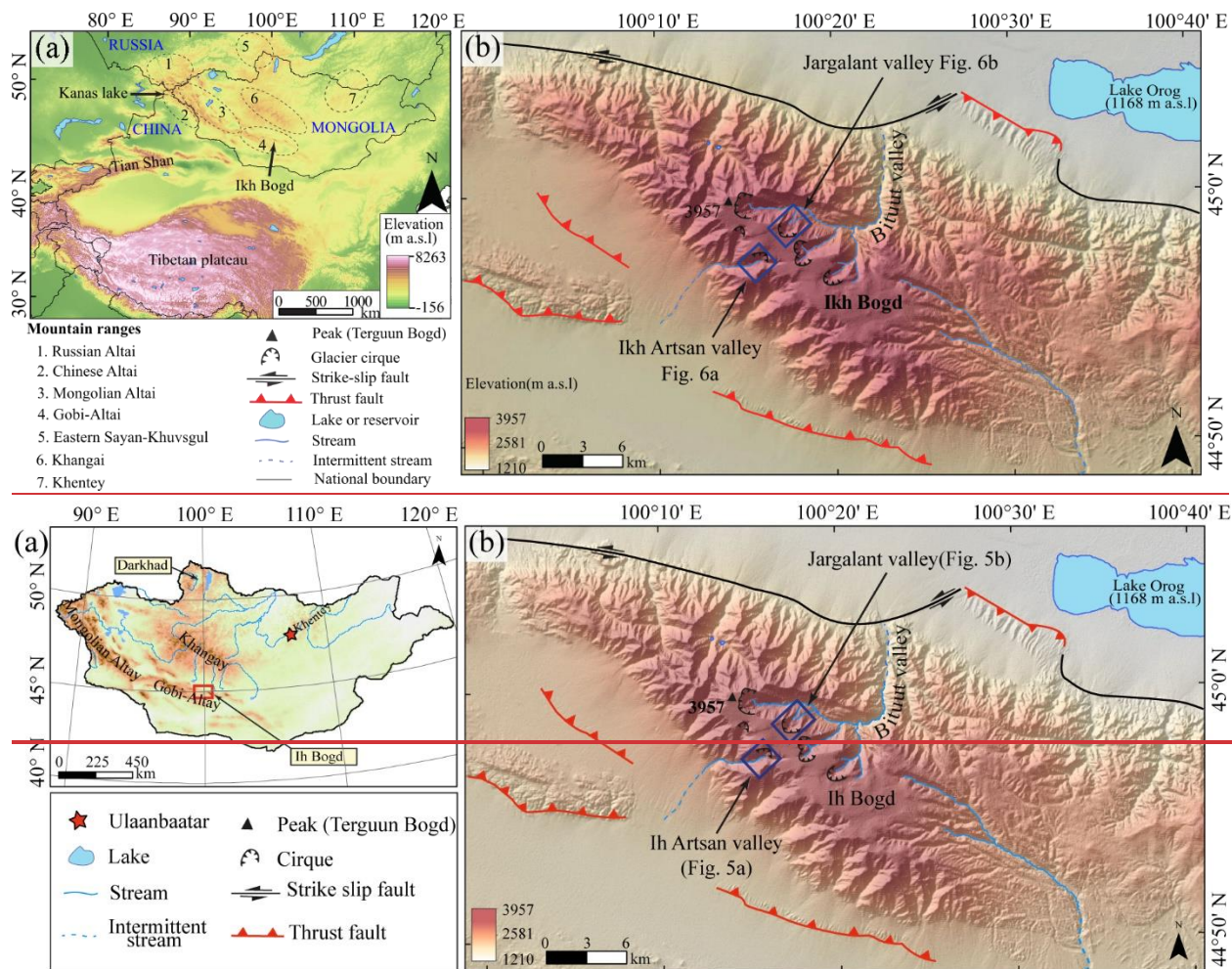
3

4

5 **Table 4.** Input Key parameters of glacial mass balance model

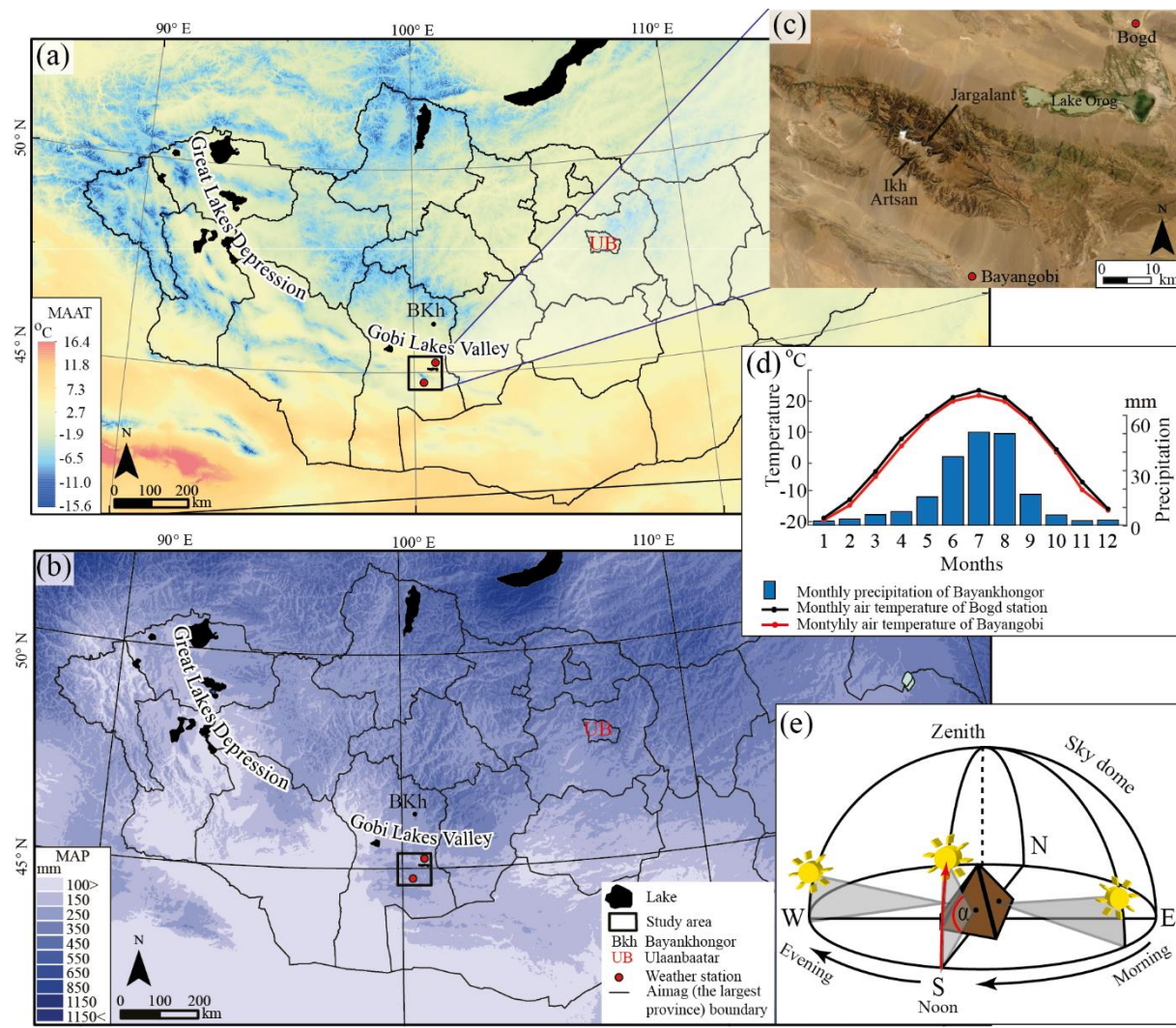
Variable	Optimized values/Unit	Variable	Optimized values/Unit
Mass balance calculation (m, mm)		Air pressure calculation (P_h, Pa)	
c	Accumulation <u>Mmm, m</u>	P_0	Pressure at reference point (sea level) 1013.25 Pa
a	Ablation/melt <u>Mmm, m</u>	T_h	Air temperature at the height h Pa
Melt calculation (a, mmm)		T_0	Air temperature at the reference point 288.15 K
n	Number of time steps per day	M	Mass per air molecule 0.0290 kg mol ⁻¹
MF	Melt factor 1.8 mm d ⁻¹ °C ⁻¹	g	Acceleration due to gravity 9.8067 m s ⁻²
a_{ice}	Radiation coefficient for ice surfaces 0.0008	R	Universal gas constant 8.3143 mol K
I	Potential clear-sky direct solar radiation at the glacier W m ⁻²	L	Atmospheric lapse rate -0.008 K m ⁻¹
T	Monthly air temperature °C	Zenith angle calculation (Z, °) and angle of incidence (θ, °)	
Insolation calculation (I, w m⁻²)		δ	Solar declination angle °/Radian
I_0	Solar constant 1367 W m ⁻²	φ	Latitude °/Radian
R_m/R	Eccentricity correction factor of the earth's orbit	ω	Hour angle °/Radian
Ψ_a	Atmospheric transmissivity 0.75	β	Slope inclination angle °/Radian
P_h	Air pressure at the height Pa	γ	Surface azimuth angle °/Radian
P_0	Air pressure at reference point (sea level) 1013.25 Pa		
Z	Zenith angle °		
θ	Angle of incidence °		

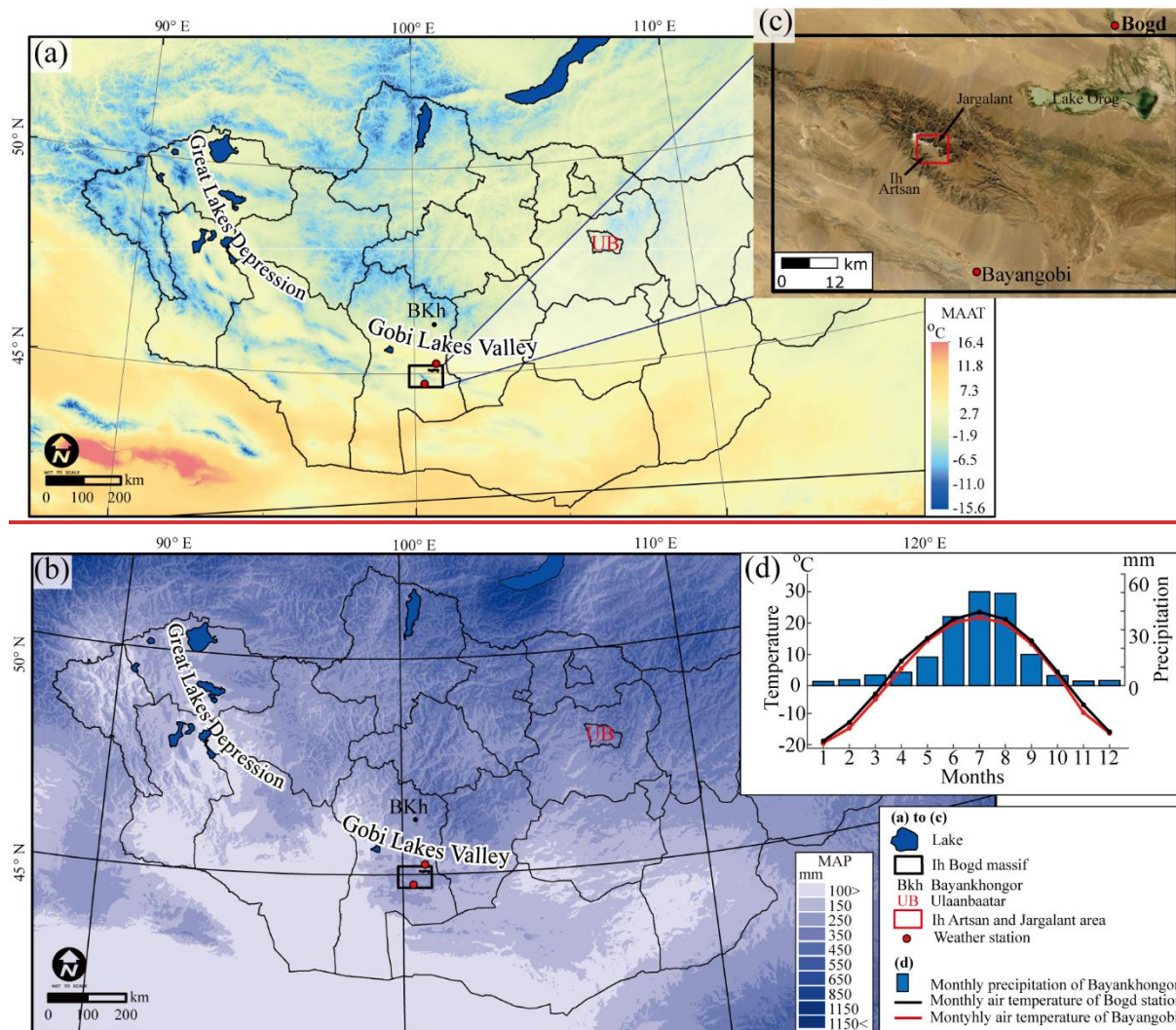
6



9 **Fig. 1.** Study area. (a) Location of the study area on the map of Mongolia. Ikh Bogd massif is described as a red
 10 box Central Asian glaciated mountain ranges during late Quaternary. (b) Detailed map of the sStudy area. Boxed areas
 11 show indicate Ikh ArtsanIkh Artsan and Jargalant valleys which were glaciated during late Quaternary. See Detailed
 12 the detailed maps of both valleys were are visualized in Figs. 34-56. The background image is shaded SRTM DEM
 13 with 30 m resolution.

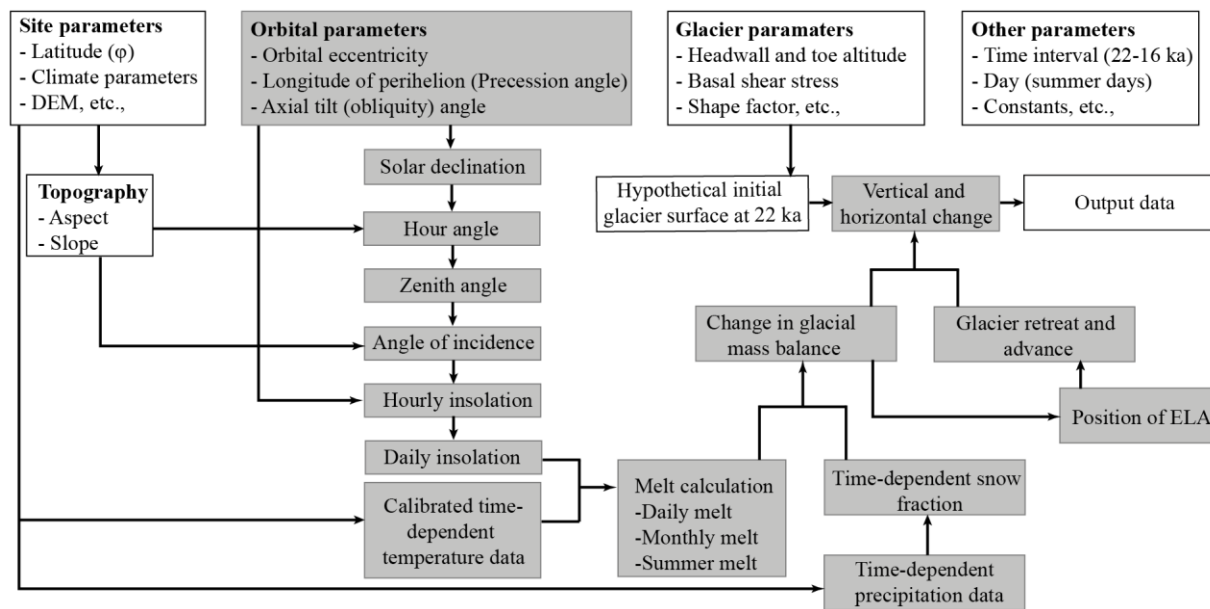
14





16

17 **Fig. 2.** The present-day climate of Mongolia. (a) Mean annual air temperature across Mongolia. (b) Mongolian mean
 18 annual precipitation. BKh (black dot) represents Bayankhongor aimag (the largest unit of province), and UB is Ulaanbaatar, the capital of Mongolia. Red dots mark the nearest weather
 19 unit of the Mongolian province), and UB is Ulaanbaatar, the capital of Mongolia. Red dots mark the nearest weather
 20 stations to the study area. Temperature data (CHELSA_Bio10_01, at 30 arc-second) and precipitation data
 21 (CHELSA_Bio10_12, at 30 arc-second) are long-term (1973-2013) annual means. Source: Bioclim Bio1 data,
 22 CHELSA V 1.2 (Karger et al., 2017). (c) The exact locations of the nearest weather stations to the massif, Bayangobi
 23 (1540 m a.s.l) and Bogd (1240 m a.s.l). (d) Long-term (1989-2019) monthly mean temperature from Bogd station
 24 (black line graph) and Bayangobi station (red line graph). Monthly mean precipitation (2005-2019) of Bayankhongor
 25 is described as blue bar chart (NAMEMNAMHEM, 2020). (e) Solar altitude angles on the mountain slopes with
 26 different aspect. Solar altitude angles (α) at different hour angles (morning to evening). Solar altitude angle is 0 degree
 27 at sunrise and reaches its maximum value at noon. In the mountainous area of northern hemisphere, south-facing slope
 28 receives highest energy at noon, however, north-facing slope receives less or no energy due to topographic shading
 29 effect.



30

31

Fig. 3. Source code structure diagram of 2D ice surface modelling



32

33

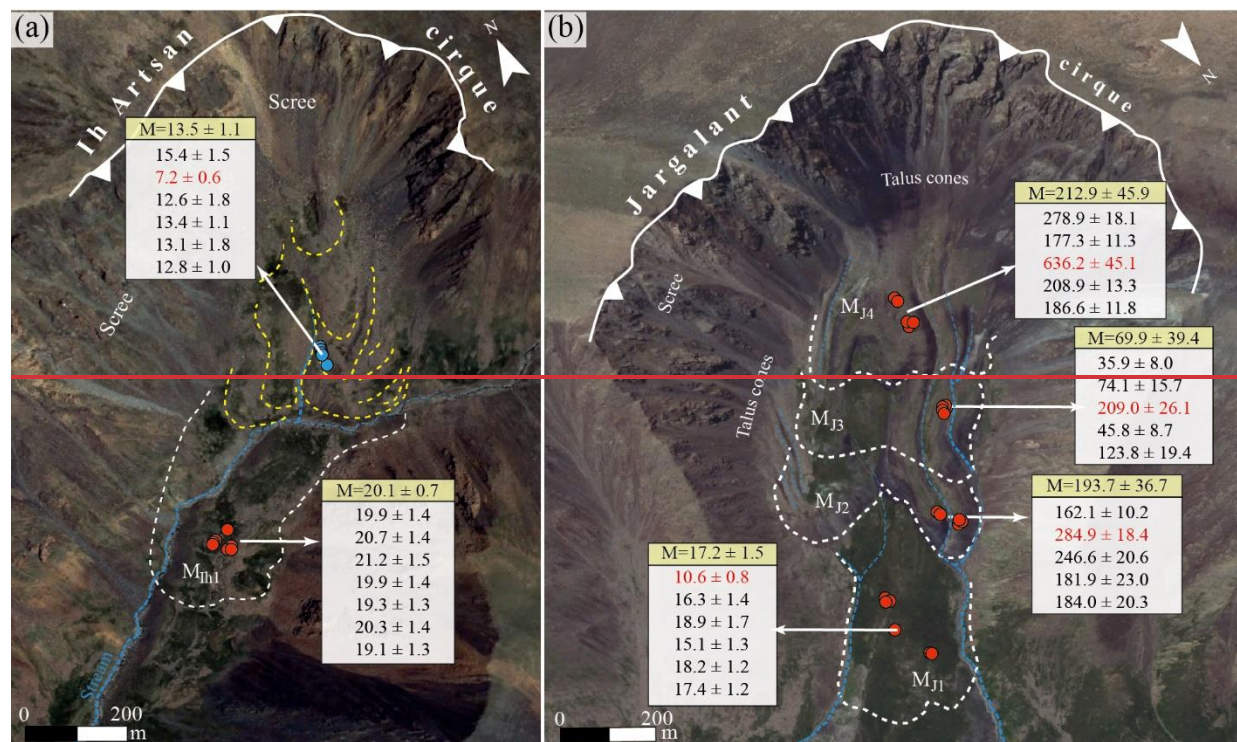
34 **Fig. 34.** Photo composites of the ~~Ih Artsan~~Ikh Artsan valley and paleoglacial evidence. (a) ~~Ih Artsan~~Ikh Artsan glacial
 35 cirque and distal moraine ridge. The white dashed arrow represents M_{Ih} / M_{Ikh} moraine ridge, which marks the farthest
 36 extent of late Quaternary glaciation. (b) Distal and inner moraine sequences (Batbaatar et al., 2018). (c) IAM006 and
 37 IAM007 sampling boulders are on the M_{Ih} / M_{Ikh} moraine ridge.



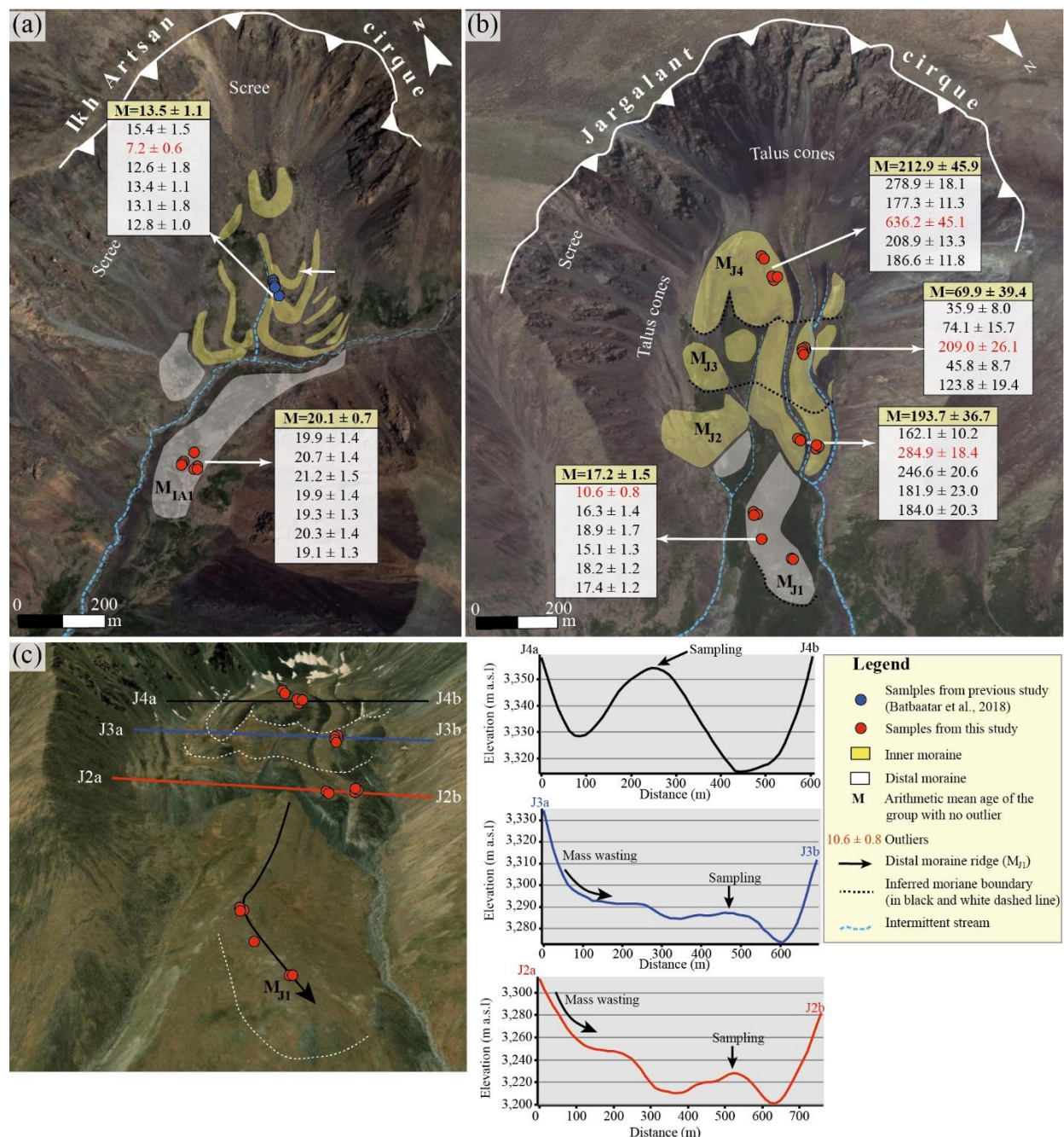


39

40 **Fig. 45.** Geomorphologic setting and moraine stratigraphy in Jargalant valley. (a) Jargalant valley and Bituut trunk
 41 valley that rises-extends from the cirque near the highest peak (3957 m a.s.l). Jargalant valley is one of the large
 42 tributary-tributaries valleys of Bituut valley, while covered by a large amount of last-late Quaternary moraine complex.
 43 (b) The stratigraphic boundary between M_{J4} and M_{J3} moraines in the Jargalant cirque. Moraines are dissected by
 44 longitudinal gullies. (c) Pair of M_{J2} moraine and oldest M_{J1} moraine ridge. Horses (red circle) are for scale. (d) Boulder
 45 sizes on M_{J2} moraine range from sub-meter to several meters. (e) Downvalley view of the moraine sequences from
 46 the uppermost moraine sequence.



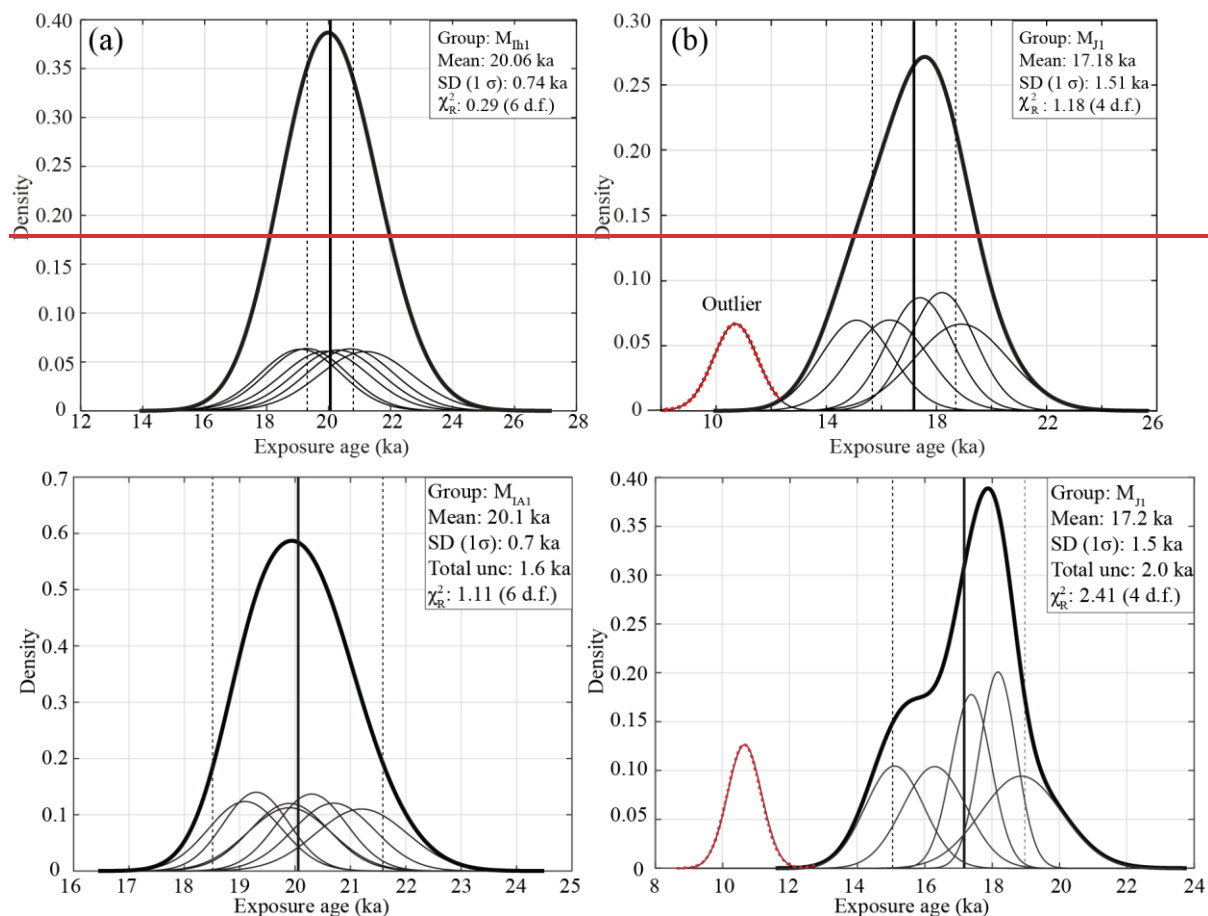
47



48

49 **Fig. 56.** ¹⁰Be Exposure ages (ka) for outer (white) and inner (yellow) moraine sequences. (a) Exposure ages from Ikh Artsan Ikh Artsan glacial cirque moraine sequences. Individual moraine sequences are marked by dashed white lines. 50 Moraine ridges in yellow dashed lines indicate inner moraine sequences recognized in the previous study by Batbaatar et al. (2018). Blue dashed lines show intermittent stream channels. Red circles are the locations of boulder samples in 51 this study, whereas blue circles indicate the sampling location from Batbaatar et al. (2018). (b) Age dating result of Jargalant hummocky cirque moraine complex, M_{J4} ~ M_{J1}. Background images of (a) and (b) are © Bing Maps (2023) 52 aerial imageries. (c) Cross-section view of inner moraine sequences (M_{J4} ~ M_{J2}) of Jargalant valley. Background image 53 is oblique imagery of © ArcGIS Earth (2023) V1.16.0.3547. Mass wasting deposits on the moraine surface and 54 intermittent stream incision have altered the original moraine morphologies. Samples were taken from the highest 55 intact point of the longitudinally elongated moraine ridge, which thought to be unaffected by reworking processes. 56 Since the exposure age dating result from inferred inner moraine sequences (M_{J4} ~ M_{J2}) shows high inheritance, which 57 cannot contribute the inferred moraine sequences. 58 59 60

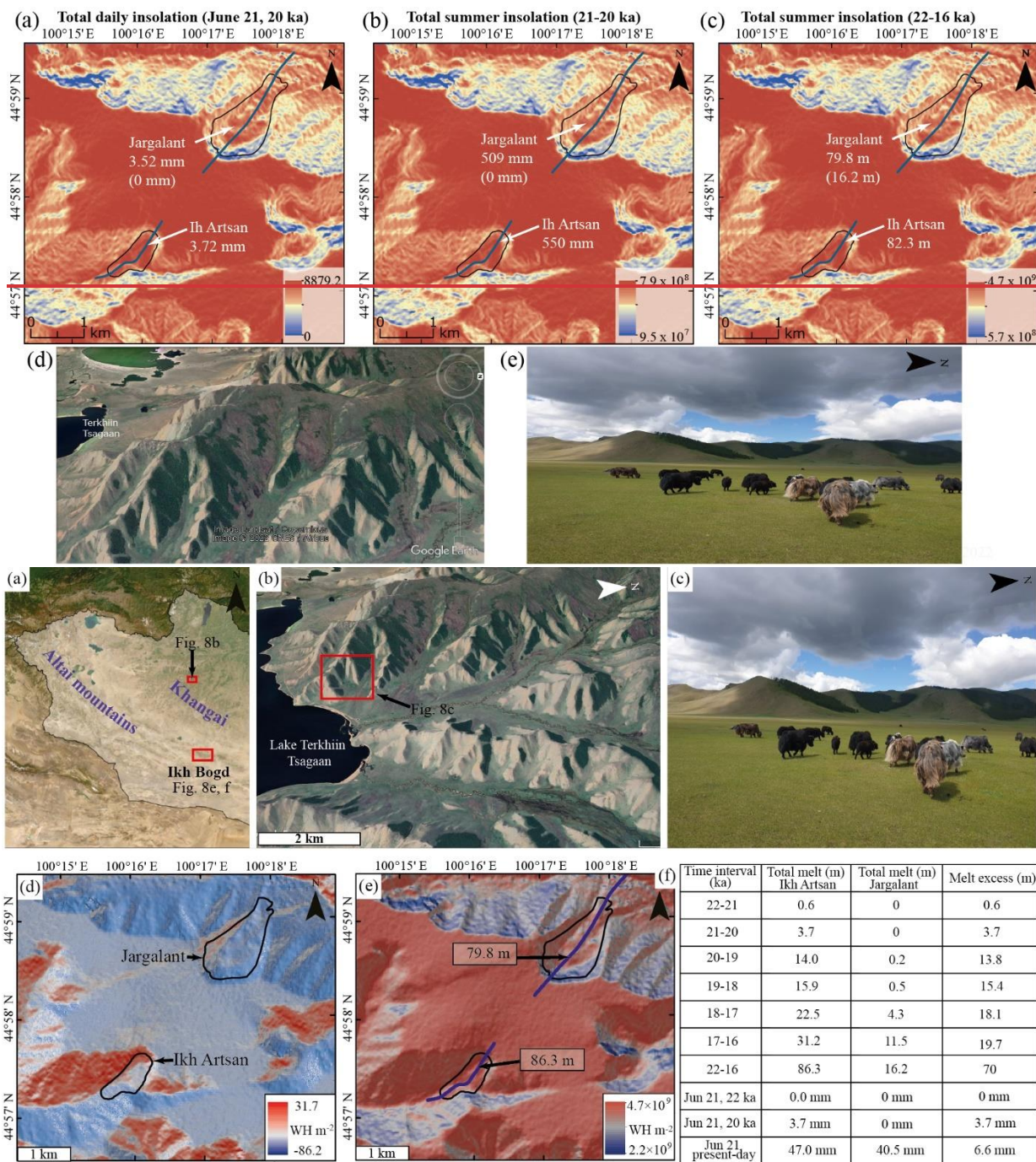
61 ~~Exposure ages in red are outliers out of one sigma. Outlier excluded mean age (M) of each moraine sequence is written~~
62 ~~on the top (yellow background). Individual moraine sequences are marked by dashed white lines. Moraine ridges in~~
63 ~~yellow dashed lines indicate inner moraine sequences recognized in the previous study by Batbaatar et al. (2018). Blue~~
64 ~~dashed lines show intermittent stream channels. Red circles are the locations of boulder samples in this study, whereas~~
65 ~~blue circles indicate the sampling location from Batbaatar et al. (2018).~~



66

67

68 **Fig. 67.** Kernel density plot (KDP) of estimated ^{10}Be exposure ages from distal moraine crests in Jargalant and ~~Artsanikh Artsan~~
69 ~~Artsanikh Artsan~~ valleys. Plots were created using IceTEA Matlab code by Jones et al. (2019). (a) KDP of exposure
70 ages of the most extensive moraine sequence ($M_{Ih}M_{IA1}$) in ~~Artsanikh Artsan~~ valley. No outlier was detected. The
71 arithmetic mean was calculated and marked as a bold solid vertical line. (b) KDP of exposure ages from the oldest
72 (M_{J1}) moraine sequence in Jargalant valley. The outlier was excluded by Chauvenet, Pierce, and the standardized
73 deviation method in the 1 sigma range. The thick solid lines represent the cumulative density curve, the dashed red
74 line shows excluded outlier, and solid, narrow black lines show individual density curves for each sample. ~~1-sigma~~
75 ~~range~~The range of total uncertainty of the group is marked as two vertical dashed lines. The sample statistics were
76 calculated after rejecting outliers, while ~~external-internal~~ errors were used to create KDP and calculate sample statistics.



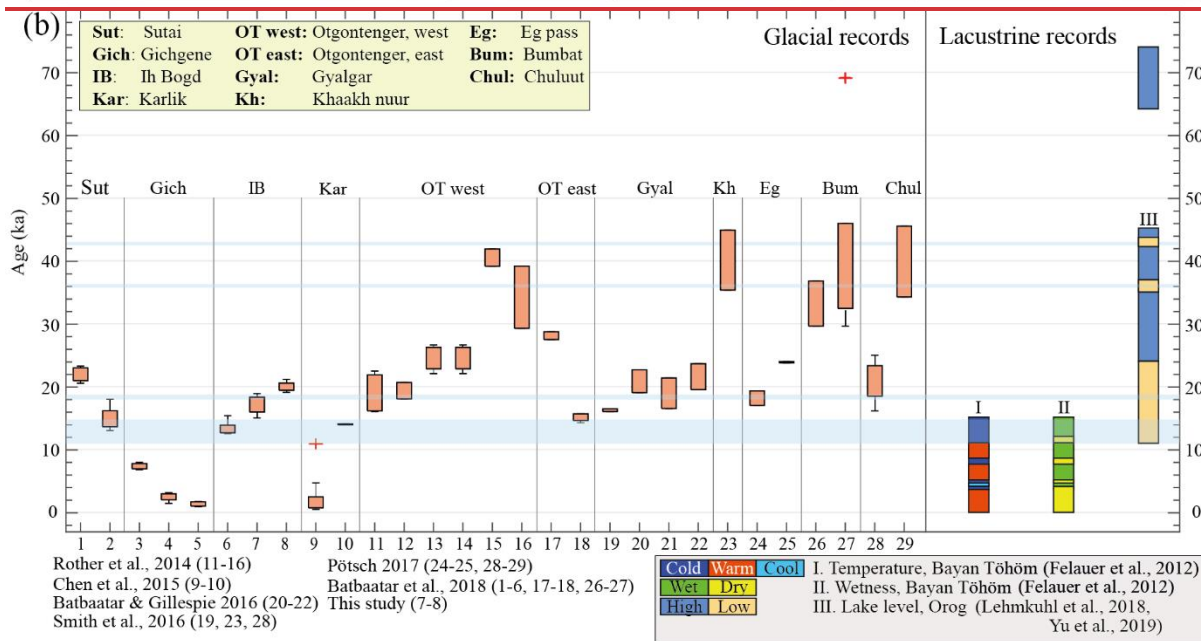
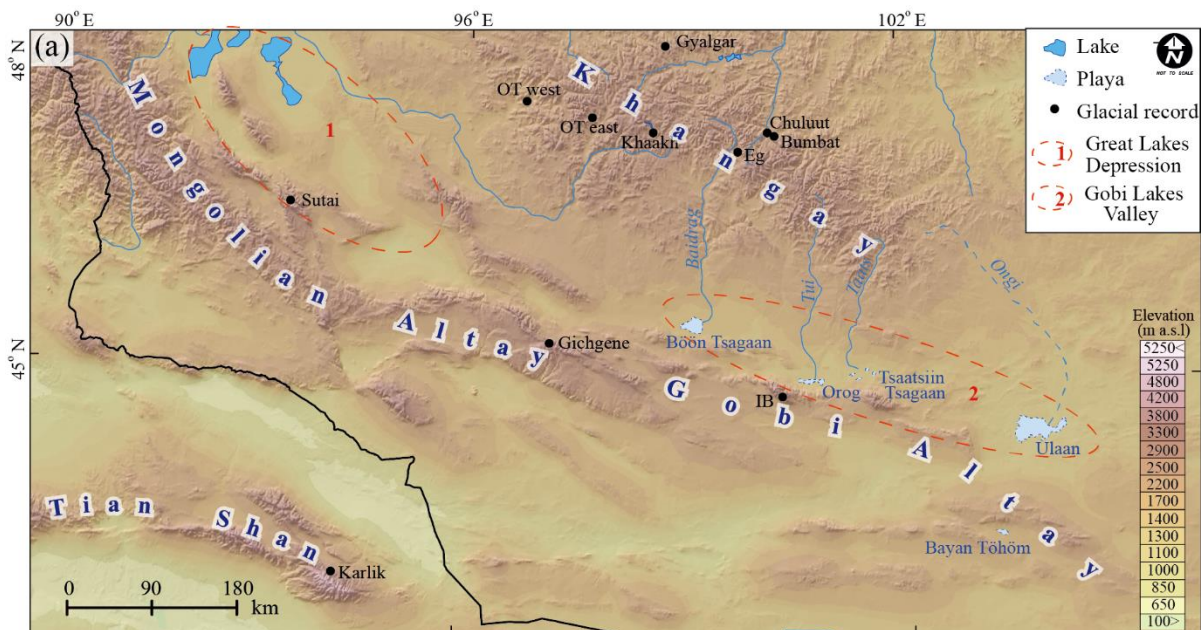
77

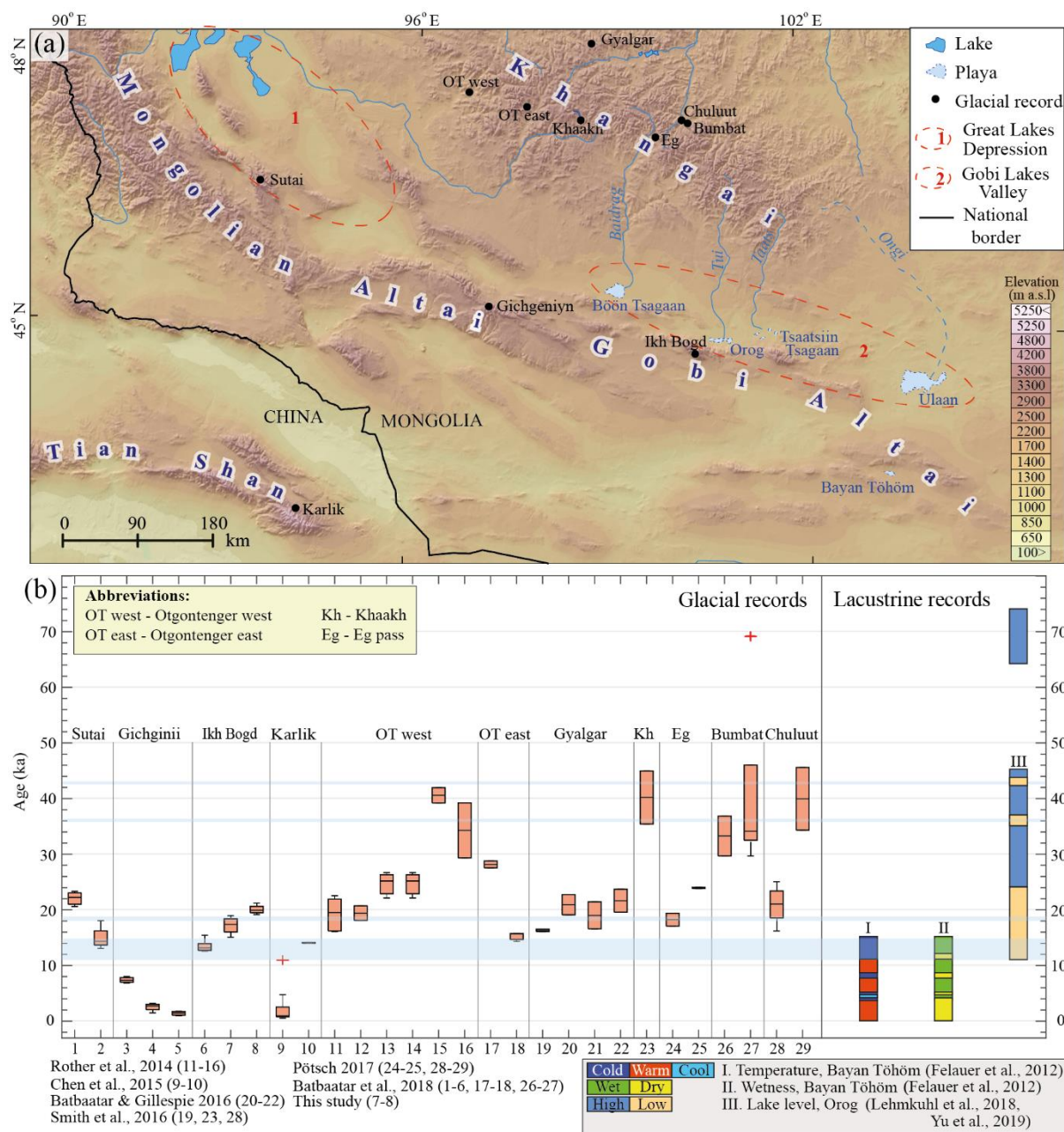
78

79 **Fig. 78. Asynchronous-Asymmetric** distribution **in-of** potential clear-sky direct solar radiation (WH m^{-2}), glacial melt,
 80 and vegetation **on the south- and north-facing slopes**. (a) **Daily insolation in the summer solstice, 20 ka** **Location map**
 81 **of Ikh Bogd and lake Terkhiiin Tsagaan**. (b, c) **Tree distribution on north-facing slope, north of lake Terkhiiin Tsagaan**
 82 **(© Google Earth 2022; photo taken by authors)**. (d) **Anomaly of Total-total** clear-sky direct solar radiation **during 21-**
 83 **20 ka** of June solstice in 20 ka from modern value. (e) **Integrated Total-total** summer insolation for 22-16 ka. **Raster**
 84 **map shows integrated total daily insolation and summer insolation**. The **blue-purple** line represents profile along
 85 **midline in Ikh Artsan** **Ikh Artsan** and Jargalant valley. **Average melt along this profile is written in white text in mm and**
 86 **m** **Integrated total melt was calculated in Ikh Artsan as 86.3 m and 79.8 m in Ikh Artsan valley for 22-26 ka at the same**
 87 **temperature.** (See supplementary file 2). (f) **Integrated total melt calculation for Ikh Artsan and Jargalant valley**

88 ~~considering average summer temperature in Jargalant is 0.5 lower than that in Ikh Artsan. Melt when the present day~~
89 ~~temperature in Jargalant is considered 0.5 °C (LGM anomaly is the same, -5.5 °C) colder than Ih Artsan is written in~~
90 ~~parenthesis. (d, e) Tree distribution pattern in northern and southern slope. Both of © Google Earth (2022) imagery~~
91 ~~(d) and photo (e) present mountain to the north of lake Terkhiin Tsagaan, Khangay mountains.~~

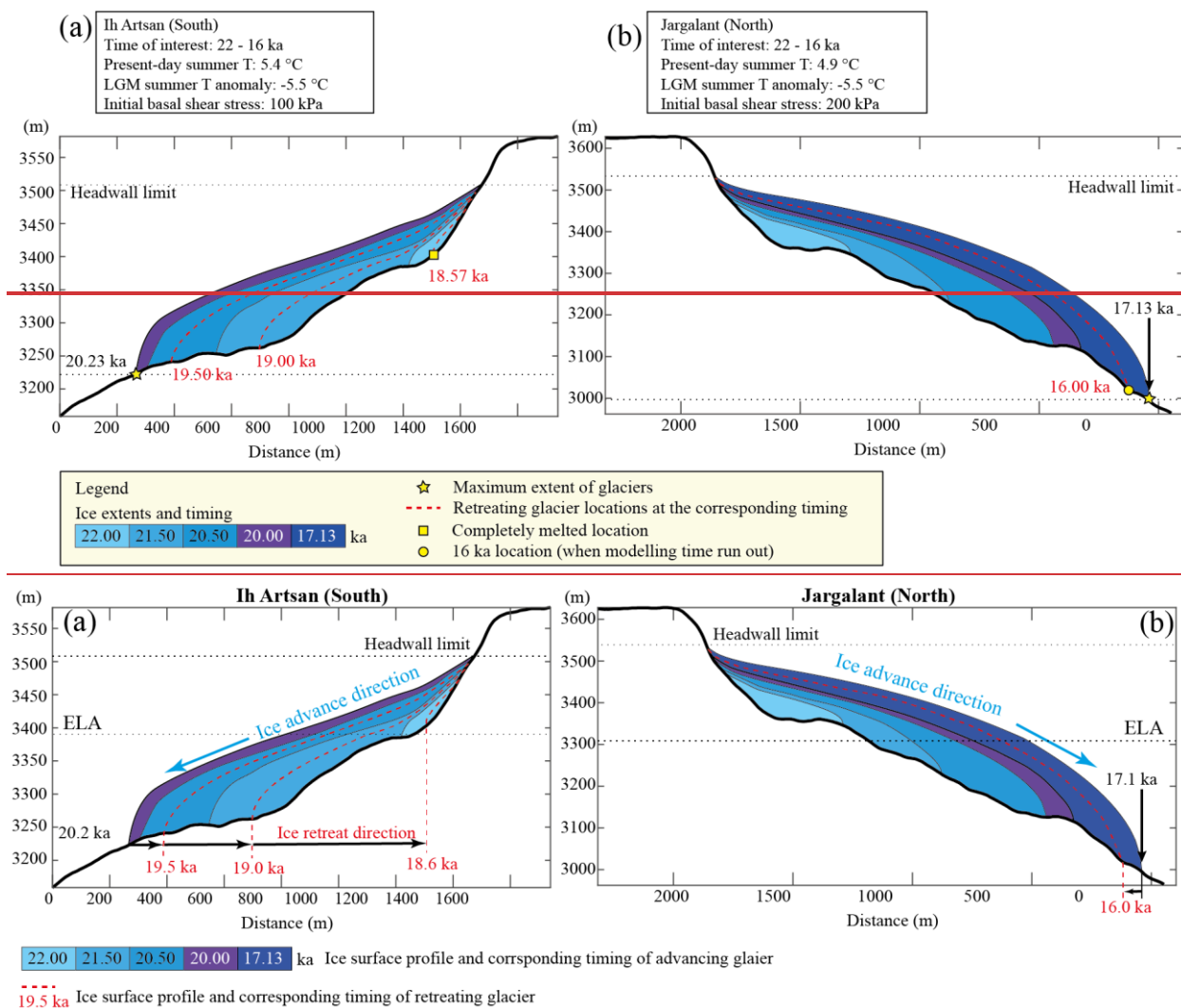
92





94

95 **Fig. 89.** Temporal and spatial distributions of glacial and paleo-lacustrine records in the neighboring regions of **H**
 96 **Bogd**/**Ikh Bogd** massif. (a) Locations of the ^{10}Be age dating sites for paleo-glaciers and paleo lacustrine proxies. (b)
 97 Age dating results from glaciers and lacustrine proxies. Glacial records on the left are the ^{10}Be exposure age dating
 98 results representing 29 individual moraine groups. Exposure ages were recalculated with Cronus Earth V3, using the
 99 LSDn scaling factor (Lifton et al., 2014). Only effective ages were plotted after outlier rejection using the [Chauvenet,](#)
 100 [Peirce,](#) and normalized deviation method ([Batbaatar et al., 2018](#)). On each box, central mark indicates the median, and
 101 the bottom and top edges of the box indicate the 25th and 75th percentiles, respectively. The whiskers extend **only to**
 102 **the most extreme data points not considered outliers,** and the additional outliers were detected from the effective
 103 ages and plotted individually using the '+' marker symbol. The shaded light blue sections on the age interval present
 104 the major harsh periods (playa phase of Orog, Yu et al., 2019). Lacustrine records on the right present temperature (I)
 105 and wetness data (II) in lake Bayan Tökhöm and lake level record of lake Orog (III).



106

107

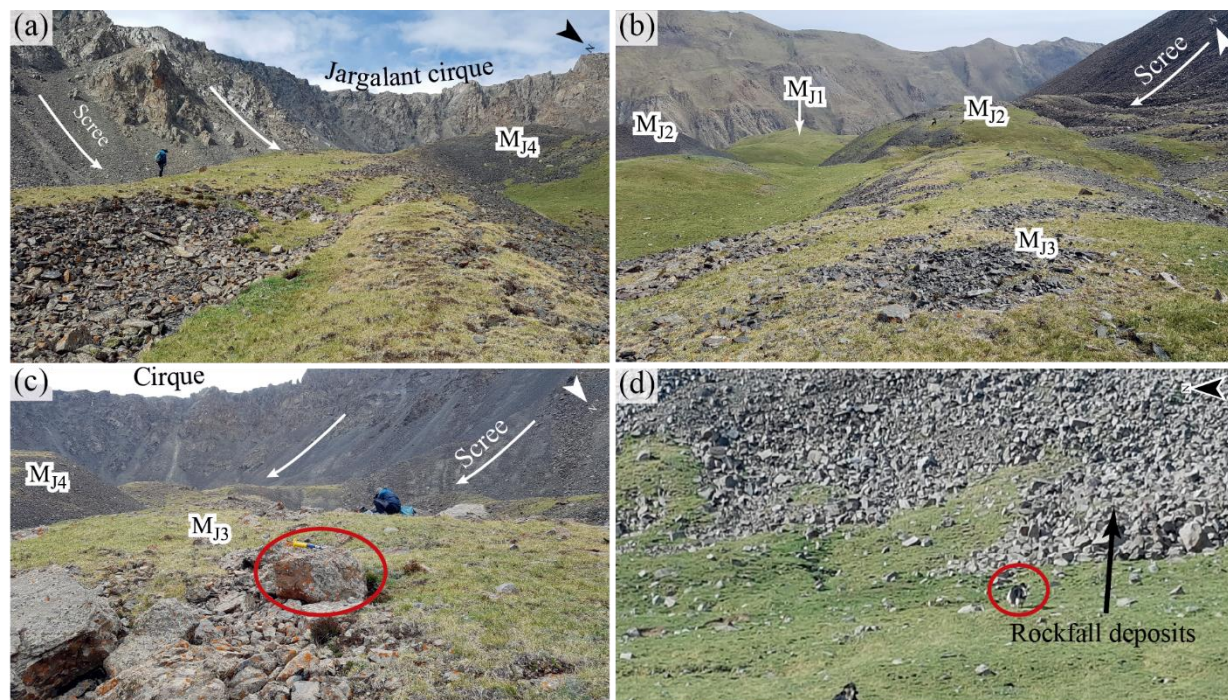
108 **Fig. 910.** Asynchronous advance and retreat pattern of Ikh Bogd paleo glacier during 22-16 ka. (a) Paleo-
 109 glacier in Ikh Artsan valley maximally advanced in 20.23 ka advanced between 22.0 and 20.2 ka and retreated
 110 from 20.2 to 18.6 ka. (b) Paleo-glacier in Jargalant valley most expanded downvalley between in 22.0 and 17.13 ka.
 111 Small retreat is observed during 17.1-16.0 ka. The present-day summer paleotemperature in the north-facing valley
 112 was considered 0.5 °C lower than in the south-facing valley. The present-day temperature is calibrated to Greenland
 113 (NGRIP) paleotemperature data (Buizert et al., 2018) using an LGM summer temperature anomaly of -5.5 °C.
 114 Headwall altitudes of the LGM paleo glaciers were used to mark the maximum thickness of the glacier.

115

116

117

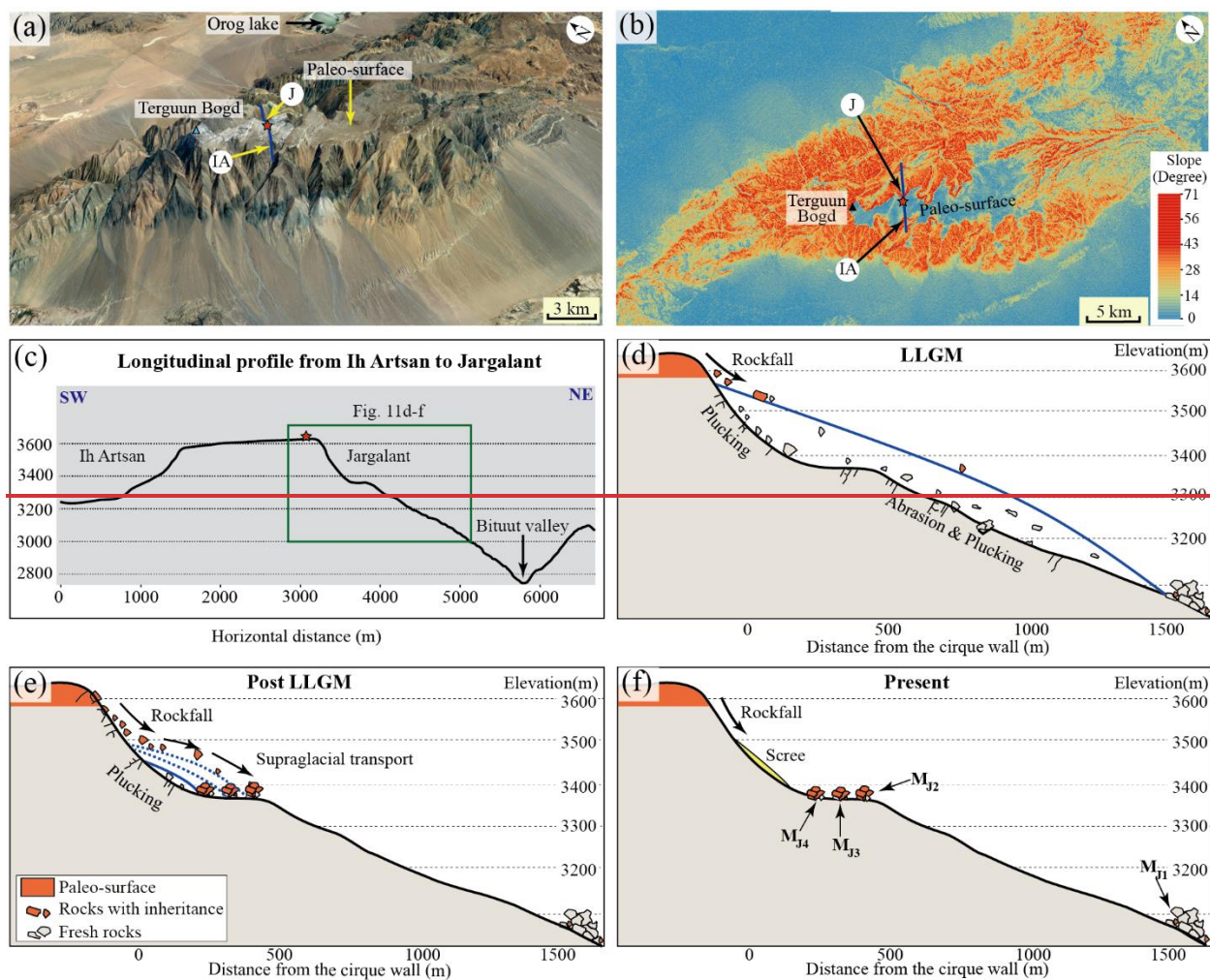
118

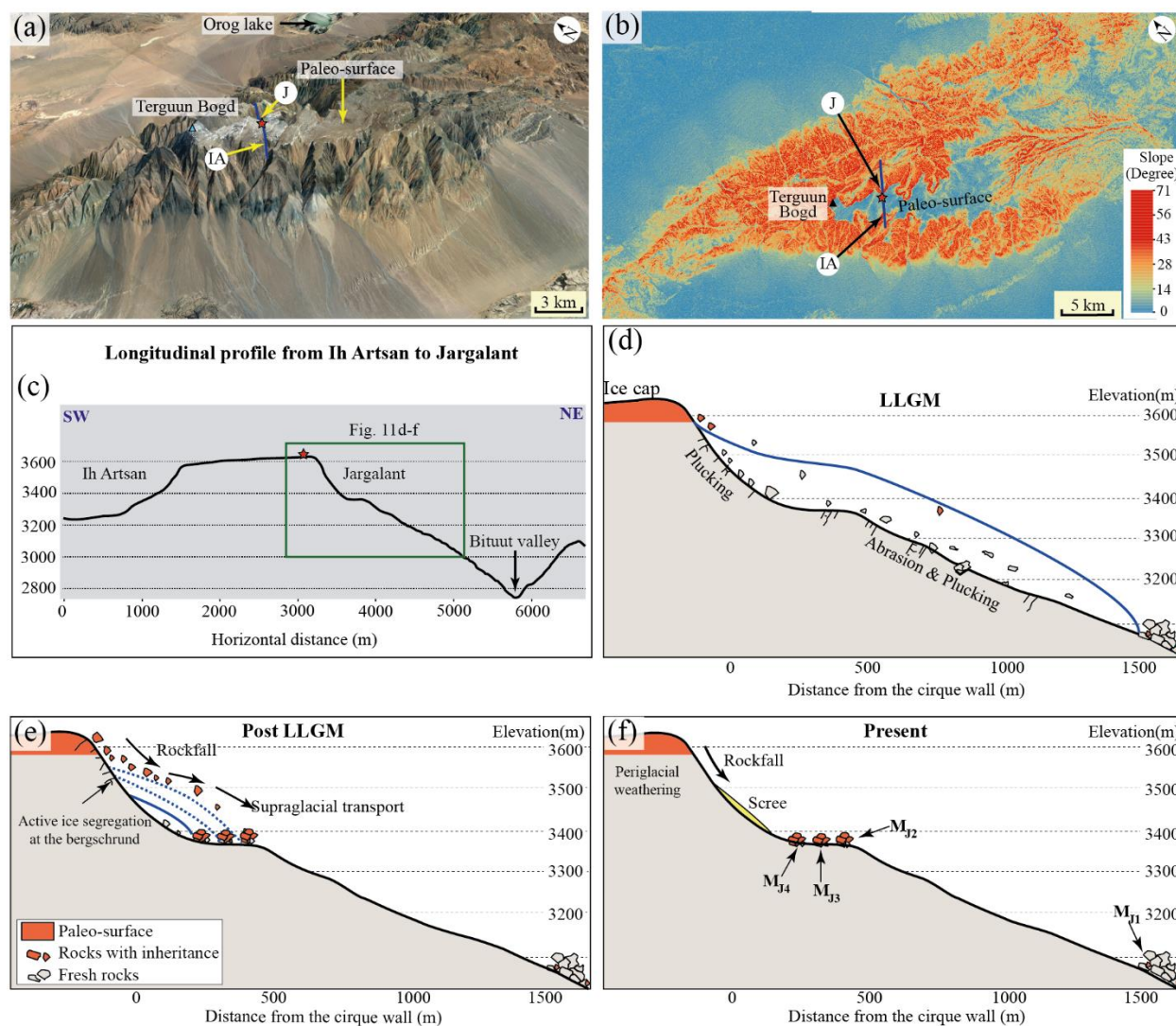


119

120 **Fig. 1011.** Rockfall deposits in Jargalant valley. The scree or talus cone was on the cirque wall. M_{J4} , M_{J3} , and M_{J2}
 121 moraine formed within a Jargalant cirque, consequently outer edges of moraine ridges near the cirque wall were
 122 covered with talus deposit. (a) Rockfall deposit on the southeastern cirque wall, near M_{J4} moraine. (b) Scree covering
 123 on M_{J2} moraine that is dissected by an intermittent stream. (c) Sampling site of M_{J3} moraine and scree on the southern
 124 and southwestern wall of the cirque, near M_{J4} , M_{J3} moraine. JAM010 was taken from the circled boulder. Chisel, for
 125 scale, is on the boulder. (d) Rockfall deposit on the eastern slope of the cirque. Yak (circled) is for scale.

126





128

129 **Fig. 112.** Inheritance from the uplifted paleo-surface of Ikh Bogd massif. (a) 3D view of the paleo-planation
 130 surface (© Google Earth, 2022). (b) Slope map of Ikh Bogd, location of the Ikh Artsan (IA) and Jargalant (J)
 131 valley. The green triangle represents the highest peak of the massif, Terguun Bogd. Exposure age and erosion rate
 132 (Table 2) were calculated using the highest concentration of the boulder from M_{J4} - M_{J2} (Fig. 11a) for the point location
 133 marked as red star (Fig. 11b; 3625 m). (c) Longitudinal profile along a dark blue line (See Fig. 11b) connecting Ikh
 134 Artsan and Jargalant valley from SW to NE. (d) LLGM (Local LGM ~17 ka) glacial extent, and intensive plucking
 135 of fresh rocks was intensive due to glacial length and thickness. (e) Enhanced supply of highly inherited rocks into a
 136 series of M_{J4} , M_{J3} , and M_{J2} moraines-moraine series which are formed by successive glacial advances or/and stagnation.
 137 According to a shortage of glacier length, low number of fresh rocks are and thinning of ice surface near cirque, less
 138 bed plucking, and more rockfall events from the paleo surface may have occurred plucked out. Thinned glacier allows
 139 intensive ice segregation along the bergschrund and more inherited rockfalls into the ice surface. Hence, boulder
 140 supply with inheritance of paleo surface would increase. (f) Present-day rockfall deposit without supraglacial transport.

141